Department of Applied Mechanics

Fatigue crack growth model for arbitrary planar cracks subjected to non-uniform stress field induced by variable amplitude loading

Pasi Lindroth

Aalto University

DOCTORAL DISSERTATIONS

Aalto University publication series
DOCTORAL DISSERTATIONS 130/2014

Fatigue crack growth model for arbitrary planar cracks subjected to non-uniform stress field induced by variable amplitude loading

Pasi Lindroth

A doctoral dissertation completed for the degree of Doctor of Science (Technology) to be defended, with the permission of the Aalto University School of Engineering, at a public examination held at the lecture hall K1/216 of the school on 19 September 2014 at 12.

Aalto University
School of Engineering
Department of Applied Mechanics
Mechanics of Materials

Supervising professor
Prof. Gary Marquis

Thesis advisor
Prof. Grzegorz Glinka

Preliminary examiners
Prof. Luca Susmel, The University of Sheffield, United Kingdom
Prof. Wolfgang Fricke, Hamburg University of Technology, Germany

Opponent
Prof. Hieronim Jakubczak, Warsaw University of Technology, Poland

Aalto University publication series
DOCTORAL DISSERTATIONS 130/2014

ISBN 978-952-60-5836-8
ISBN 978-952-60-5837-5 (pdf)
ISSN-L 1799-4934
ISSN 1799-4934 (printed)
ISSN 1799-4942 (pdf)
http://urn.fi/URN:ISBN:978-952-60-5837-5

Unigrafia Oy
Helsinki 2014

Finland

441 697
Printed matter

Aalto University

Abstract

Aalto University, P.O. Box 11000, FI-00076 Aalto www.aalto.fi

Author
Pasi Lindroth

Name of the doctoral dissertation
Fatigue crack growth model for arbitrary planar cracks subjected to non-uniform stress field induced by variable amplitude loading

Publisher School of Engineering

Unit Department of Applied Mechanics

Series Aalto University publication series DOCTORAL DISSERTATIONS 130/2014

Field of research Mechanics of Materials

Manuscript submitted 9 June 2014 **Date of the defence** 19 September 2014

Permission to publish granted (date) 21 August 2014 **Language** English

☒ **Monograph** ☐ **Article dissertation (summary + original articles)**

Abstract

Engineering components that are subjected to cyclic loads frequently contain imperfections which can rationally be assessed using linear elastic fracture mechanics. Fatigue crack growth models make use of the stress intensity factor (SIF) range and the maximum SIF to describe the driving force for crack propagation. Determining the stress intensity factor in many practical cases is difficult because the stress field is complex due to the structural geometry of the component, the crack geometry and the residual stresses caused by the manufacturing process.

Weight function (WF) solutions for numerous crack geometries have been published, e.g., for through cracks, edge cracks, surface cracks and corner cracks. However, the use of the WF for cracks of arbitrary shape is less developed. The point-load WF method for arbitrary planar cracks gives sufficiently accurate estimates of stress intensity factors for embedded cracks but the results for the surface and edge cracks are less accurate. A new form of the general point-load WF more suitable for surface breaking cracks is proposed and is combined with a crack tip plasticity based crack growth model. During numerical simulations cracks are normally modelled using a discrete number of linear segments. A new method for shifting these segments as a crack advances is also proposed.

The important aspect of the crack tip plasticity based crack growth model is the blunted crack tip with the radius of ρ^* that is assumed to be a material constant. A new method to approximate the ρ^* parameter based on the theoretical strength and fracture toughness of material is presented. The theoretical strength can be approximated based on the modulus of elasticity, and therefore, only two well established material properties are needed.

The method is verified based on comparison with published experimental results involving complex two dimensional stress fields and geometries. The experiments are related to the engineering problems such as welded structures and inclusions in a valve spring wires. The method is used to study the effect of the initial crack geometry and residual stresses. The analyses help to understand how much fatigue life estimations depend on initial parameters and when these effects must be taken into account.

Keywords weight function, fracture mechanics, fatigue

ISBN (printed) 978-952-60-5836-8 **ISBN (pdf)** 978-952-60-5837-5

ISSN-L 1799-4934 **ISSN (printed)** 1799-4934 **ISSN (pdf)** 1799-4942

Location of publisher Helsinki **Location of printing** Helsinki **Year** 2014

Pages 126 **urn** http://urn.fi/URN:ISBN:978-952-60-5837-5

Tekijä
Pasi Lindroth

Väitöskirjan nimi
Fatigue crack growth model for arbitrary planar cracks subjected to non-uniform stress field induced by variable amplitude loading

Julkaisija Insinööritieteiden korkeakoulu

Yksikkö Sovelletun mekaniikan laitos

Sarja Aalto University publication series DOCTORAL DISSERTATIONS 130/2014

Tutkimusala Lujuusoppi

Käsikirjoituksen pvm 09.06.2014 **Väitöspäivä** 19.09.2014

Julkaisuluvan myöntämispäivä 21.08.2014 **Kieli** Englanti

☒ **Monografia** ☐ **Yhdistelmäväitöskirja (yhteenveto-osa + erillisartikkelit)**

Tiivistelmä

Syklisesti kuormitetut mekaaniset komponentit sisältävät materiaalivirheitä, joita voidaan analysoida käyttämällä lineaariselastista murtumismekaniikkaa. Särönkasvumallit käyttävät jännitysintensiteettikerrointa ja jännityssuhdetta kuvaamaan särön kasvua ajavaa voimaa. Jännitysintensiteettikertoimen määrittäminen on useir vaikeaa, koska jännityskenttä on monimutkainen. Tämä johtuu rakenteiden geometriasta, valmistuksessa syntyvistä jäännösjännityksistä ja monimutkaisesta särögeometriasta. Monimutkaisissa tapauksissa jännitysintensiteetti kerroin voidaan kuitenkin laskea käyttämällä painofunktiomenetelmää.

Painofunktioratkaisuja on julkaistu monille särögeometrioille, kuten reuna-, pinta- ja kulmasärölle. Painofunktio mielivaltaisen muotoisille säröille vaatii kuitenkin vielä kehittämistä. Nykyiset painofunktiot mielivaltaisille säröille ovat riittävän tarkkoja jos särö sijaitsee materiaalin sisällä, mutta reuna- ja pintasäröjen tapauksessa tulokset voivat olla liian epätarkkoja. Tästä syystä työssä on kehitetty uusi painofunktio näille särötyypeille. Kehitetty painofunktio on yhdistetty särön kärjen plastisoitumiseen perustuvaan särönkasvumalliin. Kehitettyä menetelmää voidaan käyttää analysoimaan mielivaltaisen muotoisen särön kasvua.

Tärkeä piirre käytetyssä särönkasvumallissa on särön kärjen pyöristymä ρ^*, jonka oletetaan olevan materiaalivakio. Työssä esitellään myös uusi menetelmä ρ^*:n määrittelemiseksi käyttämällä murtolujuutta ja materiaalin teoreettista lujuutta. Teoreettinen lujuus voidaan arvioida kimmokertoimesta, jolloin ρ^* voidaan määrittää kahdesta hyvin tunnetusta materiaaliparametrista.

Kehitetty särönkasvumalli on verifioitu vertaamalla tuloksia aikaisemmin julkaistuihin kokeellisiin tuloksiin. Nämä tapaukset sisältävät monimutkaisia jännityskenttiä ja geometrioita. Valitut tapaukset liittyvät käytännössä esiintyviin vaurioihin, kuten hitsausliitoksien ja venttiilijousien väsymiseen. Menetelmää käytetään myös tutkimaan alkusärön geometrian ja jäännösjännitysten vaikutusta rakenteen elinikään.

Avainsanat painofunktiomenetelmä, murtumismekaniikka, väsyminen

ISBN (painettu) 978-952-60-5836-8 **ISBN (pdf)** 978-952-60-5837-5

ISSN-L 1799-4934 **ISSN (painettu)** 1799-4934 **ISSN (pdf)** 1799-4942

Julkaisupaikka Helsinki **Painopaikka** Helsinki **Vuosi** 2014

Sivumäärä 126 **urn** http://urn.fi/URN:ISBN:978-952-60-5837-5

Preface

I would like to express my sincere gratitude to my supervising professor, Gary Marquis, and my thesis advisor, professor Grzegorz Glinka, for this interesting research topic and their support and guidance during my doctoral studies. I also appreciate professor Heikki Remes and professor Jani Romanoff for their help and inspiring attitude toward this research.

My sincere thanks go to professor Jukka Tuhkuri, D.Sc Jouni Freund and D.Sc Kari Santaoja for teaching me important topics of solid mechanics. I am thankful to my colleagues for inspiring team spirit and many unforgettable memories. Particularly, I would like to mention Alp Karakoc, Anssi Karttunen, Eeva Mikkola, Derek Hartman, Halid Yildirim, Johanna Sjölund, Sergey Bogdanov and Susanna Hurme. Also, I wish to thank doctor Semyon Mikheevskiy for numerous intellectual discussions.

I would like to acknowledge the pre-examiners of this thesis, professor Wolfgang Fricke and professor Luca Susmel, as well as professor Hieronim Jakubczak who kindly accepted to act as my opponent.

I am grateful for funding and support I received from Aalto University, FIMECC, Ruukki, TEKES, VTT and Wärtsilä. I would also like to thank Deere & Company for their support and valuable experimental data, as well as University of Waterloo for researcher exchange period.

Finally, I would like to thank my family and friends for their endless support during all these years.

Helsinki, August 29, 2014,

Pasi Lindroth

"The business of predicting crack growth is of necessity something of a black art."

O. E. Wheeler

Contents

Original Features

Previous studies have shown that good fatigue life estimations for one-dimensional cracks can be obtained by using crack growth models, based on analysis of the material and elastic-plastic behaviour near the crack tip. However, the one-dimensional simplification is not always sufficient when complex engineering structures are considered. Therefore, the fatigue crack growth analysis method for arbitrarily-shaped planar cracks has been developed in this thesis. This thesis also provides important information about numerical fatigue crack growth simulations and various factors that influence fatigue life estimations. The following features of this thesis are considered to be original:

1. Development and evaluation of the new point load-weight function that takes into account the local bending effect. The function has been validated for arbitrarily-shaped convex planar cracks.

2. The developed weight function has been combined with a crack tip plasticity-based fatigue crack growth model. The implementation includes small crack correction and new algorithms to propagate arbitrarily-shaped planar cracks.

3. Development of a new method for the determination of the ρ^* material parameter based only on quasi-static material properties.

4. The numerical method for studying the effect of the initial crack geometry and residual stresses.

Nomenclature

a	crack length
a_i	initial crack length
A	stress intensity factor point
A_{crk}	crack area
A_{luc}	local intact area surrounding the crack
A_{uc}	area surrounding the crack
b'	fatigue strength exponent
c	crack width
c'	fatigue ductility exponent
c_i	initial crack width
C	fatigue crack growth constant
$\overline{\boldsymbol{d_p}}$	nodal point increment vector
$\overline{\boldsymbol{d_s}}$	segment increment vector
$d_{g,50\%}$	average grain size
$d_{g,99\%}$	grain size at a probability level of 99%
$\mathrm{d}N/\mathrm{d}a$	crack growth rate
D	fatigue damage
E	elastic modulus
E_p	plastic modulus
F	point load
FCG	fatigue crack growth
FEA	finite element analysis
H	generalised elastic modulus
K	stress intensity factor
K'	cyclic strength coefficient
K_{appl}	applied stress intensity factor
K_{IC}	fracture toughness
K_{net}	net stress intensity factor

K_r	local residual stress intensity factor
K_R	global residual stress intensity factor
K_{ref}	reference stress intensity factor
K_{tot}	total stress intensity factor
ΔK	stress intensity factor range
ΔK_{appl}	applied stress intensity factor range
ΔK_{eff}	effective stress intensity factor range
ΔK_{net}	net stress intensity factor range
ΔK_{ref}	reference stress intensity factor range
ΔK_{th}	threshold stress intensity factor range
ΔK_{tot}	total stress intensity factor range
l	distance between a point load and crack front
l_0	material characteristic length
m	crack growth exponent
n'	cyclic hardening exponent
$\hat{\boldsymbol{n}}_{\boldsymbol{s}}$	normal unit vector
N	number of cycle
N_f	number of cycle to failure
N_i	initiation life
p	driving force exponent
R	stress ratio
S_{max}	maximum stress in the cycle
S_{op}	stress at which the crack becomes open
SIF	stress intensity factor
t	plate thickness
u_{ref}	reference crack face displacement
w, w_A	weight function
Y	factor related to the geometry of the cracked solid
γ	angle between adjoining crack front segments
Γ_C	length of the inverted crack contour
Γ_B	length of the inverted external boundary
ϵ	strain
$\tilde{\epsilon}$	average strain over the material block
ϵ^a	elastic-plastic strain
ϵ^e	elastic strain
ϵ_{eq}	equivalent strain
ϵ'_f	fatigue ductility coefficient
$\Delta\epsilon$	strain range

κ	fatigue driving force
ν	Poisson's ratio
ρ	distance between point load and stress intensity factor point
ρ^*	crack tip radius / elementary material block size
σ	stress
$\tilde{\sigma}$	average stress over the material block
σ^a	elastic-plastic stress
σ_c	global compressive residual stress
σ^e	elastic stress
σ'_f	fatigue strength coefficient
σ_{eq}	equivalent stress
σ_r	local residual stress
σ_{ref}	reference stress
σ_t	global tensile residual stress
σ_{thr}	theoretical strength
$\Delta\sigma$	stress range
$\Delta\sigma_{th}$	fatigue limit
τ	shear stress
φ	parametric angle
Ψ	averaging constant
Ω_C	crack front
Ω_B	external boundary

1. Introduction

1.1 General

Engineering materials and mechanical components frequently contain small defects, inclusions or other crack-like features. These may arise during operation, e.g., due to stress corrosion, or they may have been introduced during the manufacturing process. In most cases, these initial cracks are not large enough to cause immediate failure, but the durability of the material is nevertheless reduced. Cyclic loading causes these cracks to grow and may ultimately lead to component failure. This phenomenon is known as fatigue failure. In material science, fatigue is understood to be progressive and permanent structural damage that occurs when a material is subjected to cyclic loading.

In most engineering cases, the cracks can be considered to be planar cracks that grow perpendicularly to the principal stress direction. Planar cracks propagate steadily under cyclic loading until they reach the critical crack size. After that, cracks begin to propagate unsteadily until final failure occurs.

The fatigue process is traditionally divided into three crack growth regions: the near-threshold region, the Paris or steady growth region and the unstable crack growth region [1]. Most of the fatigue crack growth analyses concentrate on the Paris region, at the end of which final failure is usually assumed. The fatigue crack growth which occurs in the near-threshold region is often considered to be the crack initiation period.

Numerous models have been developed to assess fatigue crack growth. Most of these models are based on linear-elastic fracture mechanics, and make used of the stress intensity factor (SIF), and are founded on the general form proposed by Paris and Erdogan [2]:

$$\frac{\mathrm{d}N}{\mathrm{d}a} = C(\Delta K_{eff})^m \tag{1.1}$$

where $\mathrm{d}a/\mathrm{d}N$ is the crack extension per cycle, ΔK_{eff} is the crack driving force based on the SIF and C and m are material constants.

Crack growth models can be divided into constant amplitude and variable amplitude models. The constant amplitude models are most often empirical and based on curve fitting. These models do not try to reproduce the actual phenomena such as deformations around the crack tip. The constant amplitude models are sufficiently accurate for most practical purposes. The variable amplitude models are more complex because the interaction between the cycles must be included. Phenomena related to those interactions are not fully understood and these models are still under development.

Marquis [3] presented a review of the most common variable amplitude crack growth prediction models. The non-interaction models are examples of models that were developed primarily for predicting the effect of stress ratio on the growth of fatigue cracks. These models can be applied to variable amplitude loading, but predict that crack growth induced by a cycle depends only on the magnitude and stress ratio of the current cycle, without the effect of previous events. Forman et al. [4] and Walker [5] proposed models of this type for the linear region of the crack growth rate curve, while Barsom and Rolfe [6] and Lal [7] proposed relationships for the near-threshold region.

Models that consider the interaction between the current fatigue cycle and preceding cycles can generally be classified into crack tip closure-based models and crack tip stress models. The plastic yield zone models of Wheeler [8] and Willenborg et al. [9] are based on the concept of residual stresses in the plastic zone. Wheeler used the ratio of the current and previous plastic zone sizes to compute the crack retardation caused by previous overloads, while Willenborg computed effective values of ΔK and R as a function of the overload plastic zone size. These models have historic significance in that they were attempts to use fracture mechanics concepts to explain changes in the crack growth rates observed during variable amplitude loading. However, following the observations of crack closure by Elber [10, 11], these models were almost abandoned.

Empirical crack tip closure models are intended to account for the effect of plasticity-induced crack closure on fatigue crack propagation (de Kon-

ing [12], Topper and Yu [13]). They model the effective SIF defined by Elber, $\Delta K_{eff} = (S_{max} - S_{op})Y\sqrt{\pi a}$, where S_{max} is the maximum stress in the cycle, S_{op} is the stress at which the crack becomes open, and Y is a factor related to the geometry of the cracked solid. Most empirical models have been developed with aircraft fatigue problems in mind. The ductile materials, load spectra with large mean stress shifts, and the thin sections found in these applications result in relatively large plastic zone sizes and frequently high degrees of closure. The Topper and Yu [13] model has also been used for small cracks in ductile aluminium and steels. Various empirical relationships for computing the S_{op} parameter have been proposed and the models show significant improvements in life-prediction capability, as compared to non-interaction models (Schjive [14]).

Yield strip-type models attempt to physically model the growing crack tip area and the plastic wake generated by a growing crack (Führing and Seeger [15], Newman [16], Wang and Blom [17]). Modifications of the Dugdale-type plastic zone [18] concept are employed to model the material deformed in the wake of an advancing crack. The crack tip closure contribution of the deformed plastic wake is computed as a function of the crack advance. These models are usually computationally demanding, but are successful in the modelling of a variety of transient events, including multiple overloads and delayed retardation.

Recent observations have led Sadananda et al. [19] to question the significance of the crack tip closure and to propose the "Unified Approach" variable amplitude model which considers the stress state ahead of the crack tip. Based on elastic-plastic stress-strain analysis in front of the crack tip, Glinka and co-workers have developed a crack tip plasticity-based model for assessing constant and variable amplitude fatigue crack propagation models (Noroozi et al. [20, 21] and Mikheevskiy [22]).

1.2 Small Crack Effect

In linear-elastic fracture mechanics, the SIF, K, uniquely describes the stresses and strains in the vicinity of the crack tip. This concept of similitude maintains that two different cracks subjected to the same K have equal plastic zone size ahead of the cracks and, as such, will propagate at an equal rate. Experimental studies indicate that the fatigue behaviour of small cracks (three-dimensional) and short cracks (two-dimensional) differ from that of long cracks [23–25]. Under the same nominal SIF, K,

the growth rates of short cracks are greater than those of long cracks. Therefore, the concept of similitude is not valid for small cracks.

Ritchie and Lankford [24] divided small cracks into classes that are associated with particular behavioural phenomena which fundamentally distinguish them from long cracks:

Mechanically small. Crack size is comparable to the size of local plasticity: e.g. small cracks embedded in the plastic zone of a notch, or cracks of a size comparable with their own crack tip plastic zones.

Microstructurally small. Crack size is comparable to the scale of the micro-structural features: e.g. crack length is on the same scale as the grain size.

Physically small. Cracks which are simply physically small, usually measuring less than 1.0 mm.

Various ideas for handling the small crack problem by taking account environmental effects and crack closure effect [24] or using elastic-plastic fracture mechanics [26] have been proposed.

1.3 State of the Art Fatigue Crack Growth Modeling Techniques

Despite the different theoretical backgrounds of closure-based models and crack tip stress models, the results obtained by using those methods are often similar. However, the fatigue crack growth model itself is not sufficient. A complete method for estimating fatigue crack growth includes the calculation of SIF, the crack growth model and algorithms for updating the crack front geometry. All of these individual parts have an effect on the limitations and accuracy of the method.

The SIF calculation plays a very significant role in any fracture mechanics-based fatigue assessment method. Unfortunately, the determination of the SIF is not trivial in most practical engineering cases, especially when the stress field or the crack geometry is complex.

Finite element analysis (FEA) can be used to determine the SIF for cases involving complex geometries and stress states. The FEA solution provides stresses and strains around the crack tip and methods such as the J-integral can be used to calculate the SIF [27]. Although FEA is a powerful tool for solving SIF problems, complications arise when the method is used in conjunction with fatigue analyses. The FEA is a very time con-

suming method because very fine meshes or special techniques are needed to obtain accurate stresses and strains near the crack tip [28]. During a fatigue analysis procedure involving the growth of a crack, the crack geometry changes with each cycle and, hence, repeated re-meshing of the model is needed and stresses and strains need to be determined for each cycle or following a small group of cycles.

FEA has successfully been used in fatigue analyses, despite the fact that the process is quite time-consuming [29–32]. However, most of these studies were carried out under constant amplitude loading using the simple non-interaction fatigue models. In most cases, finite element solutions are used to derive specific SIF solutions or weight functions, used subsequently with more complex fatigue assessment cases.

The specific SIF solutions found in handbooks [33, 34] are derived for the most common crack geometries, usually under uniform tension or bending. These are very time-efficient and accurate solutions for obtaining the SIF and widely used with advanced crack growth models. However, these solutions are not sufficient when problems with more complex stress fields need to be solved. As a consequence, the weight function technique [35, 36] is used.

Traditionally, the weight functions are derived for specific crack geometries under an arbitrary, one-dimensional stress field [37]. The weight functions are powerful tools when interaction fatigue models are used [38, 39] and SIF solutions for non-standard cracks are required. As a result, weight functions for two-dimensional stress fields have been developed to handle more complex stress fields [40–42] and arbitrary crack shapes [43–46].

The state of the art is that the crack tip closure and crack tip, stress-based interaction models are used only to model the most common crack growth problems under one-dimensional stress fields. Most of these efforts have been concentrated on surface flaws and embedded cracks have not been widely studied. Studies concerning the crack growth of arbitrary planar cracks have been reported, but only using non-interaction models [47]. In addition, the general weight function has originally been developed for embedded cracks and problems arise when surface cracks need to be considered.

Altogether, the wide range of problems can be solved using the existing methods, but the most complex cases require certain simplifications. Unfortunately, simplification can lead to unrealistic estimations of crack

growth and, therefore, methods of modelling more complex practical problems with far fewer simplifications are needed.

1.4 Objective

The primary objective of this work has been to develop a method for simulating fatigue crack growth of an arbitrary planar crack under a non-uniform, two-dimensional stress field induced by variable amplitude loading. In this method, the crack tip plasticity-based crack growth model is combined with a new general point load-weight function.

In order to accomplish this, a new, general point load-weight function was derived which includes the effect of the local bending that occurs when deep surface cracks are considered thus the crack face opening displacement is significant. The weight function can be used to calculate the SIF along the crack front, for surface cracks of arbitrary shape and embedded, arbitrarily-shaped cracks. Additionally, a new algorithm which is better able to capture the crack front advance of complex planar cracks was developed.

The method is verified by comparing various simulations with well-accepted analytical or handbook solutions. In some cases experimental data was available which highlighted crack propagation in complex stress fields which are not available in handbook solutions. However, these examples highlight real, practical engineering problems.

The method is used to study the effect of the initial crack geometry and residual stresses. The analyses help to understand how much fatigue life estimations depend upon initial parameters, and at which point these effects must be taken into account.

1.5 Limitations

Although the overall goal is to develop a method for the analysis of fatigue growth of arbitrarily-shaped planar cracks, the scope of this work is limited. In this thesis, embedded and surface planar cracks with an arbitrary, convex shape have been studied. The method can be applied to various crack types, such as corner, edge or central through-cracks, but those cases are not presented or verified in this work. The developed method includes only Mode I fatigue crack growth, because that is the

predominant mode in the majority of practical engineering cases.

In some of the verification cases, assumptions concerning the through-thickness residual stress distribution have been made. The significant influences of an assumed residual stress field have been demonstrated, but it is beyond the scope of this work to study the specific residual stress field in detail.

2. Theory

2.1 General Point Load Weight Function

2.1.1 Introduction

Bueckner [35] and Rice [36] proposed that the SIF, K, can be obtained if the crack face displacement, $u_{ref}(x;a)$, and corresponding SIF reference , K_{ref} are known for any load applied to a crack with the same geometry:

$$K = \int_0^a \sigma(x) w(x;a) \mathrm{d}x \tag{2.1}$$

where $\sigma(x)$ is the stress field over the crack length, a, in the un-cracked body, and $w(x;a)$ is the weight function:

$$w(x;a) = \frac{H}{K_{ref}} \frac{\partial u_{ref}(x;a)}{\partial x} \tag{2.2}$$

where H is the generalised elastic modulus. The notation is shown in Fig. 2.1.

The SIF, K, for a two-dimensional planar crack is then calculated by integrating the weight function and the stress field over the crack area, Ω_C.

$$K_A = \iint_{\Omega_C} \sigma(x,y) w_A(x,y;A,\Omega_C) \,\mathrm{d}x \,\mathrm{d}y \tag{2.3}$$

The index, A, denotes the arbitrary point at the crack front, Ω_C, where the SIF is to be calculated.

The weight function depends only on the geometry of the cracked body. Therefore, after the weight function is derived, it can be used with any

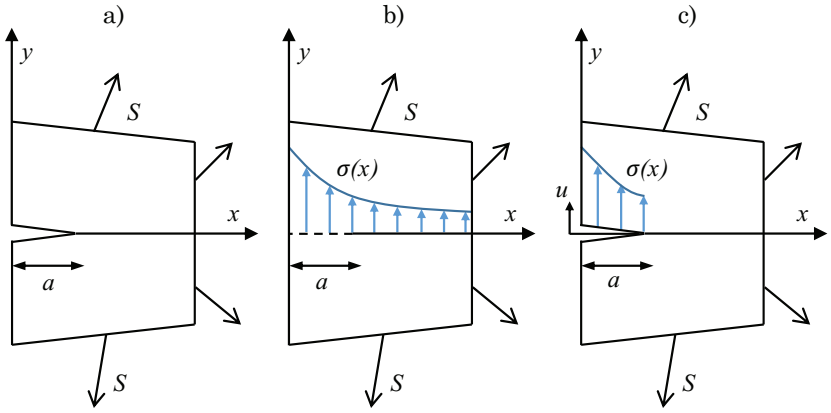

Figure 2.1. Nomenclature and the concept of weight function: a) cracked body subjected to the load system, S, (b) geometrically-identical, un-cracked body with the stress field, $\sigma(x)$, in the crack plane, induced by the loading system, S, c) geometrically-identical, cracked body with the crack subjected to the stress field, $\sigma(x)$.

stress field. As mentioned earlier, the significant advantage of the weight function is that only the stress field of the un-cracked body is used. This stress field is significantly easier to compute than the singular stress field in a cracked body.

The weight functions, $w(x;a)$, for the different crack geometries can be derived from existing literature; Shen and Glinka [37] presented a method for deriving weight functions using reference SIF solutions, without knowing the crack face displacement. The limitation of these weight functions is that they are derived for a specific crack shape and are limited to a one-dimensional stress field. In order to model the fatigue crack growth in more complex applications, such as welded joints, more general weight functions are needed.

2.1.2 The General Point Load Weight Function

Oore and Burns [43] proposed a general weight function for arbitrarily-shaped planar cracks, based on their observation of SIF solutions for different crack geometries. The weight function depends on two parameters, the distance, ρ, between the load point, F, and point A along the crack front at which the SIF needs to be determined and the line integral along the crack contour, Ω_C.

$$w_A(x,y) = \frac{\sqrt{2}}{\pi\rho^2\sqrt{\oint_{\Omega_C}\frac{\mathrm{d}\Omega_C}{l^2}}} \tag{2.4}$$

The notation is shown in Fig. 2.2. The exact weight function for the embedded circular crack in an infinite body can be derived from Eq. (2.4) by solving the line integral in closed form [43]. Solving the line integral for more complex geometries is not a trivial task. However, Glinka and Reinhardt [44] presented a geometrical interpretation of the line integral that simplifies the calculations. The line integral can be replaced by the length of the inverted crack contour, Γ_C, with respect to the location of the point load. Therefore, the point-load weight function for an embedded crack can be written in a simpler form.

$$w_A(x,y) = \frac{\sqrt{2}}{\pi\rho^2\sqrt{\Gamma_C}} \tag{2.5}$$

Glinka and Reinhardt [44] also proposed a method, taking into account the finite boundaries of the cracked body, Ω_B. The effect of the external boundaries can be included by using an inverted contour idea which is similar to the inverted crack contour. The external contour has to be inverted with respect to the point, A, where the SIF is to be calculated. The general point-load weight function for surface, edge and embedded cracks in both infinite and (semi-)finite bodies can therefore be written as:

$$w_A(x,y) = \frac{\sqrt{2}}{\pi\rho^2}\frac{\sqrt{\Gamma_C+\Gamma_B}}{\Gamma_C} \tag{2.6}$$

Since the general weight function, $w_A(x,y)$, is known, Eq. (2.3) can be used to compute the SIF at any point along the crack front of any arbitrary planar crack.

2.2 Crack Growth Rate

2.2.1 Introduction

It is generally accepted that local stresses and strains near the crack tip control the fatigue crack growth process. It is difficult to determine the crack tip stress and strain in the case of elastic-plastic behaviour as these are strongly dependent on the theoretical and numerical methods used in

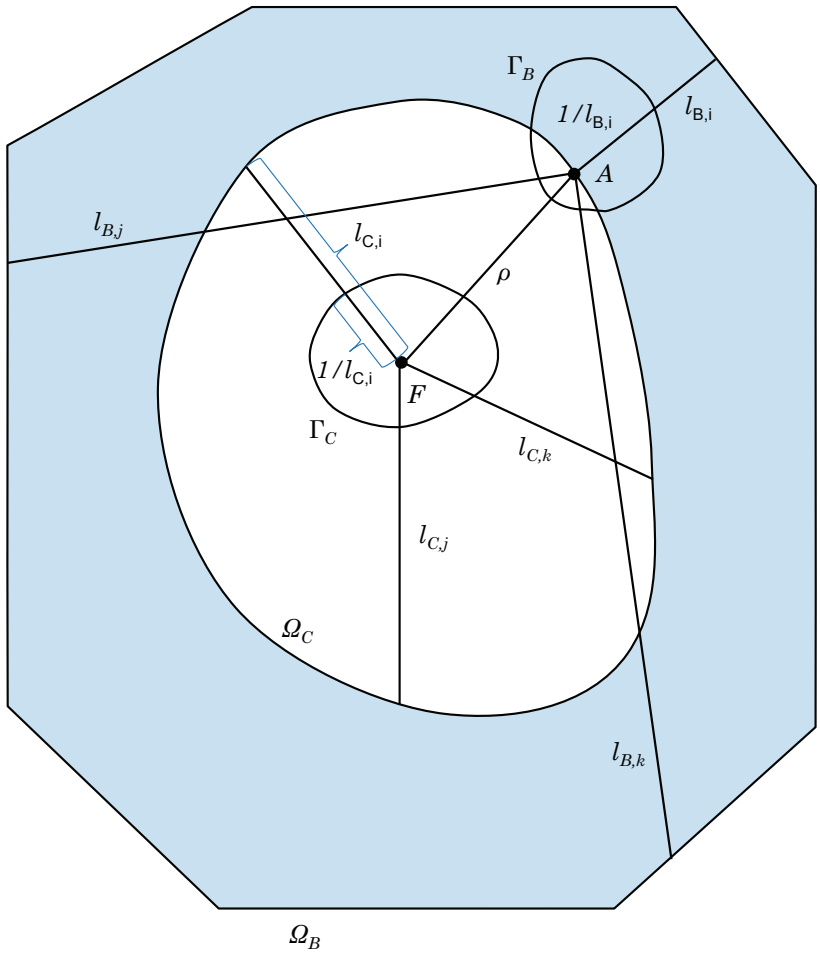

Figure 2.2. Notation for the general weight function for an arbitrary planar crack in a finite body.

the analysis.

If the theory of classic, linear-elastic fracture mechanics is used, the crack tip is assumed to be infinitely sharp and, therefore, the stress field near the crack tip is singular. In order to avoid a singular stress field, the crack tip can be modelled as a notch with a finite radius, ρ^* [48–51]. Notch theories yield finite, thus more realistic, stresses and strains in the vicinity of the crack tip.

Neuber [51] proposed that, as a material property, the minimum effective notch tip radius, ρ^*, controls the maximum stress concentration which can be generated in a material. Noroozi et al. [20] suggested that the crack tip radius is the smallest notch radius which can occur in a material.

In this regard, the Neuber micro-support concept [51] suggests that a material can be modelled by considering elementary blocks of the dimension, ρ^* (Fig. 2.3). The elementary material block can be considered as the smallest material volume to which can be applied the continuum mechanics and bulk material properties such as modulus of elasticity, E; Poisson's ratio, ν; the strength coefficient, K'; and the strain hardening exponent, n'. A similar observation was made by Forsyth [52].

Based on these observations, Noroozi et al. [20] proposed the following fatigue crack growth model:

- The material is assumed to be composed of identical, elementary material blocks of a finite dimension, ρ^*.

- The fatigue crack can be analysed as a notch with the tip radius, ρ^*.

- The fatigue crack growth is considered as successive crack re-initiations over the distance, ρ^*.

- The material properties used in the proposed model are the Ramberg-Osgood cyclic stress-strain curve [53] with kinematic hardening:

$$\begin{aligned} \varepsilon &= \frac{\sigma}{E} + \left(\frac{\sigma}{K'}\right)^{1/n'} \\ \Delta\varepsilon &= \frac{\Delta\sigma}{E} + 2\left(\frac{\Delta\sigma}{2K'}\right)^{1/n'} \end{aligned} \tag{2.7}$$

and the Manson-Coffin strain-life fatigue curve [54]:

$$\frac{\Delta\varepsilon}{2} = \frac{\sigma_f^{'}}{E}(2N)^{b'} + \epsilon_f^{'}(2N)^{c'} \tag{2.8}$$

- The number of cycles, N, to failure of the first elementary block of the material at the crack-tip can be determined from the Manson-Coffin strain-life fatigue curve, by accounting for the stress-strain history and using the Smith-Watson-Topper (SWT) fatigue damage parameter[55].

$$D = \sigma_{max}\frac{\Delta\varepsilon}{2} \tag{2.9}$$

- The fatigue crack growth rate can be determined as the average fatigue crack propagation rate over the elementary material block of the size ρ^*.

$$\frac{\mathrm{d}a}{\mathrm{d}N} = \frac{\rho^*}{N} \tag{2.10}$$

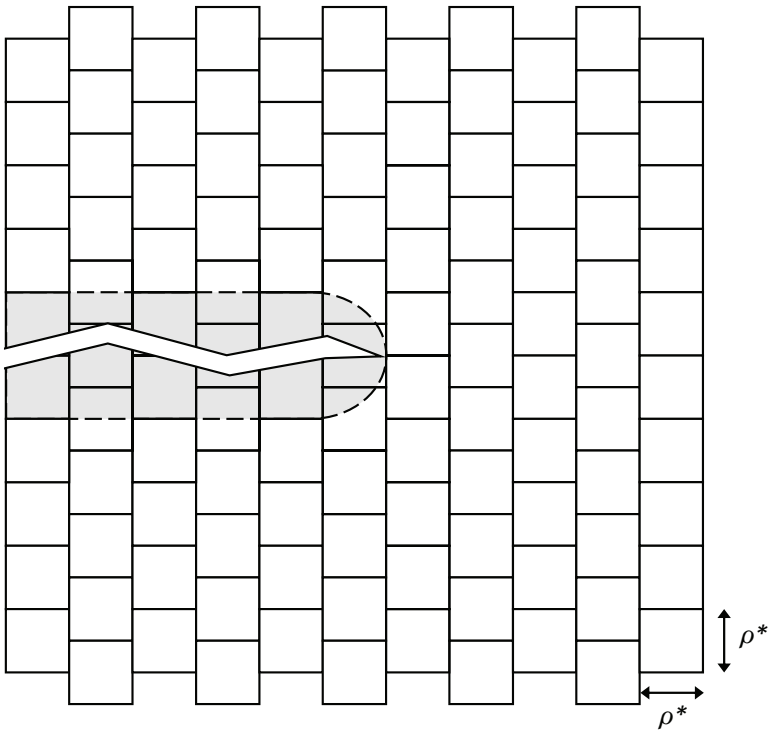

Figure 2.3. A crack and discrete elementary material blocks.

2.2.2 Method of Calculation of Local Elastic-Plastic Stresses and Strains near the Crack-Tip

Stresses near the crack tip are calculated by assuming that the crack tip is blunt and, therefore, the stress field is not singular. The linear-elastic stresses at the crack tip can be calculated by using the Creager-Paris solution [56], as shown in Fig. 2.4.

$$\begin{aligned}
\sigma_x^e(r,\theta) &= -\frac{K}{\sqrt{2\pi r}}\frac{\rho^*}{2r}\cos\frac{3\theta}{2} + \frac{K}{\sqrt{2\pi r}}\cos\frac{\theta}{2}\left[1-\sin\frac{\theta}{2}\sin\frac{3\theta}{2}\right] + \dots \\
\sigma_y^e(r,\theta) &= \frac{K}{\sqrt{2\pi r}}\frac{\rho^*}{2r}\cos\frac{3\theta}{2} + \frac{K}{\sqrt{2\pi r}}\cos\frac{\theta}{2}\left[1+\sin\frac{\theta}{2}\sin\frac{3\theta}{2}\right] + \dots \\
\tau_{xy}^e(r,\theta) &= -\frac{K}{\sqrt{2\pi r}}\frac{\rho^*}{2r}\sin\frac{3\theta}{2} + \frac{K}{\sqrt{2\pi r}}\sin\frac{\theta}{2}\cos\frac{\theta}{2}\cos\frac{3\theta}{2} + \dots
\end{aligned} \tag{2.11}$$

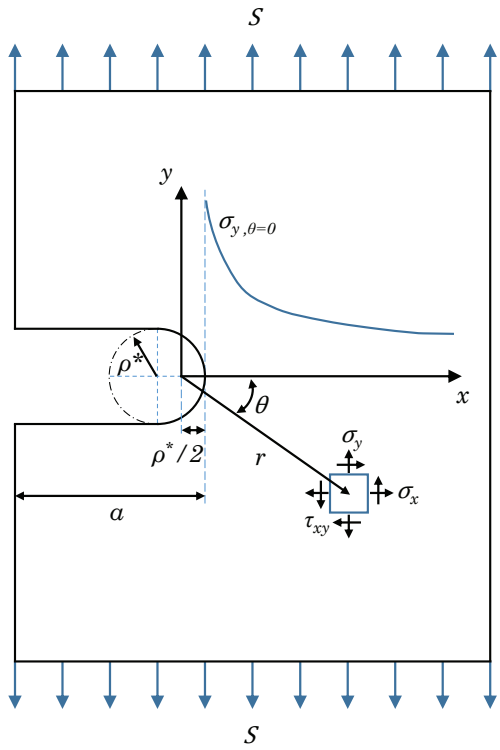

Figure 2.4. Linear-elastic stresses ahead of a blunted crack tip.

The linear-elastic stress components along the crack plane ($\theta = 0$, $r = x$) are now obtained by removing the high order terms:

$$\sigma_x^e = \frac{K}{\sqrt{2\pi x}}\left(1 - \frac{\rho^*}{2x}\right)$$
$$\sigma_y^e = \frac{K}{\sqrt{2\pi x}}\left(1 + \frac{\rho^*}{2x}\right) \tag{2.12}$$
$$\tau_{xy}^e = 0$$

It is important to note from Eq. (2.12) that the crack tip is located at $x = \rho^*/2$. Thus, the maximum stresses and stress ranges can be written as:

$$\sigma_{x,max}^e = \frac{K_{max,net}}{\sqrt{2\pi x}}\left(1 - \frac{\rho^*}{2x}\right)$$
$$\sigma_{y,max}^e = \frac{K_{max,net}}{\sqrt{2\pi x}}\left(1 + \frac{\rho^*}{2x}\right)$$
$$\Delta\sigma_x^e = \frac{\Delta K_{net}}{\sqrt{2\pi x}}\left(1 - \frac{\rho^*}{2x}\right) \tag{2.13}$$
$$\Delta\sigma_y^e = \frac{\Delta K_{net}}{\sqrt{2\pi x}}\left(1 + \frac{\rho^*}{2x}\right)$$

The net SIFs in Eq. (2.13) are defined as:

$$\begin{aligned} K_{max,net} &= K_{max,appl} \\ \Delta K_{net} &= K_{max,net} - K_{min,net} \\ \Delta K_{min,net} &= \begin{cases} K_{min,appl} & \text{if} \quad K_{min,appl} \geq 0 \\ \dfrac{3}{2Y}\sqrt{\dfrac{\rho^*}{a}}K_{min,appl} & \text{if} \quad K_{min,appl} < 0 \end{cases} \end{aligned} \tag{2.14}$$

wher Y is a factor related to the geometry of the cracked solid. The $\Delta K_{min,net}$ parameter, in the case of $K_{min,appl} < 0$ load in Eq. (2.14), is calculated by assuming that a compressive load does not close the crack completely. The crack tip remains open as a circular hole with the radius of ρ^*. The derivation of the $\Delta K_{min,net}$ expression is presented elsewhere [20].

When the linear-elastic stresses are known, the actual elastic-plastic stresses and strains can be obtained by using the Neuber rule [57]. The Neuber rule hypothesises the equivalence of the strain energy density at the notch tip, between the linear-elastic and elastic-plastic behaviour of geometrically-identical notched bodies subjected to identical external

loads.

$$\sigma^a \varepsilon^a = \sigma^e \varepsilon^e \tag{2.15}$$

The original Neuber rule, Eq. (2.15), was derived for a pure shear stress state. The stress state near a crack tip is bi-axial in case of plane stress or, respectively, tri-axial in the state of plane strain. Fortunately, the Neuber rule has been also expanded for multi-axial proportional and non-proportional loading paths [58, 59].

In the case of a bi-axial stress state, all maximum, elastic-plastic, crack tip strains and stresses can be determined by using Hencky stress-strain relationships [60], the Ramberg-Osgood stress-strain constitutive equation, Eq. (2.7), and the multi-axial Neuber rule:

$$\begin{cases} \varepsilon^a_{x,max} = \dfrac{1}{E}\left(\sigma^a_{x,max} - \upsilon\sigma^a_{y,max}\right) + \dfrac{1}{E_p}\left(\sigma^a_{x,max} - \dfrac{1}{2}\sigma^a_{y,max}\right) \\ \varepsilon^a_{y,max} = \dfrac{1}{E}\left(\sigma^a_{y,max} - \upsilon\sigma^a_{x,max}\right) + \dfrac{1}{E_p}\left(\sigma^a_{y,max} - \dfrac{1}{2}\sigma^a_{x,max}\right) \\ \sigma^a_{x,max}\varepsilon^a_{x,max} = \sigma^e_{x,max}\varepsilon^e_{x,max} \\ \sigma^a_{y,max}\varepsilon^a_{y,max} = \sigma^e_{y,max}\varepsilon^e_{y,max} \end{cases} \tag{2.16}$$

where

$$\begin{aligned} E_p &= \frac{\sigma^a_{eq}}{\varepsilon^a_{eq}} \\ \varepsilon^a_{eq} &= \left(\frac{\sigma^a_{eq}}{K'}\right)^{1/n'} \\ \sigma^a_{eq} &= \sqrt{\left(\sigma^a_{x,max}\right)^2 - \sigma^a_{x,max}\sigma^a_{y,max} + \left(\sigma^a_{y,max}\right)^2} \\ \sigma^e_{x,max} &= \frac{K_{max,net}}{\sqrt{2\pi x}}\left(1 - \frac{\rho^*}{2x}\right) \\ \sigma^e_{y,max} &= \frac{K_{max,net}}{\sqrt{2\pi x}}\left(1 + \frac{\rho^*}{2x}\right) \end{aligned}$$

The actual elastic-plastic stress and strain ranges can be determined from a similar set of equations.

$$\begin{cases} \Delta\varepsilon_x^a = \dfrac{1}{E}\left(\Delta\sigma_x^a - \upsilon\Delta\sigma_y^a\right) + \dfrac{1}{E_p}\left(\Delta\sigma_x^a - \dfrac{1}{2}\Delta\sigma_y^a\right) \\ \Delta\varepsilon_y^a = \dfrac{1}{E}\left(\Delta\sigma_y^a - \upsilon\Delta\sigma_x^a\right) + \dfrac{1}{E_p}\left(\Delta\sigma_y^a - \dfrac{1}{2}\Delta\sigma_x^a\right) \\ \Delta\sigma_x^a\Delta\varepsilon_x^a = \Delta\sigma_x^e\Delta\varepsilon_x^e \\ \Delta\sigma_y^a\Delta\varepsilon_y^a = \Delta\sigma_y^e\Delta\varepsilon_y^e \end{cases} \tag{2.17}$$

where

$$\begin{aligned} E_p &= \frac{\Delta\sigma_{eq}^a}{\Delta\varepsilon_{eq}^{a,p}} \\ \Delta\varepsilon_{eq}^{a,p} &= 2\left(\frac{\Delta\sigma_{eq}^a}{2K'}\right)^{1/n'} \\ \Delta\sigma_{eq}^a &= \sqrt{\left(\Delta\sigma_x^a\right)^2 - \Delta\sigma_x^a\Delta\sigma_y^a + \left(\Delta\sigma_y^a\right)^2} \\ \Delta\sigma_x^e &= \frac{\Delta K_{net}}{\sqrt{2\pi x}}\left(1 - \frac{\rho^*}{2x}\right) \\ \Delta\sigma_y^e &= \frac{\Delta K_{net}}{\sqrt{2\pi x}}\left(1 + \frac{\rho^*}{2x}\right) \end{aligned}$$

2.2.3 Method of Calculation of the Residual Stress Intensity Factor

When the actual elastic-plastic stresses are known, the residual stresses that remain in the region of the crack tip following an applied loading cycle can be calculated:

$$\sigma_r = \sigma_{y,max}^a - \Delta\sigma_y^a \tag{2.18}$$

The residual stress distribution ahead of the crack tip is obtained by varying parameter x (the distance from the crack tip) in Eqs. (2.16) and (2.17) and by using Eq. (2.18).

The effect of local residual stresses near the crack tip, induced by cyclic plasticity, is taken into account by defining a residual SIF, K_r. Hence, the effect of the complex stress field, based on elastic-plastic stress and strain analysis, can be described by one scalar.

Due to the complex residual stress field, the weight function method has been utilised in SIF computations. Mikheevskiy [22] pointed out that the size of the residual stress field is relatively small compared to the crack length and, therefore, the following universal, geometrically-independent,

one-dimensional weight function is sufficient to obtain the K_r.

$$w(x,a) = \frac{2F}{\sqrt{2\pi(a-x)}} \tag{2.19}$$

The residual SIF, K_r, is obtained by integrating the residual stress field, Eq. (2.18), and the weight function, Eq. (2.19), over the crack length.

$$K_r = \int_0^a \sigma_r(x) w(x,a) \mathrm{d}x \tag{2.20}$$

It is important to note that only the residual stress field behind the crack tip contributes to the residual SIF. Consequently, the crack tip has to grow into the zone under compressive residual stresses before crack growth retardation occurs. This corresponds to experiments which show delayed retardation [61].

2.2.4 Total Stress Intensity Factor

Crack growth occurs only if an applied cycle is large enough to overcome the compressive residual stresses that tend to resist crack face opening. Thus, only the portion of the loading that exceeds the residual stresses contributes to crack growth. Therefore, as seen in Fig. 2.5, the local residual SIF, K_r, which always has a negative value, is added to the applied SIF. This also affects the SIF range.

$$\begin{aligned} K_{max,tot} &= K_{max,net} + K_r \\ \Delta K_{tot} &= \Delta K_{net} + K_r \end{aligned} \tag{2.21}$$

2.2.5 Simplified Elastic-Plastic Stresses and Strains Near the Crack Tip

In order to derive a practical expression for the fatigue crack driving force, closed form solutions for σ^a_{max} and $\Delta\varepsilon^a$ are needed. Unfortunately, Eqs. (2.16) and (2.17) are non-linear equations and closed form solutions are not feasible. Consequently, an approximate solution is needed. The approximate solution is used only to obtain the fatigue driving force. Eqs. (2.16) and (2.17) can be solved numerically when local residual stresses are calculated.

Fatigue crack growth is considered to be successive crack initiations over a series of elementary material blocks at the crack tip. Therefore, the av-

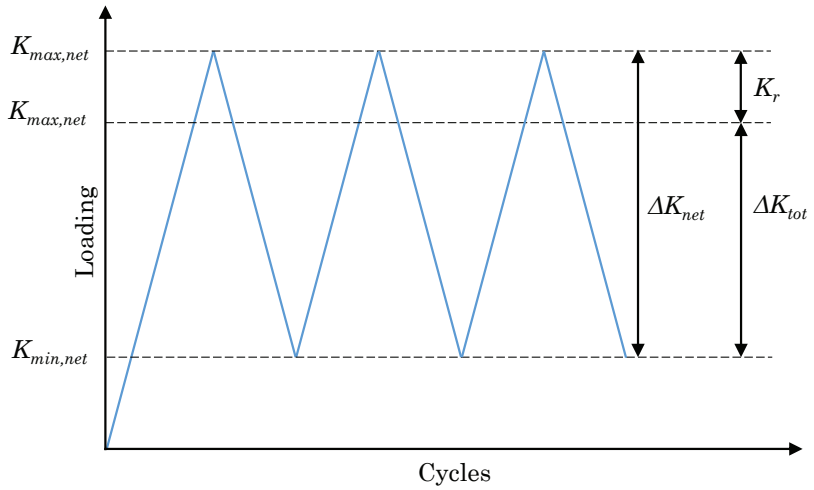

Figure 2.5. The maximum SIF, K_{max}, and the SIF range ΔK are affected by the local residual SIF, K_r.

erage stresses over the block are calculated using Eq. (2.12). The average stresses over the i^{th} material block are:

$$\begin{aligned}\tilde{\sigma}^e_{x,i} &= \frac{1}{x_{i+1}-x_i}\int_{x_i}^{x_{i+1}} \frac{K}{\sqrt{2\pi x}}\left(1-\frac{\rho^*}{2x}\right)\mathrm{d}x \\ \tilde{\sigma}^e_{y,i} &= \frac{1}{x_{i+1}-x_i}\int_{x_i}^{x_{i+1}} \frac{K}{\sqrt{2\pi x}}\left(1+\frac{\rho^*}{2x}\right)\mathrm{d}x\end{aligned} \tag{2.22}$$

Thus, the average stresses over the first material block are:

$$\begin{aligned}\tilde{\sigma}^e_{x,1} &= \frac{\Psi_{x,1}K_{tot}}{\sqrt{2\pi\rho^*}} \\ \tilde{\sigma}^e_{y,1} &= \frac{\Psi_{y,1}K_{tot}}{\sqrt{2\pi\rho^*}}\end{aligned} \tag{2.23}$$

where

$$\begin{aligned}\Psi_{x,1} &= \frac{2\sqrt{2}\left(2\sqrt{3}-3\right)}{3} \\ \Psi_{y,1} &= \frac{2}{3}\sqrt{6}\end{aligned} \tag{2.24}$$

The actual elastic-plastic stresses and strains are obtained in a similar way to that described in Section 2.2.2. In the case of plane stress condition, the stress state over the first elementary material block reduces to one normal stress component, σ_y. Hence, Eq. (2.16) reduces to the classic, uni-axial Neuber rule associated with the Ramberg-Osgood equation.

$$\begin{cases} \tilde{\varepsilon}^a_{x,1} = -\dfrac{\upsilon}{E}\tilde{\sigma}^a_{y,1} - \dfrac{1}{2}\left(\dfrac{\tilde{\sigma}^a_{y,1}}{K'}\right)^{1/n'} \\ \tilde{\varepsilon}^a_{y,1} = \quad \dfrac{1}{E}\tilde{\sigma}^a_{y,1} + \left(\dfrac{\tilde{\sigma}^a_{y,1}}{K'}\right)^{1/n'} \\ \tilde{\sigma}^a_{y,1}\tilde{\varepsilon}^a_{y,1} = \tilde{\sigma}^e_{y,1}\tilde{\varepsilon}^e_{y,1} \end{cases} \tag{2.25}$$

The uni-axial Neuber rule, Eq. (2.15), can also be written in terms of the SIF.

$$\tilde{\sigma}^e_{y,1}\tilde{\varepsilon}^e_{y,1} = \frac{\left(\tilde{\sigma}^e_{y,1}\right)^2}{E} = \frac{1}{E}\left(\frac{\Psi_{y,1}K_{tot}}{\sqrt{2\pi\rho^*}}\right)^2 = \tilde{\sigma}^a_{y,1}\tilde{\varepsilon}^a_{y,1} \tag{2.26}$$

Then, the maximum elastic-plastic stress and strain at the crack tip can be determined by solving Eqs. (2.25) and (2.26):

$$\begin{cases} \dfrac{1}{E}\left(\dfrac{\Psi_{y,1}K_{max,tot}}{\sqrt{2\pi\rho^*}}\right)^2 = \dfrac{\left(\tilde{\sigma}^a_{max}\right)^2}{E} + \tilde{\sigma}^a_{max}\left(\dfrac{\tilde{\sigma}^a_{max}}{K'}\right)^{1/n'} \\ \tilde{\varepsilon}^a_{max} = \dfrac{\tilde{\sigma}^a_{max}}{E} + \left(\dfrac{\tilde{\sigma}^a_{max}}{K'}\right)^{1/n'} \end{cases} \tag{2.27}$$

The elastic-plastic stress and strain ranges can be determined by starting from Eq. (2.17) and using Eqs. (2.25) and (2.26).

$$\begin{cases} \dfrac{1}{E}\left(\dfrac{\Psi_{y,1}\Delta K_{tot}}{\sqrt{2\pi\rho^*}}\right)^2 = \dfrac{\left(\Delta\tilde{\sigma}^a\right)^2}{E} + 2\Delta\tilde{\sigma}^a\left(\dfrac{\Delta\tilde{\sigma}^a}{2K'}\right)^{1/n'} \\ \Delta\tilde{\varepsilon}^a = \dfrac{\Delta\tilde{\sigma}^a}{E} + 2\left(\dfrac{\Delta\tilde{\sigma}^a}{2K'}\right)^{1/n'} \end{cases} \tag{2.28}$$

Noroozi et al. [20] proposed that at high applied loads, the elastic terms in Eqs. (2.27) and (2.28) can be neglected because the strains at the crack tip are predominantly plastic. The strains at the crack tip in the near-threshold fatigue crack growth region are predominantly elastic and, therefore, the plastic terms can be ignored. These assumptions lead to the following equations:

Predominantly Elastic (near threshold region):

$$\begin{cases} \dfrac{1}{E}\left(\dfrac{\Psi_{y,1}K_{max,tot}}{\sqrt{2\pi\rho^*}}\right)^2 = \dfrac{\left(\tilde{\sigma}^a_{max}\right)^2}{E} \\ \tilde{\varepsilon}^a_{max} = \dfrac{\tilde{\sigma}^a_{max}}{E} \end{cases} \tag{2.29}$$

$$\begin{cases} \dfrac{1}{E}\left(\dfrac{\Psi_{y,1}\Delta K_{tot}}{\sqrt{2\pi\rho^*}}\right)^2 = \dfrac{\left(\Delta\tilde{\sigma}^a\right)^2}{E} \\ \Delta\tilde{\varepsilon}^a = \dfrac{\Delta\tilde{\sigma}^a}{E} \end{cases} \tag{2.30}$$

Predominantly Plastic (Paris region):

$$\begin{cases} \dfrac{1}{E}\left(\dfrac{\Psi_{y,1}K_{max,tot}}{\sqrt{2\pi\rho^*}}\right)^2 = \tilde{\sigma}^a_{max}\left(\dfrac{\tilde{\sigma}^a_{max}}{K'}\right)^{1/n'} \\ \tilde{\varepsilon}^a_{max} = \left(\dfrac{\tilde{\sigma}^a_{max}}{K'}\right)^{1/n'} \end{cases} \tag{2.31}$$

$$\begin{cases} \dfrac{1}{E}\left(\dfrac{\Psi_{y,1}\Delta K_{tot}}{\sqrt{2\pi\rho^*}}\right)^2 = 2\Delta\tilde{\sigma}^a\left(\dfrac{\Delta\tilde{\sigma}^a}{2K'}\right)^{1/n'} \\ \Delta\tilde{\varepsilon}^a = 2\left(\dfrac{\Delta\tilde{\sigma}^a}{2K'}\right)^{1/n'} \end{cases} \tag{2.32}$$

Then, σ^a_{max} and $\Delta\varepsilon^a$ can be solved in closed form:

Predominantly Elastic (near threshold region):

$$\begin{cases} \tilde{\sigma}^a_{max} = \dfrac{\Psi_{y,1}K_{max,tot}}{\sqrt{2\pi\rho^*}} \\ \Delta\tilde{\varepsilon}^a = \dfrac{\Psi_{y,1}\Delta K_{tot}}{E\sqrt{2\pi\rho^*}} \end{cases} \tag{2.33}$$

Predominantly Plastic (Paris region):

$$\begin{cases} \tilde{\sigma}^a_{max} = \left(\dfrac{\left(\Psi_{y,1}\right)^2\left(K'\right)^{1/n'}}{2\pi E\rho^*}\right)^{n'/(n'+1)}\left(K^2_{max,tot}\right)^{n'/(n'+1)} \\ \Delta\tilde{\varepsilon}^a = \left(\dfrac{2^{n'}\left(\Psi_{y,1}\right)^2}{4\pi EK'\rho^*}\right)^{1/(n'+1)}\left(\Delta K^2_{tot}\right)^{1/(n'+1)} \end{cases} \tag{2.34}$$

2.2.6 Fatigue Crack Driving Force

Fatigue crack growth is considered to be successive crack initiations over the elementary material block at the crack tip. N_f, the number of cycles required to break the first material block, ρ^*, can be determined by using the Manson-Coffin strain-life curve, Eq. (2.8), and the SWT damage parameter, Eq. (2.9):

$$\tilde{\sigma}^a_{max}\frac{\Delta\tilde{\varepsilon}^a}{2} = \frac{\left(\sigma'_f\right)^2}{E}(2N_f)^{2b'} + \sigma'_f\varepsilon'_f(2N_f)^{b'+c'} \tag{2.35}$$

In order to remain consistent, Eq. (2.35) should be divided into elastic and plastic terms, in the same way that the stresses and strains were divided in Section 2.2.5.

Predominantly Elastic (near threshold region):

$$\tilde{\sigma}^a_{max}\frac{\Delta\tilde{\varepsilon}^a}{2} = \frac{\left(\sigma'_f\right)^2}{E}(2N_f)^{2b'} \tag{2.36}$$

Predominantly Plastic (Paris region):

$$\tilde{\sigma}^a_{max}\frac{\Delta\tilde{\varepsilon}^a}{2} = \sigma'_f\varepsilon'_f(2N_f)^{b'+c'} \tag{2.37}$$

When stresses and strains from Eqs. (2.33) and (2.34) are substituted into Eqs. (2.36) and (2.37), the number of cycles, N_f, needed for the failure of the elementary material block can be obtained:

Predominantly Elastic (near threshold region):

$$N_f = \frac{1}{2}\left[\frac{\Psi_{y,1}^2}{4\sigma_f'^2\pi\rho^*}\left(K_{max,tot}\right)\left(\Delta K_{tot}\right)\right]^{1/(2b')} \tag{2.38}$$

Predominantly Plastic (Paris region):

$$N_f = \frac{1}{2}\left[\frac{\Psi_{y,1}^2}{2^{(n'+3)/(n'+1)}\sigma_f'\varepsilon_f'\pi E\rho^*}\left(K_{max,tot}^2\right)^{n'/(n'+1)}\left(\Delta K_{tot}^2\right)^{1/(n'+1)}\right]^{1/(b'+c')} \tag{2.39}$$

The fatigue crack growth rate, Eq. (2.10), can subsequently be calculated as:

Predominantly Elastic (near threshold region):

$$\frac{\mathrm{d}a}{\mathrm{d}N} = 2\rho^*\left[\frac{\Psi_{y,1}^2}{4\sigma_f'^2\pi\rho^*}\left(K_{max,tot}\right)\left(\Delta K_{tot}\right)\right]^{-1/(2b')} \tag{2.40}$$

Predominantly Plastic (Paris region):

$$\frac{\mathrm{d}a}{\mathrm{d}N} = 2\rho^*\left[\frac{\Psi_{y,1}^2}{2^{(n'+3)/(n'+1)}\sigma_f'\varepsilon_f'\pi E\rho^*}\left(K_{max,tot}^2\right)^{n'/(n'+1)}\left(\Delta K_{tot}^2\right)^{1/(n'+1)}\right]^{-1/(b'+c')} \tag{2.41}$$

The SIFs are the only variables in Eqs. (2.40) and (2.41) and, therefore, the fatigue crack growth expression can be written in a general form as:

$$\frac{\mathrm{d}a}{\mathrm{d}N} = C\left[\left(K_{max,tot}\right)^p\left(\Delta K_{tot}\right)^{1-p}\right]^m \tag{2.42}$$

Equation (2.42) indicates that the fatigue crack driving force consists of two SIF parameters. Parameters C, m and p depend upon a predominant strain component, i.e., predominantly elastic strain or predominantly plastic strain.

Predominantly Elastic (near threshold region):

$$\begin{aligned} C &= 2\rho^*\left[\frac{\Psi_{y,1}^2}{4\sigma_f'^2\pi\rho^*}\right]^{-1/(2b')} \\ m &= -\frac{1}{b'} \\ p &= 0.5 \end{aligned} \tag{2.43}$$

Predominantly Plastic (Paris region):

$$\begin{aligned} C &= 2\rho^* \left[\frac{\Psi_{y,1}^2}{2^{(n'+3)/(n'+1)} \sigma_f' \varepsilon_f' \pi E \rho^*} \right]^{-1/(b'+c')} \\ m &= -\frac{2}{b'+c'} \\ p &= \frac{n'}{n'+1} \end{aligned} \tag{2.44}$$

2.2.7 Determination of the Parameter ρ^*

The method presented is based on the assumption that the material can be modelled using elementary material blocks with a finite dimension, ρ^*. The block size, ρ^*, is assumed to be a material property and also defines the smallest notch tip radius that can exist in a material.

The dimension, ρ^* , is indirectly dependent on the micro-structural features of the analysed material, but thus far, it cannot be uniquely associated with any specific, micro-structural particle size. Rather, the elementary, material block size, ρ^* , can be understood as an average dimension of inhomogeneous material blocks which still behave like the bulk material of larger volume.

The material parameter, ρ^*, cannot be measured directly. Therefore, various methods have been developed to determine ρ^* indirectly, depending on available data.

Determination of the ρ^* Parameter from $\mathrm{d}a/\mathrm{d}N$ vs. ΔK Fatigue Crack Growth Data

The most reliable estimation for ρ^* can be obtained if several $\mathrm{d}a/\mathrm{d}N$ vs. ΔK curves with different stress ratios, R, are available; the following technique is used as proposed by Mikheevskiy [22].

Since the mean stress effect has already been accounted for by using the SWT fatigue damage parameter, Eq. (2.9), the material constants in Eq. (2.42) are assumed to be independent of the stress ratio, R. As a result, the same driving force, $\kappa = (K_{max,tot})^p (\Delta K_{tot})^{1-p}$, resulting from various combinations of $K_{max,tot}$ and ΔK_{tot}, must always lead to the same crack growth rate, $\mathrm{d}a/\mathrm{d}N$. Therefore, all $\mathrm{d}a/\mathrm{d}N$ vs. ΔK curves with different R values should collapse into one single curve when results are presented as $\mathrm{d}a/\mathrm{d}N$ vs. κ, as presented in Fig. 2.6. The best collapse is obtained when the correct ρ^* value is used. The driving force, κ, is calculated by using K_{max} and ΔK from the fatigue crack growth data in Eq. (2.21) and ρ^* is adjusted until the best collapse is obtained. The ρ^* adjustment affects the

value of K_r inEq. (2.21).

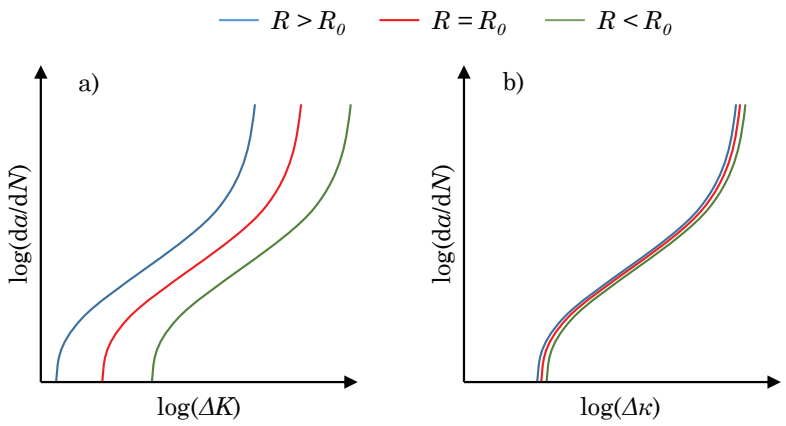

Figure 2.6. : Fatigue curves, a), with different stress ratios, R, will collapse to the single curve, b), when ρ^* is adjusted correctly.

Determination of the ρ^* Parameter from the Fatigue Limit and the Threshold Stress Intensity Factor range

Noroozi et al. [20] proposed that the ρ^* parameter can be determined by using the threshold SIF, ΔK_{th}, and the fatigue limit, $\Delta\sigma_{th}$.

The method is based on the assumption that the local stress range at the crack tip is equal to the fatigue limit, $\Delta\sigma_{th}$, when the threshold SIF, ΔK_{th}, is applied. Due to the fact that the fatigue limit is less than the material yield limit, the elastic stress-strain analysis can be carried out. Thus, according to the Creager-Paris solution, the two material properties can be related as:

$$\Delta\tilde{\sigma}^a_{th} = \frac{\Psi_{y,1}\Delta K_{th}}{\sqrt{2\pi\rho^*}} \tag{2.45}$$

Subsequently, the elementary material block size ρ^* can be determined.

$$\rho^* = \frac{(\Psi_{y,1})^2}{2\pi}\left(\frac{\Delta K_{th}}{\Delta\sigma_{th}}\right)^2 \tag{2.46}$$

Determination of the ρ^* Parameter from Grain Size Distribution

Remes et al. [62] presented a strain-based approach to model fatigue crack initiation and propagation. The model considers the fatigue crack growth as initiation of micro-cracks inside the homogenisation unit. The size of the homogenisation unit is described by the material characteristic length, l_0, and stresses and strains are considered to be constant within

the units.

The model is based upon similar assumptions as those made by Noroozi et al. [20]. Hence, the ρ^* parameter can be assumed to be equal to the material characteristic length, l_0. Remes et al. [62] suggested that l_0 is a function of the average grain size, $d_{g,50\%}$, and the parameter, c_g, which is dependent on the grain size distribution:

$$l_0 = c_g \cdot d_{g,50\%} \tag{2.47}$$

The parameter, c_g, is assumed to be the ratio between the grain size at a probability level of 99%, $d_{g,99\%}$, and the average grain size, d_g:

$$c_g = \frac{d_{g,99\%}}{d_{g,50\%}} \tag{2.48}$$

Therefore, ρ^* can now be determined from the grain size distribution using Eqs. (2.47) and (2.48):

$$\rho^* = l_0 = d_{g,99\%} \tag{2.49}$$

3. Crack Growth Model for Arbitrarily-shaped Planar Cracks

3.1 Introduction

In this chapter, the fatigue crack growth model for arbitrarily-shaped planar cracks is described. The purpose of this work is to study the fatigue behaviour of planar cracks. These cracks can be arbitrarily shaped and grow under non-uniform stress fields induced by variable amplitude loading.

Numerical implementation of a crack growth simulation procedure requires three steps: 1) computation of the SIF along the existing crack front, 2) crack growth increment calculation along the crack front and, 3) advancement of the crack front. These steps are repeated until predefined failure criteria are met. Consequently, a computer program has been developed by using the C++ programming language to perform these steps and to estimate the fatigue life.

SIFs are computed using the general point-load weight function method. The weight function in Section 2.1 is inaccurate when deep surface cracks are considered and, therefore, a new weight function for surface cracks has been proposed. In order to perform the calculations, the 2-D crack front and the external boundary of the component are modelled by using a finite number of points connected by linear segments, as shown in Fig. 3.1. The SIF is calculated at the middle of each linear segment.

The crack growth rate is calculated from SIFs by using the plasticity-based crack growth model described in Section 2.2. Computations for the crack tip plasticity require knowledge of the parameter, ρ^*, that describes the crack tip geometry. In many practical cases, the material data required to determine ρ^* are not available. Therefore, a new method for approximating ρ^*, based on elastic modulus and fracture toughness, has

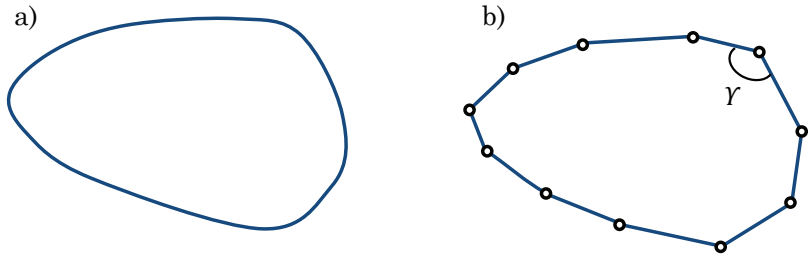

Figure 3.1. The continuous crack front, a), is replaced by a finite number of nodal points and linear segments, b).

been presented.

The SIF and the crack growth rate are calculated along the crack front. Based on the crack growth rates, the crack front is updated after each cycle. In order to advance the crack front of arbitrary shape, special algorithms have been developed. These algorithms are necessary since the discretization of the crack front can cause numerical errors.

3.1.1 Definitions

Crack Front Locations φ

Specific location at the crack front can be defined in different ways. The parametric angle φ Fig. 3.2 is often used when (semi-)elliptical cracks are considered.

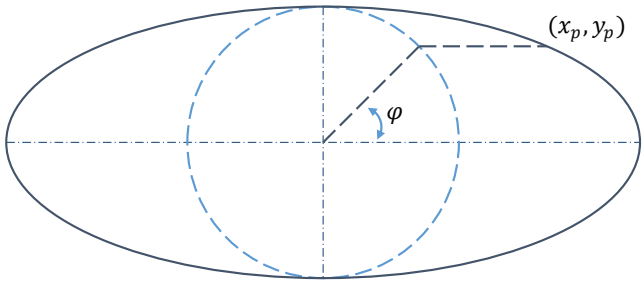

Figure 3.2. The crack front location (x, y) can be defined by using the parametric angle φ.

The Crack Aspect Ratio a/c

For an elliptical crack, the aspect ratio, a/c, refers traditionally to the ratio of the minor axis, $2a$, and the major axis, $2c$. However, a more general definition is needed when cracks of arbitrary shape are considered. In this work, the cracks are divided into two categories: embedded and surface

cracks. The following definitions for dimensions, a and c, are used:

Embedded:	$2a$	= dimension perpendicular to the largest dimension
($Fig.$ 3.3)	$2c$	= largest dimension of the crack
Surface:	a	= depth of the crack
($Fig.$ 3.4)	$2c$	= width of the crack

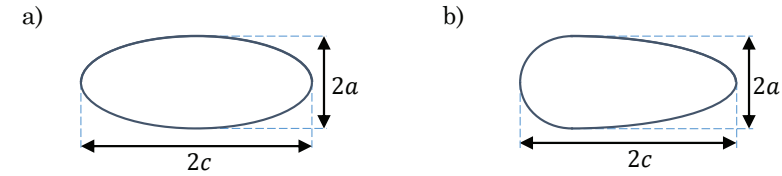

Figure 3.3. The a/c definition for **a)** an elliptical crack and **b)** an arbitrary embedded crack.

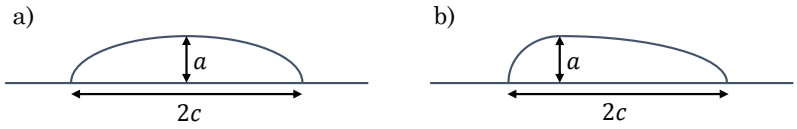

Figure 3.4. The a/c definition for **a)** a semi-elliptical crack and **b)** an arbitrary surface crack.

3.2 Stress Intensity Factor Calculations

In the method proposed, the mode I SIF is the driving force that controls the fatigue crack growth. The traditional methods used for calculation of the SIF, such as the handbook solutions or the specific weight functions, are not suitable when arbitrary cracks are considered. Therefore, the more advanced method for the computation of the SIF along the arbitrary crack front was needed.

Consequently, the general point-load weight function, presented in Section 2.1, was chosen as the method for calculating the necessary SIFs. The general point-load weight function which can be used with arbitrarily-shaped cracks, is a powerful method for the calculation of SIFs for growing cracks [43, 44]. The weight function method uses the stress field of the

un-cracked body, so there is no need to re-calculate the stress field while the crack advances [35, 63]. Hence, calculation of the SIF is computationally efficient and very rapid, in comparison to any FEA-based method.

The general point-load weight function is accurate when embedded cracks are considered. However, Glinka and Reinhardt [44] pointed out that Eq. (2.6) neglects the additional local bending that occurs in the presence of surface cracks. The effect of local bending contributes significantly when the depth of the crack is approximately 10% of the thickness. Therefore, a new weight function is needed to compensate for this effect.

3.2.1 Overview of the Stress Intensity Factor Calculations

The SIF calculation includes the following steps explained in detail below:

1. The crack area is divided into small rectangular or triangular segments.

2. The stress fields over the rectangular or triangular segments are replaced by discrete point loads, positioned at the middle of the each segment.

3. The SIF induced by a single point load is calculated by using the general point-load weight function.

4. The total SIF is obtained by calculating the sum of contributions from each point load.

5. The SIF of the free surface is corrected by using the presented technique, if a surface crack is considered.

3.2.2 New Weight Function for Surface Cracks

The weight functions are derived from existing SIF solutions. In this case, requirements for the reference solution are that the local bending effect should be included and the closed form solution exists. The solution for double-edged cracks under a single-line load, as found in existing literature [34], fulfil these requirements. The exact solution is:

$$K_I = \frac{F}{\sqrt{\pi w}} \sqrt{v^2 - w^2} \left(\frac{1}{v - w} + \frac{2}{w} \right) \tag{3.1}$$

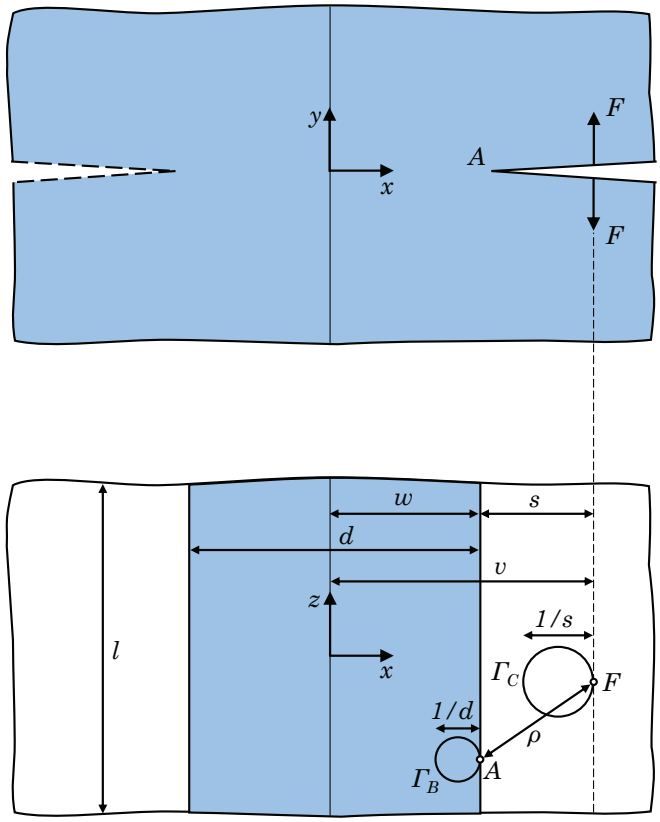

Figure 3.5. Double-edged crack.

The new weight function is obtained by comparing the current weight function, Eq. (2.6), and the exact solution, Eq. (3.1). Equation (2.6), can be solved in closed form because the crack line and the free boundary are straight lines and, therefore, the inverted contours, Γ_C and Γ_B, are circles. The diameters of these circles are $D_C = 1/s$ and $D_B = 1/d$, as illustrated in Fig. 3.5. Therefore, the inverted crack contours are:

$$\begin{aligned} \Gamma_C &= \pi D_C = \frac{\pi}{s} \\ \Gamma_B &= \pi D_B = \frac{\pi}{d} \end{aligned} \tag{3.2}$$

The weight function for the problem is obtained when Eq. (3.2) is combined with Eq. (2.6):

$$w_A(x_p, y_p) = \frac{\sqrt{2s}}{\pi^{3/2}\rho^2}\sqrt{1+\frac{s}{d}} \tag{3.3}$$

The SIF at point A is obtained by integrating Eq. (3.3) along the line load:

$$K_{I,wf} = \oint_{x=b} \frac{\sqrt{2s}}{\pi^{3/2}\rho^2}\sqrt{1+\frac{s}{d}}\mathrm{d}z = \frac{F\sqrt{2}}{\sqrt{\pi s}}\sqrt{1+\frac{s}{d}} \tag{3.4}$$

If the notation of Eq. (3.4) is changed to correspond to Eq. (3.1), the SIF can be written as:

$$K_{I,wf} = \frac{F}{\sqrt{\pi w}}\frac{\sqrt{v^2-w^2}}{v-w} \tag{3.5}$$

The obtained SIF, Eq. (3.5), is exactly the first term of the reference solution Eq. (3.1). Hence, the local bending effect is the second part of the solution, Eq. (3.1), which is missing in the current general weight function.

The missing part can be re-written by using the notation of Eq. (2.6):

$$K_I = \frac{2F\sqrt{v^2-w^2}}{w\sqrt{\pi w}} = \frac{4F\sqrt{2s}}{d\sqrt{\pi}}\sqrt{1+\frac{s}{d}} = \frac{4F\sqrt{2}}{d}\frac{\sqrt{\Gamma_C+\Gamma_B}}{\Gamma_C} \tag{3.6}$$

The problem lies in finding a weight function that produces this SIF after integration along the line load. The integration along the infinite line load yields an infinite load, $l \cdot F$. However, since the SIF is a finite value and the term, l, gets eliminated from Eq. (3.6), l must therefore vanish during the integration. The following function satisfies this criteria:

$$wf = \frac{4\sqrt{2}}{ld}\frac{\sqrt{\Gamma_C+\Gamma_B}}{\Gamma_C} \tag{3.7}$$

In Eq. (3.7), the term, $l \cdot d$, represents the area of the un-cracked ligament. Hence, the equation links the local bending contribution and the un-cracked area, A_{uc}. This is reasonable because the un-cracked area resists bending and Eq. (3.7) vanishes if the crack is located in an infinite plate. Finally, the function can be written in a more general form:

$$wf = \frac{4\sqrt{2}}{A_{uc}}\frac{\sqrt{\Gamma_C+\Gamma_B}}{\Gamma_C} \tag{3.8}$$

However, more careful study of Eq. (3.8) indicates that A_{uc} in Fig. 3.6 works only with edge cracks. In the case of semi-elliptical surface cracks in a semi-infinite body, A_{uc} gets an infinite value and, therefore, the local

bending effect disappears. However, the results presented later in Section 4.1.2 indicate that the local bending effect should not totally disappear.

Additional numerical studies of SIFs in Section 4.1.2 indicate that A_{luc}, the local intact area which surrounds the crack, should be used instead of A_{uc}. The size of A_{luc} seems to be dependent on the a/c and a/t ratios. In the case of an edge crack, A_{luc} reaches its maximum value that is equal to A_{uc}. Correspondingly, a semi-circular crack yields the second maximum for A_{luc}. Based on these observations, the approximation for A_{luc} has been proposed. The expression for A_{luc} is written in a form similar to that used for many empirical SIF equations:

$$A_{luc} = A_l \cdot M_1 \cdot M_2 \tag{3.9}$$

where

$$A_l = 2c \cdot t - A_{crk} \tag{3.10a}$$

$$M_1 = 1 - \frac{a}{c}\left(\frac{a}{t}\right)^{0.5} \tag{3.10b}$$

$$M_2 = \exp\left[5.286\left(\frac{a}{c}\right)^{0.7469}\right] \tag{3.10c}$$

$$A_{crk} = \text{crack area} \tag{3.10d}$$

This solution is derived based on the SIF data from semi-elliptical cracks with aspect ratios, a/c, between 0.1 and 1.0. This is the range where the weight function solution presented in Section 3.2 is accurate. When this approximation is used, one should always verify that Eq. (3.9) does not exceed the area of the cross-section. This can happen if the cross-section is not rectangular.

The complete weight function for surface cracks is subsequently obtained by combining Eqs. (2.6) and (3.8):

$$w_A(x_p, y_p) = \frac{\sqrt{2}}{\pi\rho^2}\frac{\sqrt{\Gamma_C + \Gamma_B}}{\Gamma_C} + \frac{4\sqrt{2}}{A_{luc}}\frac{\sqrt{\Gamma_C + \Gamma_B}}{\Gamma_C} \tag{3.11}$$

3.2.3 Numerical Integration

The SIF in the presented model is calculated by using Eq. (2.3). The weight function used in the equation depends on the type of crack. The weight function of Eq. (2.6) is used for embedded cracks and Eq. (3.11) for surface cracks.

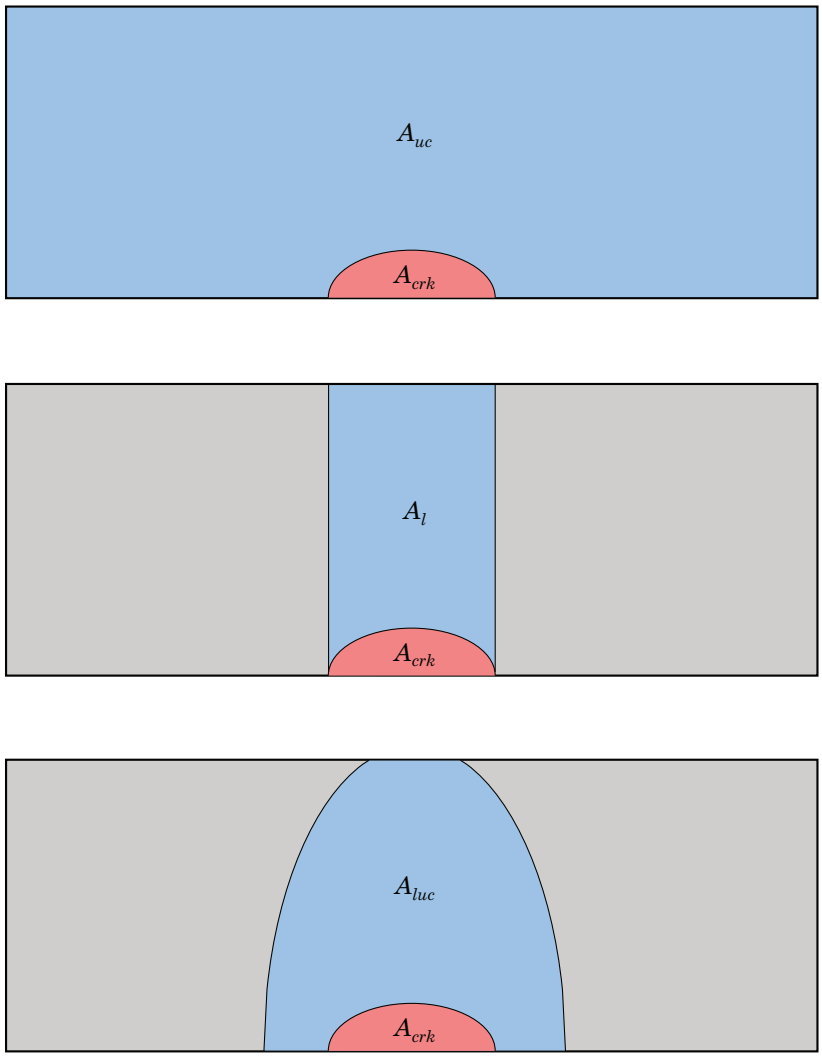

Figure 3.6. The parameters, A_{crk}, A_{uc}, A_l and A_{luc}, that are used to define the size of the un-cracked area contributing to local bending.

The integration of Eq. (2.3) was performed numerically and required discretization of the problem. The crack front and the external boundary were approximated by using a finite number of points and linear segments, as shown in Fig. 3.1. The weight function is singular at the crack front and, therefore, the most accurate point for calculation of the SIF is the centre of each segment. The nodal points between the segments are the corner points, hence integration at these points would be more complex.

Jankowiak et al. [47] studied the influence of the angle, γ, between two adjacent segments for semi-elliptical cracks, concluding that the angle should be at least at 170°. An increase of the angle beyond 174° would only slightly improve accuracy, but computation time would increase significantly. The general conclusion is that 60 segments are enough for an embedded elliptical crack and 30 segments for a semi-elliptical surface crack. It must be noted that this proposed limit of 170° may not always be practical for arbitrary cracks, e.g., for rectangular cracks.

The crack area was divided into n small rectangular and triangular regions, and stress fields influencing each region was replaced by a discrete point load positioned in the middle of the regions. The SIF in the middle of the j^{th} segment was obtained by calculating the sum of the contributions from each point load.

$$K_j = \sum_{i=0}^{n} \left\{ \frac{F_i\sqrt{2}}{\pi\rho_i^2} \frac{\sqrt{\Gamma_{C,i} + \Gamma_{B,A}}}{\Gamma_{C,i}} \right\} \tag{3.12}$$

where F_i is the magnitude of the i^{th} point load, l_i is the distance between the i^{th} position of the point load and the middle point of the j^{th} segment, $\Gamma_{C,i}$ is the length of the inverted crack contour with respect to the i^{th} point load position, and $\Gamma_{B,A}$ is the length of the inverted boundary contour with respect to the middle point of the j^{th} segment, as illustrated in Fig. 3.7.

3.2.4 Surface Boundary Layer Correction

Hartranft and Sih [64] proposed that the classic SIF associated with the $1/\sqrt{r}$ singularity decreases rapidly near the free surface and equals zero at the free surface. Raju and Newman [65] studied this thin surface boundary layer by using the FEA method and concluded that the SIF near the free surface is greatly dependent on mesh size.

Similar problems occur when the general point-load weight function is used. The SIF near the free surface is very sensitive to the scheme, e.g.,

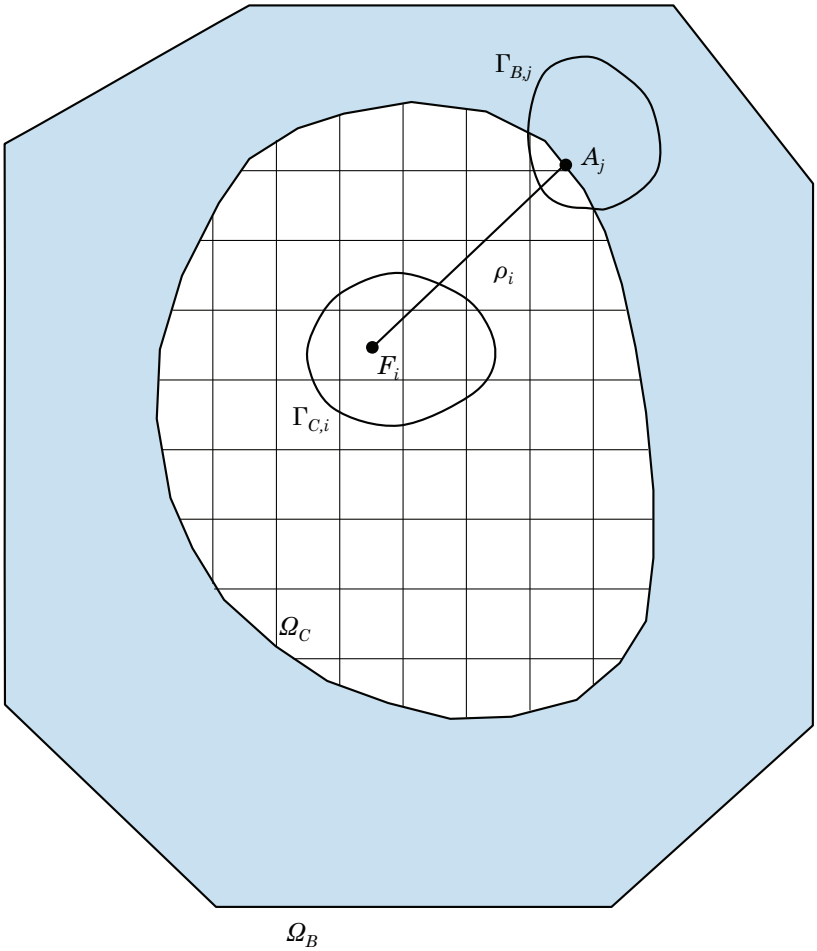

Figure 3.7. Approximation of the crack area with rectangular and triangular regions.

the orientation and length of the segments. Even if the initial geometry is constructed carefully, the accuracy of the SIF calculation may decrease during the simulation because the crack geometry continuously changes due to crack growth. This problem was solved by developing a special rule to obtain the SIF close to the free surface.

According to the rule presented in this work, the SIF at points located within the region, $0 < \varphi < \pi/64$, are approximated by a quadratic equation:

$$K(\varphi) = A_1 \cdot \varphi^2 + A_2 \cdot \varphi + A_3 \tag{3.13}$$

The coefficients in Eq. (3.13) are determined based on three SIFs, obtained at points located further away from the free surface. These points are the closest points to the free surface, but are located outside of the surface layer, i.e., $\varphi > \pi/64$.

For example, in Fig. 3.8, the segments (middle points), C_1 and C_2, are positioned inside of the surface layer ($\varphi < \pi/64$). Respectively, the segments, C_3, C_4 and C_5, are located outside of the surface layer ($\varphi > \pi/64$) and, are therefore used to calculate the coefficients, A_1, A_2 and A_3 in Eq. (3.13).

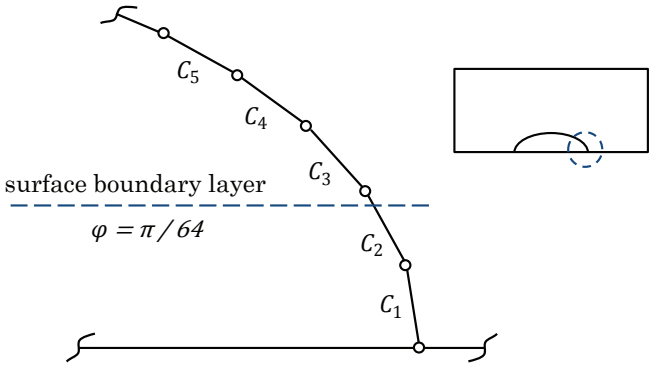

Figure 3.8. Segments near the free surface.

3.3 Calculation of the Fatigue Crack Growth Rate

In order to model the fatigue crack growth during each cycle, the crack growth rate along the crack contour must be calculated. In this work, the crack growth rate is computed from the SIF by using the selected crack tip plasticity-based fatigue crack growth law, as presented in Section 2.2.

The model is capable of accounting for variable amplitude loading effects such as retardation, acceleration and stress ratio. The crack growth retardation occurs because of the local residual stresses induced by the cyclic-plastic deformation ahead of the crack tip. The chosen crack growth model is derived from the widely-accepted principles and assumptions of fracture mechanics and fatigue and, as such, has a strong theoretical foundation.

The important feature of the crack growth model is the blunted crack tip with the radius of ρ^*. Methods for the determination of ρ^* have been developed and are discussed in Section 2.2.7. On occasion, those methods may prove unfeasible because the required material data may not be available. As a result, the new method for determining the ρ^* parameter is presented in this chapter. Since several different methods are available for the determination of ρ^*, one can select the best approach based on the material information available.

The fatigue crack growth laws based on linear-elastic fracture mechanics assume that the SIF, K, or the driving force equivalent to K, uniquely describes the crack growth rate. However, this similitude concept does not apply to small cracks. Thus, the growth of small flaws was also studied and, consequently, the crack growth rate of the small cracks was corrected by modifying the SIF, based on crack size.

3.3.1 Overview

The calculation of the fatigue crack growth rate includes the following steps, as explained in detail below:

1. The SIF is modified by using the small crack correction.

2. The residual SIF is calculated from the residual stress field generated around the crack tip.

3. The fatigue crack growth driving force is composed of the SIF range and the maximum SIF.

4. The crack growth increment is calculated from the driving force.

5. The residual stress field generated in the crack tip region is updated after each loading cycle.

3.3.2 Driving Force and Crack Growth Increment

According to the adopted crack growth model, the fatigue driving force, κ, consists of three SIF value; - K_{max}, ΔK and K_r. The SIFs, K_{max} and ΔK, represent the effect of the applied load, and K_r results from the local residual stress field induced by the plastic deformation at the crack tip.

The effect of the global residual stress (e.g., as generated during the manufacturing process) is also included, if necessary, and is denoted as the global residual SIF, K_R. It is assumed that the K_R is independent of the applied cyclic load.

The SIFs, K_{max}, ΔK and K_R, are obtained by using the general point-load weight function. K_{max} and ΔK are calculated by using the stress field induced by the unit load, and the SIF which is derived is scaled by using the loading history. The global residual SIF K_R, which results from the global residual stress field, is used without any scaling or fluctuation. The local residual SIF K_r is computed from the local residual stress field ahead of the crack tip by using the simplified weight function, as well as the local residual stresses which result from cyclic-plastic deformation around the crack tip.

After including all effects, i.e., the applied cyclic stress, the local crack tip residual stress and the global residual stress, the fatigue driving force is determined:

$$\kappa = (K_{max} + K_R + K_r)^p \, (\Delta K + K_r)^{1-p} \tag{3.14}$$

The global residual SIF, K_R, is applied only to $K_{max,tot}$. This means that the loading is shifted by K_R, while the range of loading remains unchanged. This behaviour is similar to that presented by Cheng et al. [66]. K_r is applied to both $K_{max,tot}$ and ΔK_{tot}, as presented by Mikheevskiy [22]. The influence of the residual SIFs is detailed in Fig. 3.9.

The fatigue crack growth increment, $\mathrm{d}a$, induced by a loading cycle, is obtained from the driving force and the fatigue crack growth expression derived earlier:

$$\frac{\mathrm{d}a}{\mathrm{d}N} = C \left[(K_{max} + K_R + K_r)^p \, (\Delta K + K_r)^{1-p} \right]^m \tag{3.15}$$

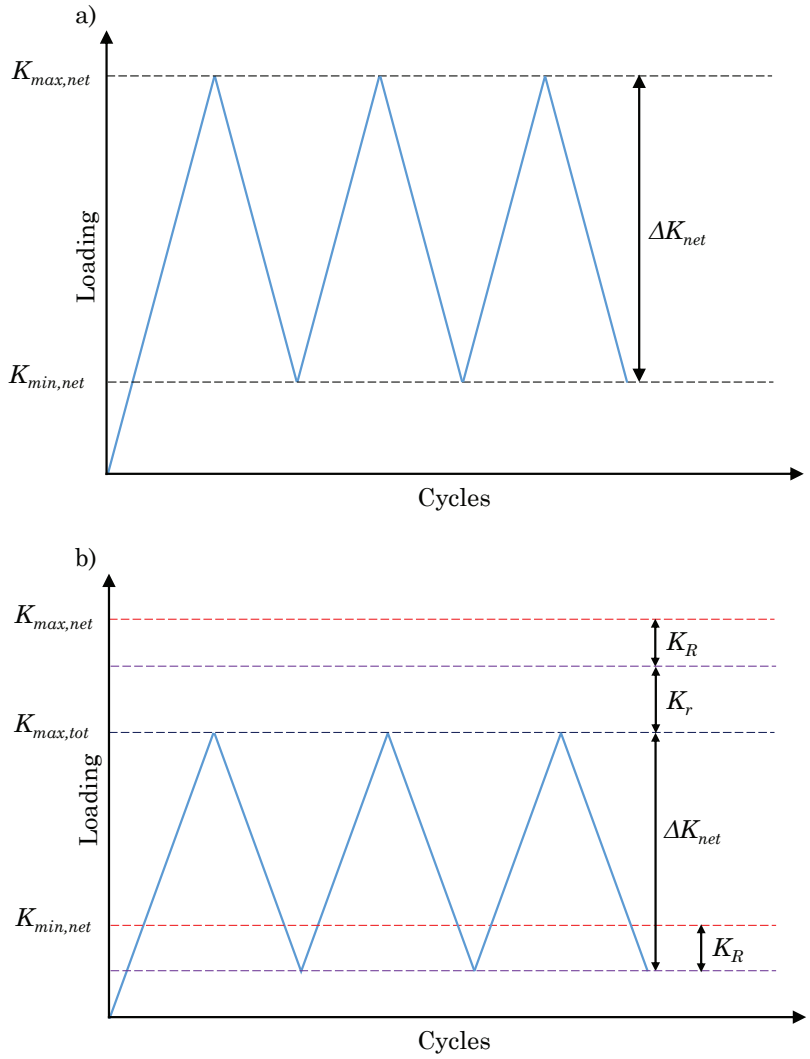

Figure 3.9. a) Actual applied loading cycles. b) Effective loading cycles when a global residual SIF, K_R, and a local residual SIF, K_r, are taken into account. In this case, a negative K_R is applied.

3.3.3 Fatigue Crack Growth Parameters C and m

The crack growth increment equation, Eq. (3.15), is derived by dividing the material behaviour at the crack tip into two modes, predominantly elastic and predominantly plastic. The predominantly elastic material behaviour is assumed in the near-threshold region and, accordingly, the predominantly plastic behaviour is present in the Paris region.

The fatigue crack growth constants, C and m in Eq. (3.15), depend on the dominant strain component. The division into elastic and plastic behaviours means that the fatigue crack growth curve is defined piece-wise (Fig. 3.10) and the fatigue driving force, Eq. (3.14), determines which constants are to be used.

The fatigue constants, C_1 and m_1 or C_2 and m_2, can be obtained from experimental data, or by using Eqs. (2.43) and (2.44) respectively. The fatigue curve in Fig. 3.10 is comprised of two linear pieces in log-log coordinates. Sometimes, more than two pieces are needed to obtain a more accurate fatigue curve. The number of fatigue crack growth curve pieces is not limited.

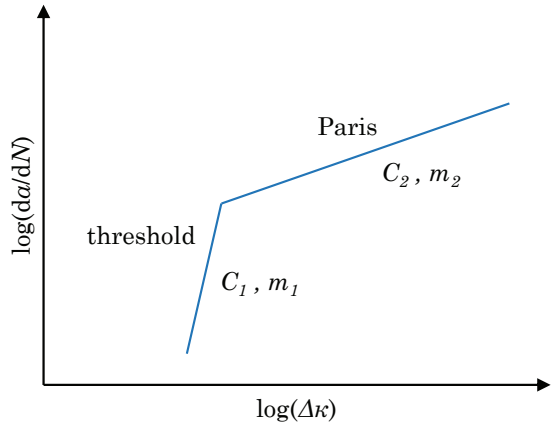

Figure 3.10. Fatigue crack growth curve.

3.3.4 Correction for the Small Crack Effect

In the presented method, a crack is considered as a small crack if the size is comparable to the ρ^* material parameter. Under the same nominal SIF, K, the growth rates of short cracks are greater than those of long cracks. Therefore, the concept of similitude is not valid for small cracks and this small crack effect must be taken into account.

The stress field ahead of a crack tip is computed in the analysed model by using the Creager-Paris solution [56]:

$$\sigma_{cp} = \frac{2K}{\sqrt{\pi\rho^*}} = \frac{2S\sqrt{\pi a}}{\sqrt{\pi\rho^*}} \tag{3.16}$$

However, the actual stress field from a classic elliptical notch solution is:

$$\sigma_{actual} = S\left(1 + 2\sqrt{\frac{a}{\rho^*}}\right) \tag{3.17}$$

Thus, the ratio between the fracture mechanics, crack tip solution and the actual elliptical solution is:

$$\frac{\sigma_{actual}}{\sigma_{cp}} = 1 + \frac{1}{2}\sqrt{\frac{\rho^*}{a}} \tag{3.18}$$

Hence, the SIF should be corrected by this difference, in order to obtain the actual stress field of the blunted crack tip:

$$K_{eff} = K\left(1 + \frac{1}{2}\sqrt{\frac{\rho^*}{a}}\right) \tag{3.19}$$

Equation (3.19) provides the relationship between the crack length and the fatigue crack driving force, applicable to both short and long cracks. As shown in Fig. 3.11, the small crack correction causes a significant increase in the SIFs for small cracks, while the SIFs for long cracks remain almost unaffected. This corresponds to experiments which demonstrate that similitude is valid for long cracks, but not for small cracks. The maximum $K_{eff}/K = 1.5$ ratio is obtained when $a/\rho^* = 1.0$ because $a \geq \rho^*$. Cracks smaller than ρ^* parameter are assumed as non-propagating cracks.

3.3.5 New Method of Determine ρ^*

The crack growth model being used is based on the assumption that the ρ^* parameter is the smallest material feature to which continuum mechanics can be applied; hence, the cracks smaller than ρ^* do not have any influence on the bulk strength of the material. Consequently, despite the possible existence of flaws smaller than ρ^*, the strength of the material is equal to the theoretical strength, as shown in Fig 3.12. The assumption is similar to the properties which result from the Kitagawa diagram [67].

The new method for the determination of the ρ^* parameter is based

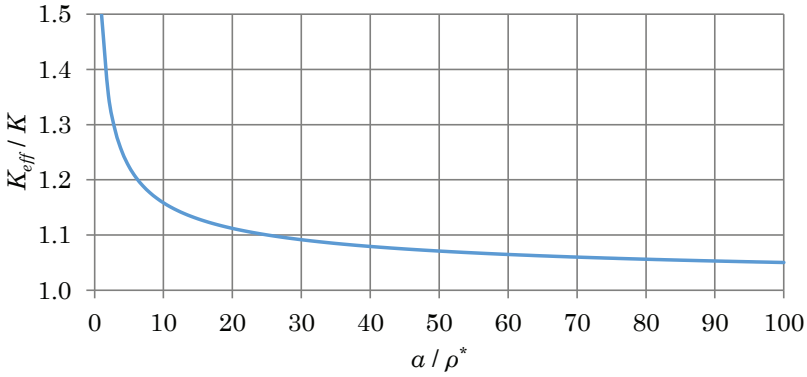

Figure 3.11. Correction for the small crack effect.

on the theoretical strength and fracture toughness of the material being analysed. The method is based on an assumption that the fracture toughness, K_{IC}, is reached when the material contains a crack of the size, ρ^*, and the applied stress is equal to the theoretical strength of the material being analysed. The assumption is similar than a method presented by Taylor [68] to determine critical distances.

$$K_{IC} = \sigma_{thr}\sqrt{\pi\rho^*} \tag{3.20}$$

Thus, the smallest effective flaw size, ρ^*, can be determined from Eq. (3.20):

$$\rho^* = \frac{K_{IC}^2}{\pi\sigma_{thr}^2} \tag{3.21}$$

If the theoretical strength of the material is unknown, the lower limit can be approximated from the modulus of elasticity [69]. The theoretical strength in this work is determined as:

$$\sigma_{thr} = \frac{E}{10} \quad \text{for steels} \tag{3.22a}$$

$$\sigma_{thr} = \frac{E}{15} \quad \text{for aluminum alloys} \tag{3.22b}$$

3.3.6 Calculations of the Local Residual Stress Intensity Factor

The local residual SIF is calculated based on the local residual stress field generated after each loading cycle. The local residual stress field is obtained from Eq. (2.18). The following steps are completed to obtain the

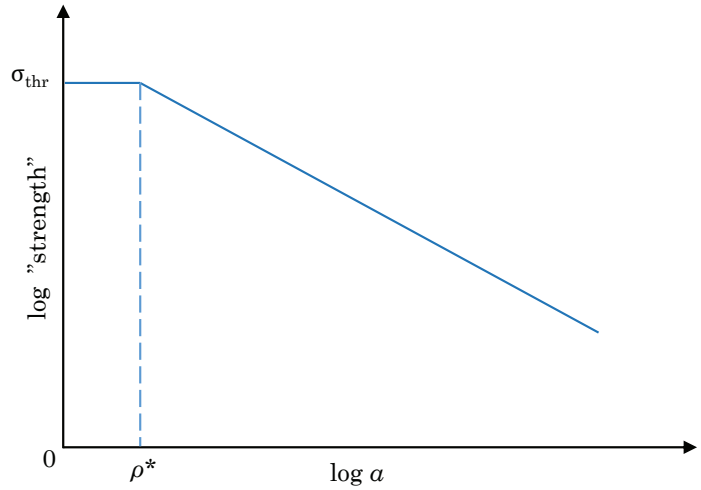

Figure 3.12. The effect of the flaw size on the strength of the material.

residual SIF, K_r:

1. The linear-elastic stress distribution, $\sigma(x)^e_{max}$, ahead of the crack tip was obtained from the $K_{max,net}$ SIF by using the Creager-Paris solution, Eq. (2.13). The material parameter, ρ^*, was used as a crack tip radius.

2. The actual maximum elastic-plastic stress distribution, $\sigma(x)^a_{max}$, was calculated from the linear-elastic stress distribution by using the multiaxial Neuber rule, Eq. (2.16).

3. The actual elastic-plastic stress range distribution, $\Delta\sigma(x)^a$, was calculated from ΔK, Eqs. (2.13) and (2.17).

4. The residual stress distribution generated ahead of the crack tip during the i^{th} cycle was calculated as $\sigma(x)^i_r = \sigma(x)^a_{max} - \Delta\sigma(x)^a$, Eq. (2.18).

5. The overall residual stress distribution was obtained by combining all stress distributions generated during the previous cycles. It is important to note that superposition was not employed to combine stress fields. If multiple distributions overlapped at the same position, x, then the highest compressive stress was used.

6. The K_r was calculated by using the weight function method. In this particular case, the weight function was integrated over a specified resid-

ual stress field behind the crack tip, Eq. (2.20).

The general idea of obtaining the residual stress distribution and the residual SIF is presented in Fig. 3.13. Green indicates the stress fields that affect the residual SIF at the current crack tip location. The crack tip has already moved out of the red stress fields and, therefore, those are neglected in the analysis. The yellow stress field is excluded because it is located inside of the bigger stress field introduced by the overload. Purple denotes the stress field that is introduced by the current cycle. This stress field region becomes effective as soon as the crack tip has grown into it. The blue stress fields will eventually be generated during upcoming cycles, but are not yet present at the current position of the crack tip.

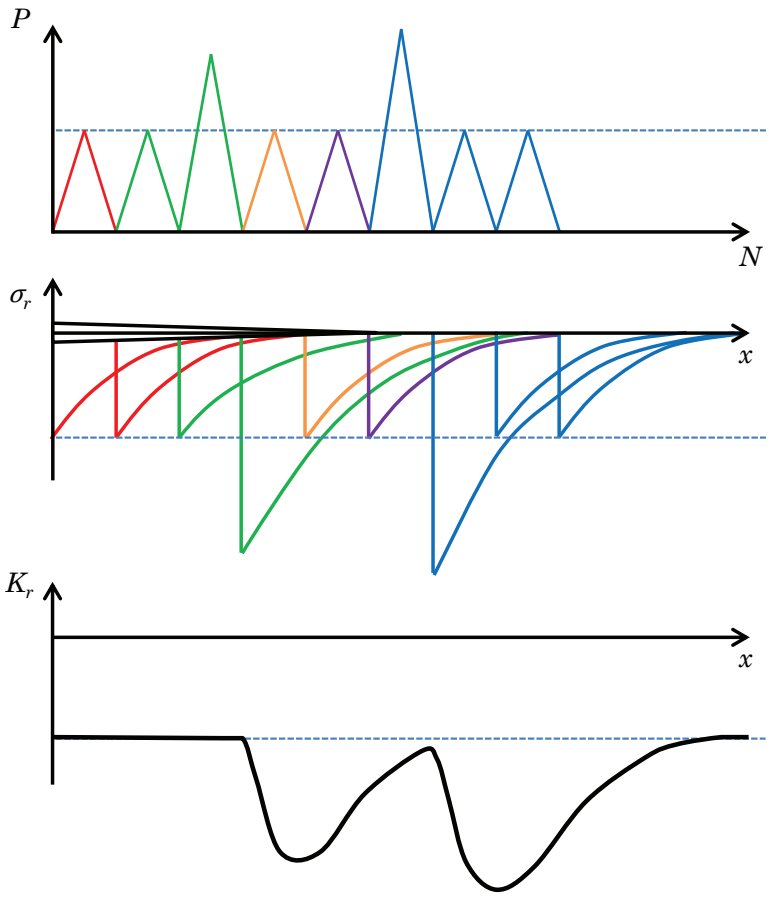

Figure 3.13. The residual stress field ahead of the crack tip.

3.4 Crack Front Propagation

In traditional 1-D or simplified 2-D fatigue crack growth analysis, the crack is described by using only one crack dimension, and the actual geometry of the crack is not needed. Therefore, it is a very straightforward task to advance the crack by increasing the crack length by crack growth increments. When arbitrarily-shaped 2-D cracks are considered, the actual geometry needs to be known and the direction of the crack growth has to be defined along the crack front. Thus, modelling of the crack front propagation becomes more complex.

The arbitrary planar cracks are defined by using a finite number of nodal points and linear segments and the SIF is calculated at the middle of the segments. Therefore, the most obvious method would be to move each segment by a parallel shift into the direction of the normal vector. However, this method restricts the development of the crack front because the rotation of the segment is excluded. This may cause a modelling error if the final crack shape differs significantly from the initial crack shape. In order to solve this problem, several different approaches have been developed [29, 31, 47, 70, 71].

In order to model the growth of a planar fatigue crack, two varying methods for the propagation of the crack front have been developed. In both methods, the nodal points are moved, based on the crack growth rate and the orientation of the adjoining segments, in a similar fashion as presented by Nykänen [71]. After all nodal points are shifted, a cubic spline is fitted through those points. The nodal points are adjusted along the spline so that all segments between the points are of equal length. The equal length of the segments helps the crack front to remain smooth. The idea of the spline fitting is based on the work of Lin and Smith [29].

A high fatigue crack growth exponent, m in Eq. (3.15), can induce considerable variation in the crack growth rates at the adjoining segments and, therefore, it may cause additional problems when segments are moved. This is discussed further in the following section.

3.4.1 Overview

1. The nodal points are moved, based on the crack growth rate and the orientation of adjacent segments.

2. A cubic spline is fitted through the nodal points.

3. The nodal points are adjusted uniformly along the spline.

4. New crack front segments are fitted between the nodal points.

3.4.2 Nodal Point Movement - Method #1

This method aims to model the natural propagation of the crack front without any simplifications. The propagation of the crack is achieved by moving the nodal points, instead of moving entire linear segments. Each segment is connected to two nodal points and therefore, the movement of the nodal points defines the translation and rotation of the segment. This enables unconstrained development of the crack front.

However, it was described in the previous section that the SIF and crack growth rate are calculated at the middle of each segment, rather than at the nodal points. As a result, the approach presented by Nykänen [71] is used to define the nodal point movement.

According to the approach of Nykänen [71], the shift of the nodal point is calculated by using the increment vectors of adjoining segments. In Fig. 3.14, the length of the i^{th} segment increment vector, $\overline{\boldsymbol{d_s}}_{,i}$, is equal to the crack growth increment, da_i, at the middle of the corresponding segment:

$$\|\overline{\boldsymbol{d_s}}_{,i}\| = da_i \tag{3.23}$$

Accordingly, the direction of the vector of the increment, $\overline{\boldsymbol{d_s}}_{,i}$, is equal to the normal unit vector, $\hat{\boldsymbol{n_s}}_{,i}$, of the segment:

$$\frac{\overline{\boldsymbol{d_s}}_{,i}}{\|\overline{\boldsymbol{d_s}}_{,i}\|} \cdot \hat{\boldsymbol{n_s}}_{,i} = 1 \tag{3.24}$$

The increment vector of the nodal point, $\overline{\boldsymbol{d_p}}$, is calculated as the vector sum of the increment vectors of two adjoining segments, $\overline{\boldsymbol{d_s}}_{,i}$ and $\overline{\boldsymbol{d_s}}_{,j}$:

$$\overline{\boldsymbol{d_p}} = \frac{1}{2}\left(\overline{\boldsymbol{d_s}}_{,i} + \overline{\boldsymbol{d_s}}_{,i+1}\right) \tag{3.25}$$

The vector, $\overline{\boldsymbol{d_p}}$, defines the direction and magnitude of the nodal point movement. After the nodal point movement, the spline fitting method described in Section 3.4.4 is applied to create a uniform crack front.

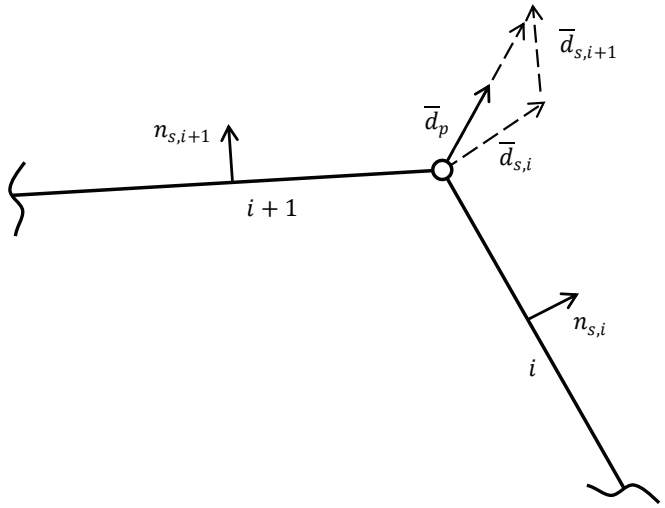

Figure 3.14. Nodal point movement.

3.4.3 Nodal Point Movement - Method #2

The crack front in the second method is simplified by using only four control points to define the crack shape. The crack front is advanced as described above, but only four points are used to fit the cubic spline and define the crack front line. The method can be used when an elliptical crack is considered to sufficiently approximate the crack shape. In such a case, the end points of the minor and major axes are the control points.

The advantage of this method is that the shape of the crack front remains very smooth and convex. Therefore, the front develops both smoothly and uniformly. This prevents bad crack fronts and, hence, the numerical problems related to bad crack shapes are avoided.

In practice, the nodal points, other than the control points, are moved slightly faster than computed crack growth rates indicate. Therefore, this method yields more conservative fatigue lives than obtained with method #1. The method is also faster because the SIF is needed only at the segments adjacent to the control points.

This method is similar to methods presented in other studies Ref. [39]. The previously-presented methods usually assume that the crack remains (semi-)elliptical. The SIF is then calculated by using specific weight functions or solutions from handbooks. The limitation of these solutions is that only a one-dimensional stress field can be considered. There is no such limitation in the method presented in this thesis. Therefore, one can

apply the method presented here to more complex crack problems.

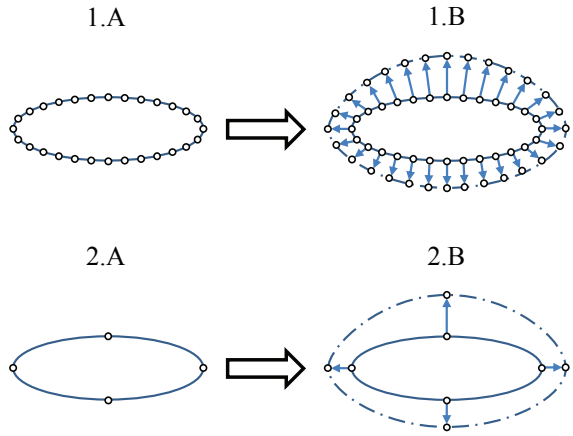

Figure 3.15. Crack front advance. 1.A: The previous method describes the crack by using several points along the crack front. 1.B: These points are moved during the cycle and a new crack front is formed. 2.A: The new method defines the crack front by using 4 points and a cubic spline. 2.B: During each cycle, only these four points are moved and a new spline is fitted.

3.4.4 Spline Fitting

The length of segments change during fatigue simulation, due to the increasing crack size. Ideally, the length of each segment should increase uniformly, but unfortunately, this only happens when a circular crack under a uniform stress field is considered. In all other cases, the SIF distribution along the crack front is not uniform and, as a consequence, segments are growing at various rates.

The fact that segments are of different lengths means that the discretization is not uniform, thus, the numerical error resulting from the discretization varies along the crack front. This may lead to cracks shaped differently than those which occur in reality.

In order to maintain equal length segments, the crack front is re-defined after the nodal point shift. The re-definition is achieved by fitting a cubic spline through the new nodal points. The spline is divided into segments of equal length. The intersections of these segments define the actual locations for the nodal points. The distance over which the nodal points move due to such an operation is relatively small. Nevertheless, the spline fitting helps to maintain a smooth and realistic crack shape.

3.4.5 Near-Threshold Region

The exponent, m, in Eq. (3.15) can attain high values in the threshold region and, therefore, even a small change of ΔK significantly affects the crack growth rate, da/dN. Since the SIF always varies along the crack front, Eq. (3.15) gives a very steep da/dN gradient along the crack front, when crack growth occurs in the threshold region.

An elliptical crack in an infinite body was studied as an example. The a/c aspect ratio of the ellipse was 0.5 and a uniform stress field was applied. The SIF was calculated by using Irwin's analytic solution [72]. The crack growth rate was obtained from Eq. (3.15) using the material constants $C_1 = 1.0$ and $m_1 = 20.0$ for the threshold region and $C_2 = 1.0$ and $m_2 = 3.0$ for the Paris region, as seen in Fig. 3.10.

In such a case, the ratio of the maximum and minimum SIFs along the crack front is $K_{max}/K_{min} = 1.41$. The ratios of the respective maximum and minimum crack growth increments are $da_{max}/da_{min} = 1024$ when m_1 is used, and $da_{max} = 2.8$ with the m_2 exponent. The SIF and crack growth increment distributions along the crack front are presented in Fig. (3.16).

According to the numbers represented by these figures, the crack advance at different points along the crack front can vary by a factor more than one thousand during a cycle when crack growth in the threshold region is considered. Therefore, numerical errors can occur when the crack front is described by using linear segments and these segments are moved based on the crack growth rates. The errors occur when the movement rate of the adjoining segments differs significantly.

These numerical problems can be avoided by using simplified method to advance the crack front (method #2). When crack growth shifts from the threshold region to the Paris region, current segments can be held and the method without simplifications used (method #1). This should be done if a complex stress field is applied. Both methods to model and advance the crack front are illustrated in Fig. 3.15.

3.5 The Summary of the Model Implementation

During one cycle, the following steps are performed and repeated until pre-defined failure criteria are met.

- The SIF is calculated at the middle of each segment, using the general

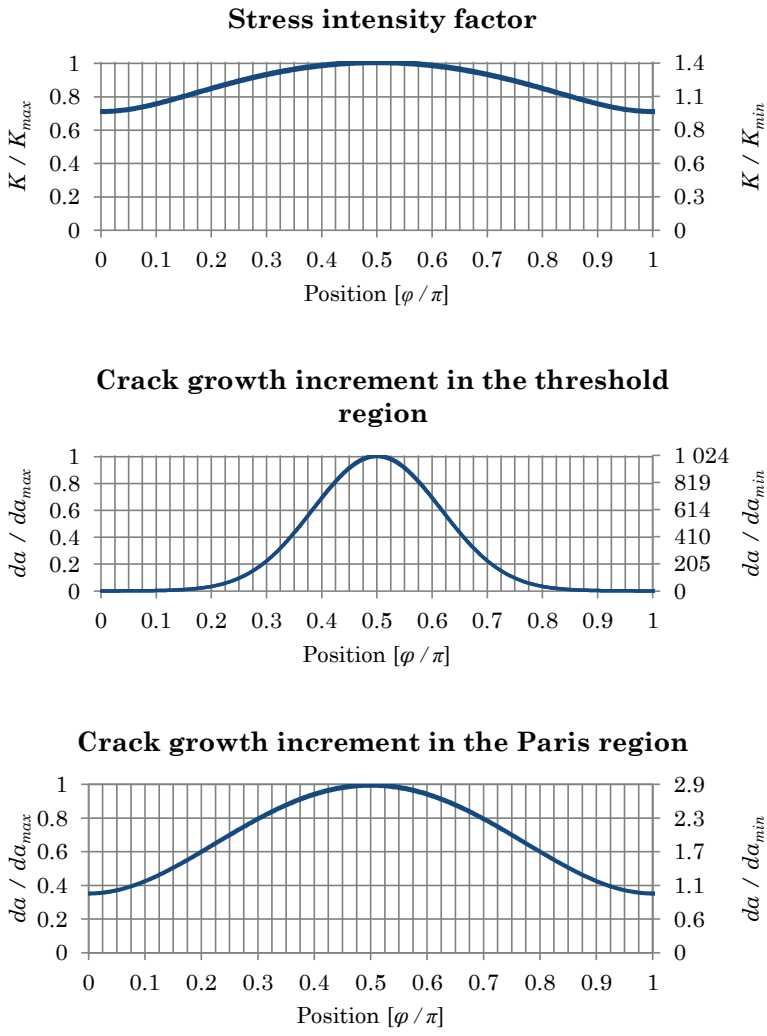

Figure 3.16. SIF and crack growth increment distributions along the crack front.

point-load weight function, Eqs. (2.6) and (3.11). The SIF is calculated for the unit load and scaled by load level associated with the current cycle.

- The correction for the small crack effect as in Eq. (3.19) is used to correct the SIF.

- The global residual SIF is calculated at the middle of each segment, using the general point-load weight function, Eqs. (2.6) and (3.11). The global residual SIF is not influenced by the loading history.

- The local residual SIF due to crack tip plasticity is calculated, Eq. (3.15).

- The crack growth rate at the middle of each crack segment is computed using the crack tip plasticity based fatigue crack growth law.

- The new local residual stress field ahead of the crack tip is computed.

- The nodal crack points are moved, based on the crack growth rates at the two adjoining segments.

- The spline line is fitted through the nodal crack points.

- The fitted spline is divided into linear segments of equal length.

4. Numerical and Experimental Cases and Results

4.1 Stress Intensity Factors

In this section, SIFs obtained by using the weight function introduced in Section 3.2 are compared to solutions from existing literature. A comparison is made for both embedded and semi-elliptical surface cracks under uniform and non-uniform stress fields.

4.1.1 Embedded Elliptical Cracks

Embedded elliptical cracks in an infinite body are considered first and, as a result, the local bending introduced in Section 3.2 does not occur in this configuration. SIFs for cracks under the following stress fields were studied:

$$\sigma(x, y) = 1 \tag{4.1a}$$

$$\sigma(x, y) = \frac{x}{c} \tag{4.1b}$$

$$\sigma(x, y) = \frac{y}{a} \tag{4.1c}$$

$$\sigma(x, y) = \frac{x \cdot y}{a \cdot c} \tag{4.1d}$$

All stress fields are shown in Fig. 4.1. Reference SIFs are calculated using Irwin's analytic solution [72] and a solution proposed by Atroshchenko et al. [73]. The SIFs and comparison with the reference values are presented in Figs. 4.2-4.7. All SIF values along the crack front are in good agreement with the reference values.

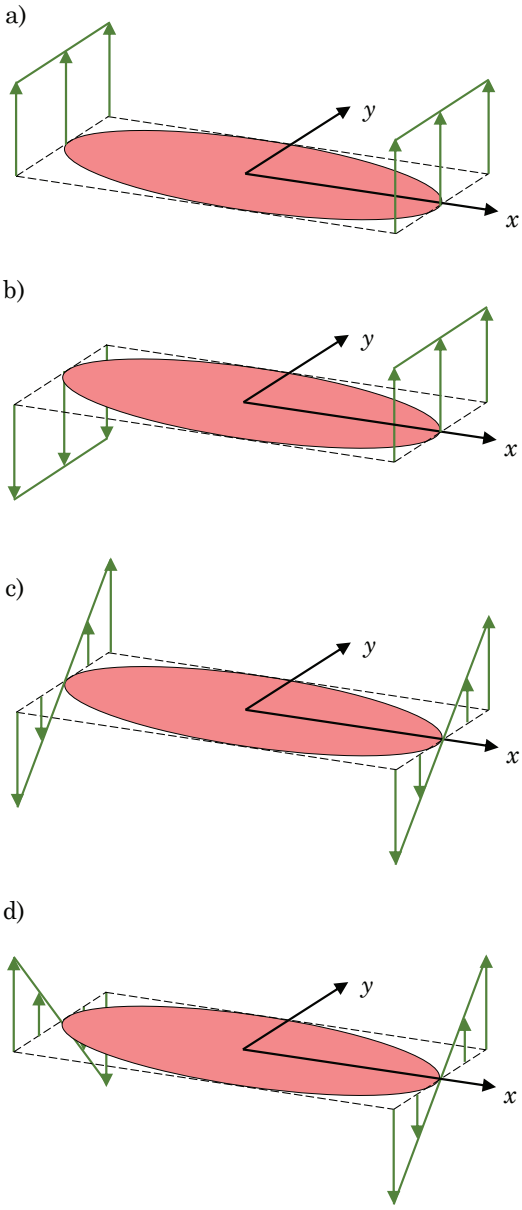

Figure 4.1. Embedded elliptical crack in an infinite body subjected to various stress fields, Eq. (4.1).

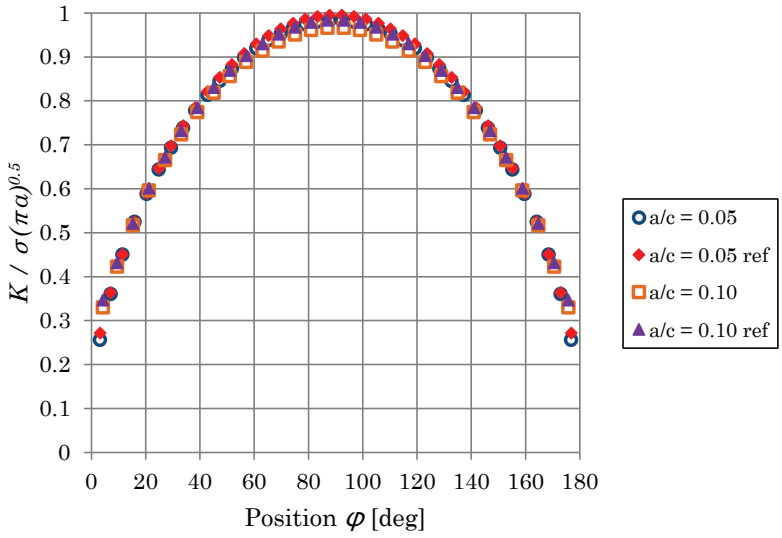

Figure 4.2. SIF distribution along the front line of an embedded crack in an infinite body, subjected to a uniform stress field. The crack aspect ratios, $a/c = 0.05$ and 0.1, were used. Reference solution: Irwin [72].

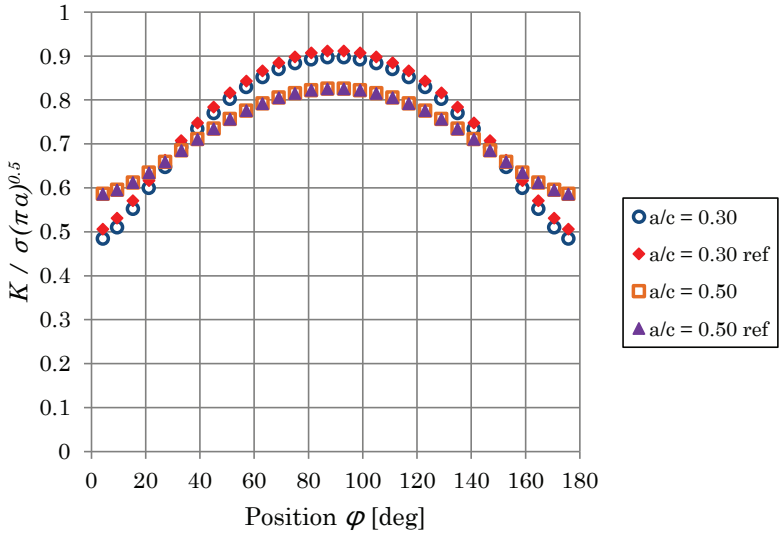

Figure 4.3. SIF distribution along the front line of an embedded crack in an infinite body, subjected to a uniform stress field. The crack aspect ratios, $a/c = 0.3$ and 0.5, were used. Reference solution: Irwin [72].

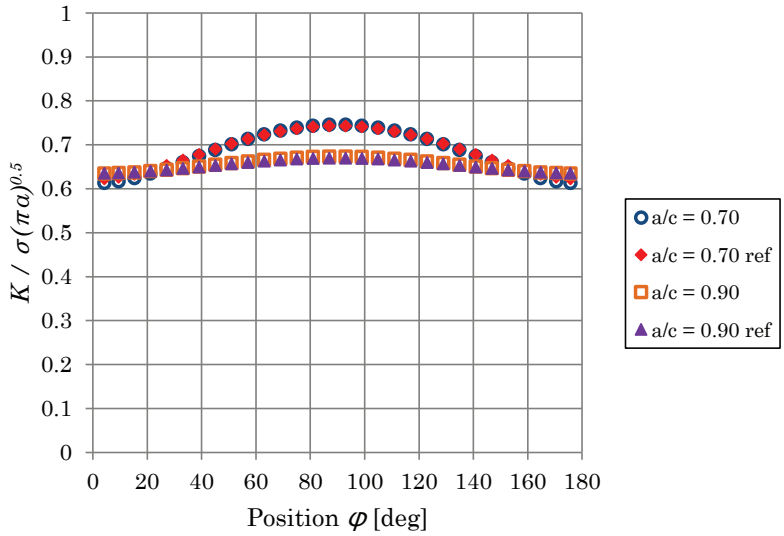

Figure 4.4. SIF distribution along the front line of an embedded crack in an infinite body, subjected to a uniform stress field. The crack aspect ratios, $a/c = 0.7$ and 0.9, were used. Reference solution: Irwin [72].

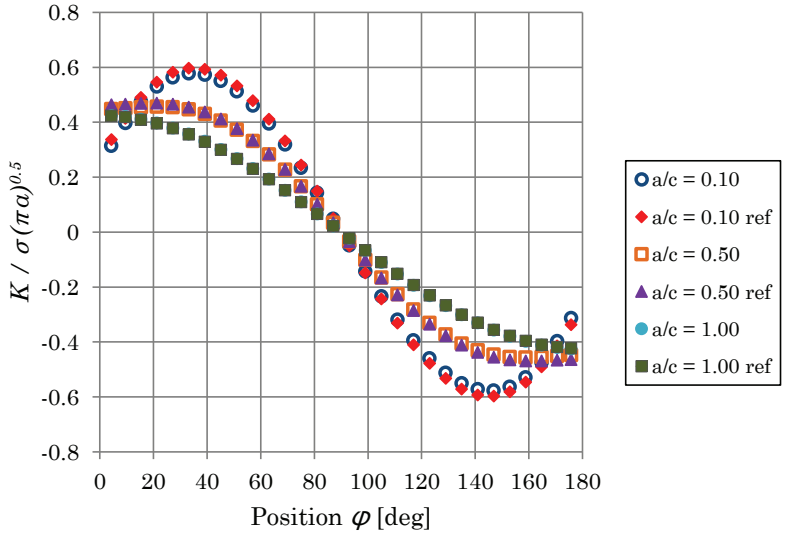

Figure 4.5. SIF distribution along the front line of an embedded crack in an infinite body, subjected to a non-uniform stress field, Eq. (4.1b). The crack aspect ratios, $a/c = 0.1$, 0.5 and 1.0, were used. Reference solution: Atroshchenko et al. [73].

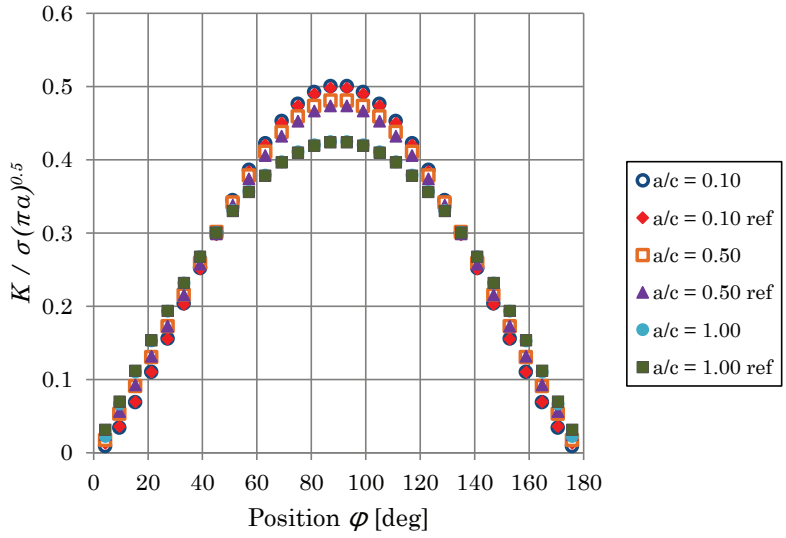

Figure 4.6. SIF distribution along the front line of an embedded crack in an infinite body, subjected to a non-uniform stress field, Eq. (4.1c). The crack aspect ratios, $a/c = 0.1$, 0.5 and 1.0, were used. Reference solution: Atroshchenko et al. [73].

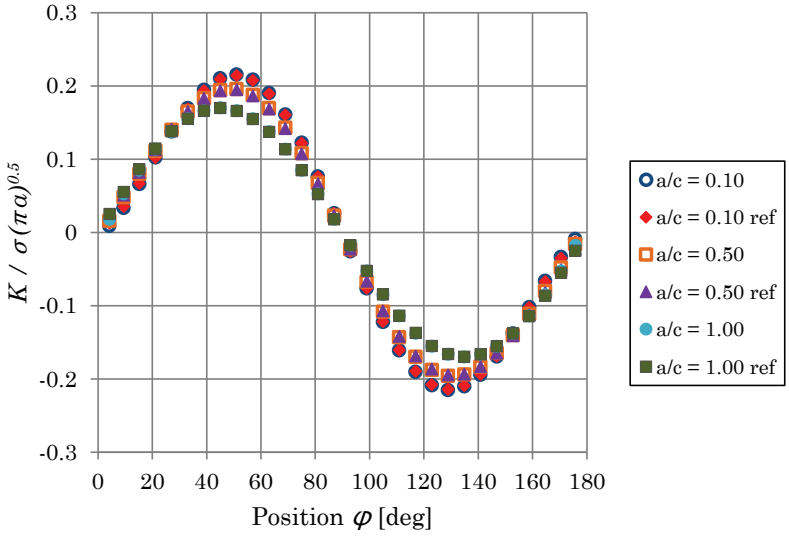

Figure 4.7. SIF distribution along the front line of an embedded crack in an infinite body, subjected to a non-uniform stress field, Eq. (4.1d). The crack aspect ratios, $a/c = 0.1$, 0.5 and 1.0, were used. Reference solution: Atroshchenko et al. [73].

4.1.2 Semi-Elliptical Surface Cracks

Semi-elliptical surface cracks in a finite thickness plate are considered and, as a consequence, the bending effect discussed in Section 3.2 had to be included. The SIF is calculated by using the proposed general point-load weight function, Eq. (3.11). The reference SIFs for such a semi-elliptical surface crack were calculated by using an empirical FEM-based equation presented by Newman and Raju [74] and a weight function proposed by Wang and Lambert [75]. The SIFs were calculated for different aspect ratios, a/c, and at different depths, a/t, and the following stress fields were applied:

$$\sigma(x,y) = 1 \tag{4.2a}$$

$$\sigma(x,y) = 1.0 - 2\frac{y}{t} \tag{4.2b}$$

The stress fields are shown in Fig. 4.8. The SIFs and comparison with the reference solutions are presented in Figs. 4.9-4.17. All SIF values along the crack front are in good agreement with the reference values when local bending is included. The SIFs presented in Figs. 4.14-4.17 were also calculated at the deepest point and the surface point using the proposed weight function Eq. (3.11) and original general point-load weight function without the local bending contribution, Eq. (2.6). The comparison shows that local bending contributes significantly when the crack is deep ($a/t > 0.2$) and wide ($a/c < 0.5$).

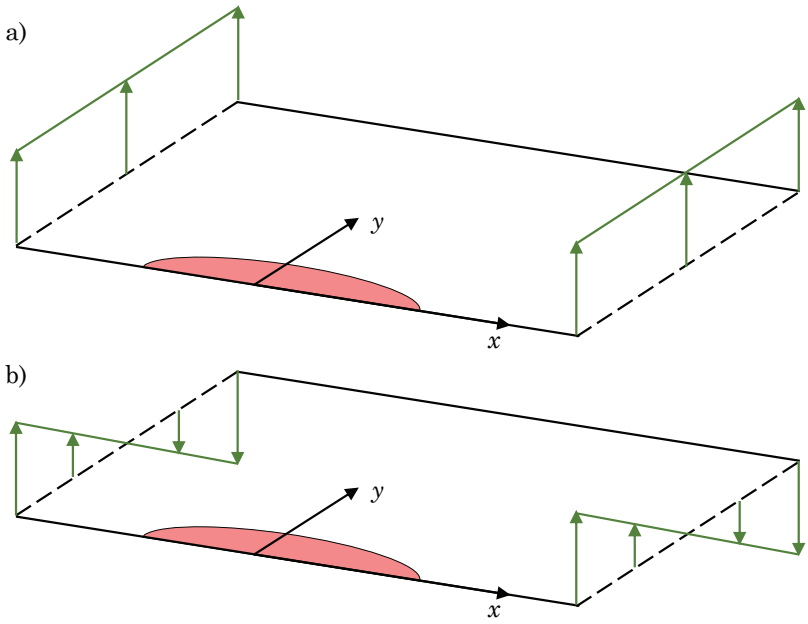

Figure 4.8. Semi-elliptical surface crack in a semi-finite body, subjected to various stress fields, Eq. (4.2).

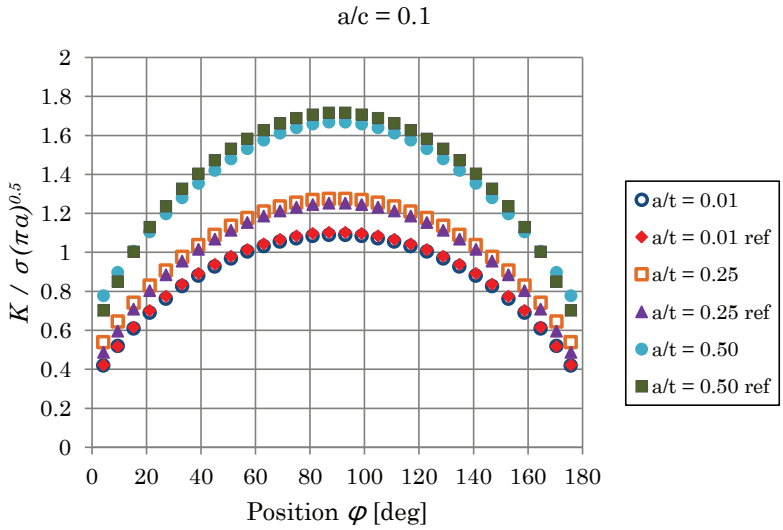

Figure 4.9. SIF distribution along the front line of a semi-elliptical crack in a finite thickness plate, subjected to a uniform stress field. The crack aspect ratio, $a/c = 0.1$, and the crack depths, $a/t = 0.01$, 0.25 and 0.5, were used. Reference solution: Newman and Raju [74].

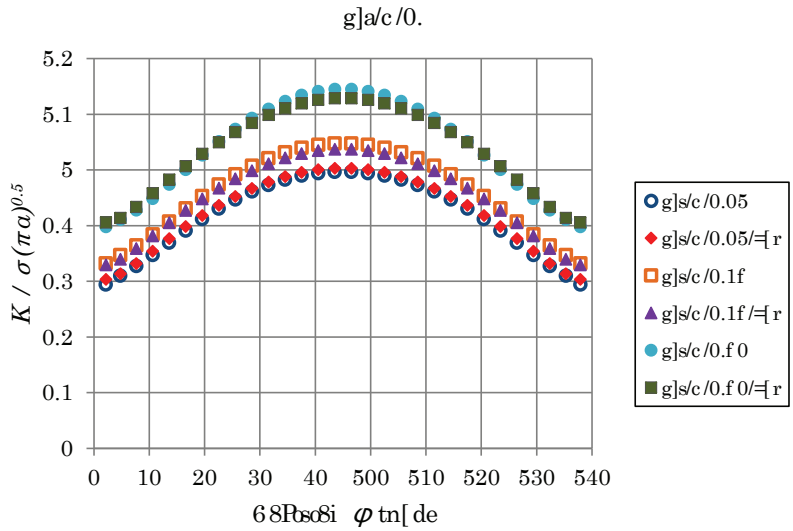

Figure 4.10. SIF distribution along the front line of a semi-elliptical crack in a finite thickness plate, subjected to a uniform stress field. The crack aspect ratio, $a/c = 0.3$, and the crack depths, $a/t = 0.01$, 0.25 and 0.5, were used. Reference solution: Newman and Raju [74].

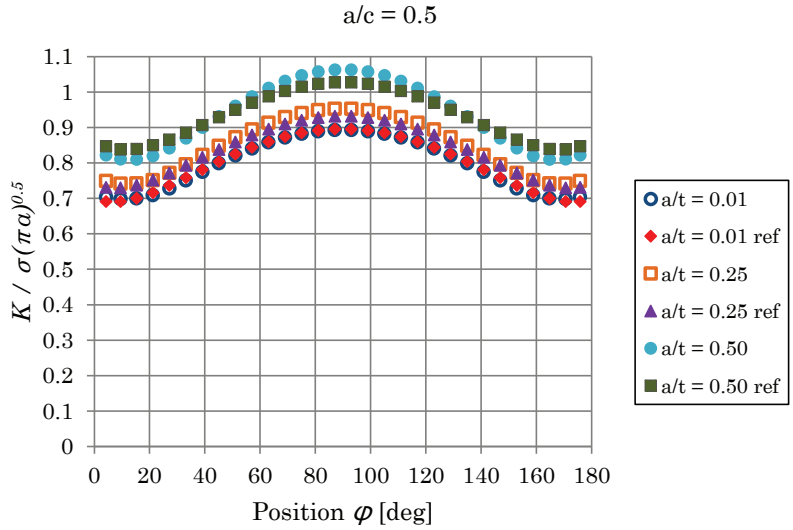

Figure 4.11. SIF distribution along the front line of a semi-elliptical crack in a finite thickness plate, subjected to a uniform stress field. The crack aspect ratio, $a/c = 0.5$, and the crack depths, $a/t = 0.01$, 0.25 and 0.5, were used. Reference solution: Newman and Raju [74].

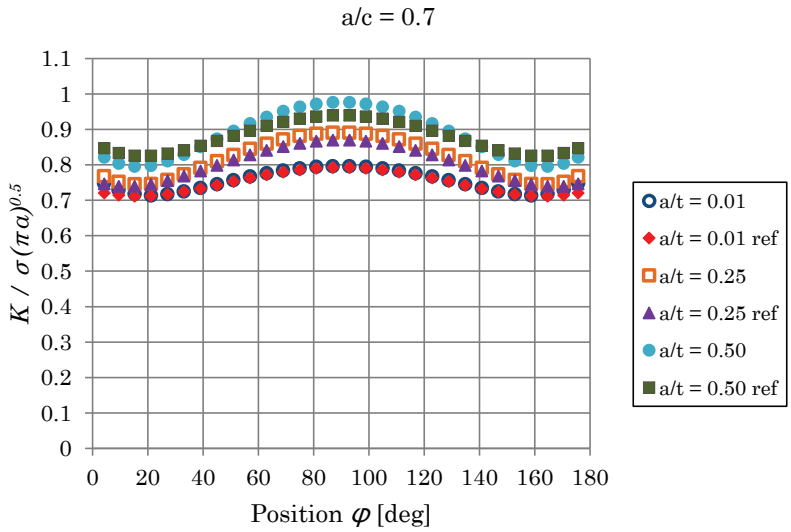

Figure 4.12. SIF distribution along the front line of a semi-elliptical crack in a finite thickness plate, subjected to a uniform stress field. The crack aspect ratio, $a/c = 0.7$, and the crack depths, $a/t = 0.01$, 0.25 and 0.5, were used. Reference solution: Newman and Raju [74].

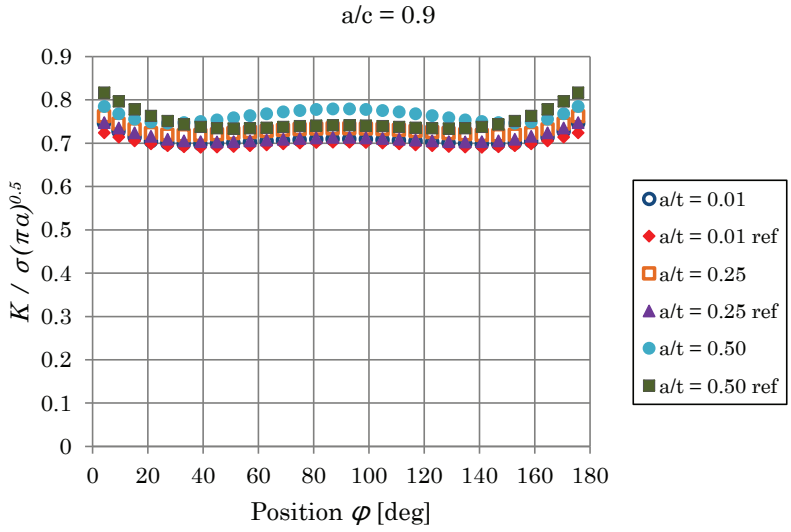

Figure 4.13. SIF distribution along the front line of a semi-elliptical crack in a finite thickness plate, subjected to a uniform stress field. The crack aspect ratio, $a/c = 0.9$, and the crack depths, $a/t = 0.01$, 0.25 and 0.5, were used. Reference solution: Newman and Raju [74].

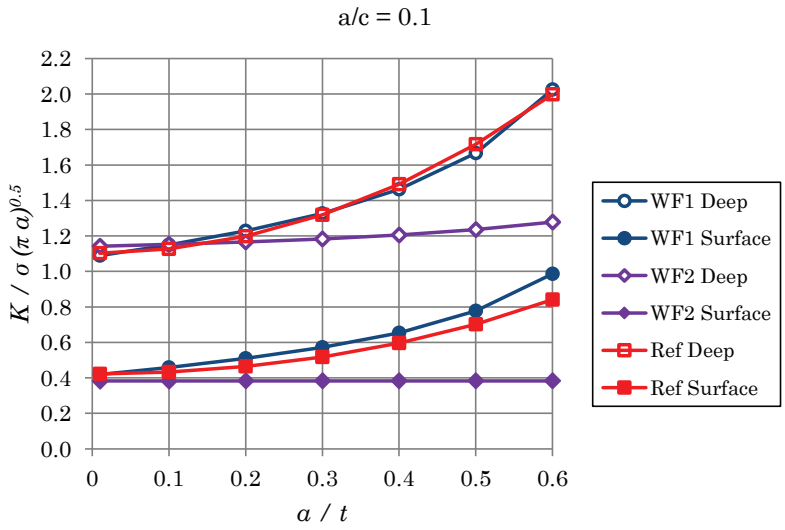

Figure 4.14. SIF at the deepest point and the surface point of a semi-elliptical crack in a finite thickness plate, subjected to a uniform stress field. The crack aspect ratio, $a/c = 0.1$, and the crack depths, $a/t = 0 - 0.6$, were used. WF1 is proposed weight function that includes the local bending. WF2 is the original weight function. Reference solution: Wang and Lambert [75].

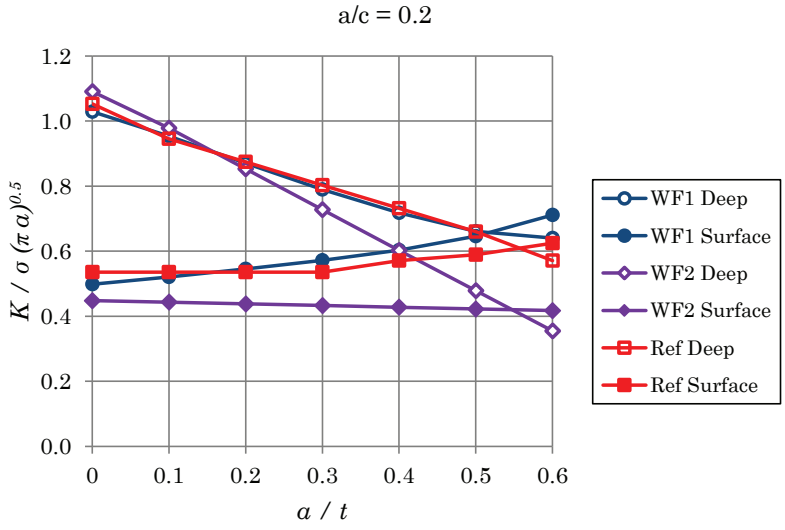

Figure 4.15. SIF at the deepest point and the surface point of a semi-elliptical crack in a finite thickness plate, subjected to a non-uniform stress field, Eq. (4.2b). The crack aspect ratio, $a/c = 0.2$, and the crack depths, $a/t = 0 - 0.6$, were used. WF1 is proposed weight function that includes the local bending. WF2 is the original weight function. Reference solution: Wang and Lambert [75].

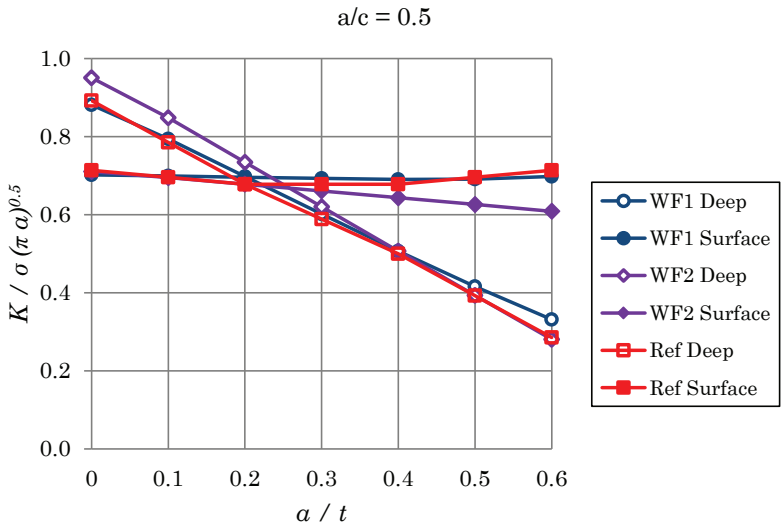

Figure 4.16. SIF at the deepest point and the surface point of a semi-elliptical crack in a finite thickness plate, subjected to a non-uniform stress field, Eq. (4.2b). The crack aspect ratio, $a/c = 0.5$, and the crack depths, $a/t = 0 - 0.6$, were used. WF1 is proposed weight function that includes the local bending. WF2 is the original weight function. Reference solution: Wang and Lambert [75].

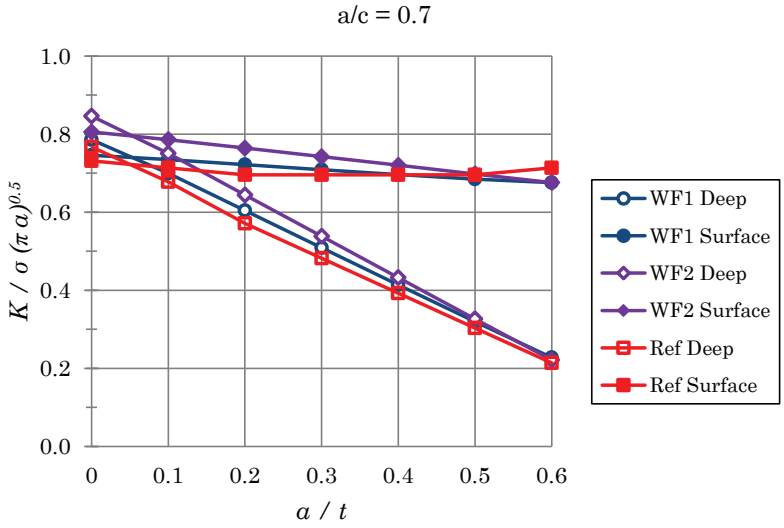

Figure 4.17. SIF at the deepest point and the surface point of a semi-elliptical crack in a finite thickness plate, subjected to a non-uniform stress field, Eq. (4.2b). The crack aspect ratio, $a/c = 0.7$, and the crack depths, $a/t = 0 - 0.6$, were used. WF1 is proposed weight function that includes the local bending. WF2 is the original weight function. Reference solution: Wang and Lambert [75].

4.2 Determination of the ρ^* Parameter

Accordingly, the material parameter, ρ^*, in Table 4.1 was determined for the method presented in Section 3.3.5. The method was verified by comparing the obtained ρ^* values with the referenced $\rho^*_{ref,1}$ [20] and $\rho^*_{ref,2}$ [76] values found in existing literature. The theoretical strength, σ_{thr}, was estimated by using Eqs. (3.22a) and (3.22b). The ρ^* parameter was calculated by substituting σ_{thr} into Eq. (3.21).

Table 4.1. Material properties and ρ^* estimations.

		Material		
		Al 2024	Al 7075-T6	St 4340
Elastic modulus (MPa)	E	$70,000$	$71,000$	$200,000$
Fracture toughness (MPa m$^{0.5}$)	K_{IC}	26	20	50
Theoretical strength (MPa)	σ_{thr}	$4,667$	$4,733$	$20,000$
Crack tip radius (m)	ρ^*	$9.9 \cdot 10^{-6}$	$5.7 \cdot 10^{-6}$	$2.0 \cdot 10^{-6}$
	$\rho^*_{ref,1}$ [20]	$1.5 \cdot 10^{-5}$	$4.0 \cdot 10^{-6}$	$1.1 \cdot 10^{-5}$
	$\rho^*_{ref,2}$ [76]	$8.0 \cdot 10^{-6}$	-	$2.0 \cdot 10^{-6}$

4.3 Planar Cracks Under Non-Uniform Stress Field and Subjected to Variable Amplitude Loading Histories

The behaviour of the planar cracks subjected to fluctuating non-uniform stress fields induced by variable amplitude cyclic loading is presented below. The motivation for this study was to verify that the method presented here can correctly simulate the retardation effect after applied overloads, in the case of uniform and non-uniform stress fields. The semi-elliptical crack was subjected to the uniform stress field and the embedded crack was considered when a non-uniform stress field was applied. The non-uniform stress field from Fig. 4.18 was used with the reference stress of $\sigma_{ref} = 200$ MPa. The stress field was chosen so that it is relevant for industrial practice but handbook solutions or one dimensional weight functions

are not applicable to solve problem.

The initial cracks in both cases were $a_i = 0.5$ mm and $c_i = 2.5$ mm and material properties from Table 4.2 were used. The simulations were run with four different loading spectra:

Spectrum #1
Constant amplitude stress with $\sigma = 200$ MPa and $R = 0$. The spectrum is shown in Fig. 4.19

Spectrum #2
Constant amplitude similar to Spectrum #1, but including a single periodic overload, $\sigma_{ol} = 375$ MPa, which first occurs at cycle $20,000$. The overload was applied every $100,000$ cycles in the case of the semi-elliptical crack and, correspondingly, every $50,000$ cycles in the case of the embedded crack. The spectrum is presented in Fig. 4.20.

Spectrum #3
Similar to Spectrum #2, except that the overload was followed by an immediate underload (throughout this document the term underload is used to describe a compressive overload cycle), $\sigma_{ul} = -55$ MPa. The spectrum appears as Fig. 4.21.

Spectrum #4
Random stress spectrum. For each cycle, σ_{max} and $\Delta\sigma$ were randomly sampled using the normal probability distribution. The mean of the normal distribution was 200 MPa and standard deviation was 50 MPa. The complete spectrum is presented in Fig. 4.22 and the first 100 reversals in Fig. 4.23.

Simulations of the surface crack growth were run until the crack depth of $a = 10$ mm was reached. Correspondingly, the growth of the embedded crack was simulated until $a = 20$ mm was reached. The fatigue lives are provided in Table 4.3 and a and crack area against N are shown in Figs 4.24 and 4.25. The evolution of the crack front under Spectrum #2 is presented in Figs. 4.26 and 4.27. The results are in good agreement with general knowledge and assumptions based on previous studies related to the behaviour of fatigue cracks under variable amplitude loading [77].

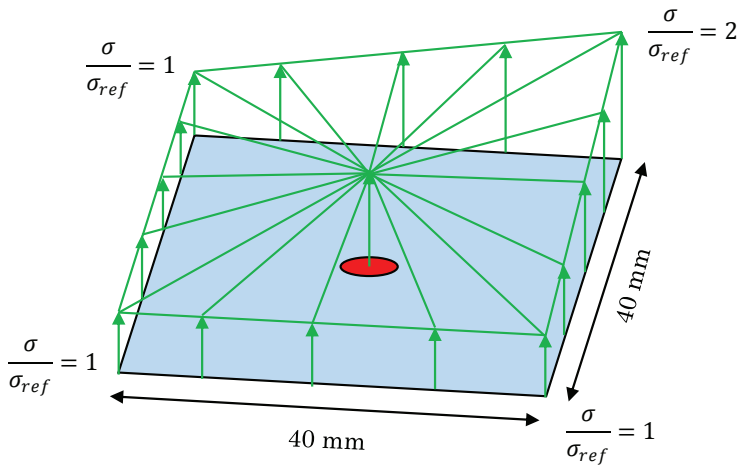

Figure 4.18. Non-uniform stress field applied to an embedded crack.

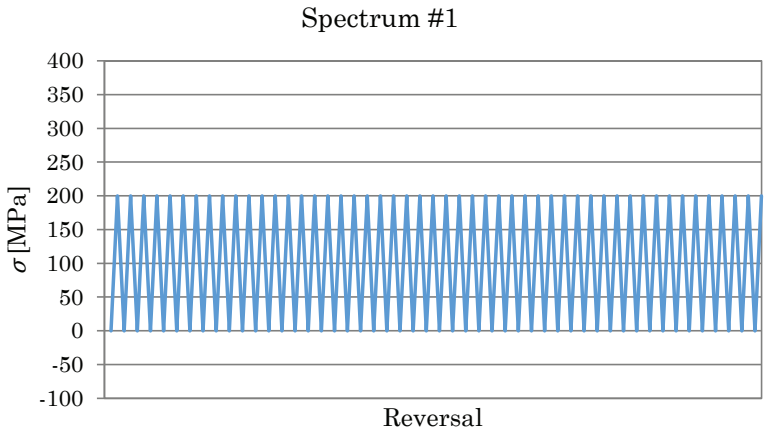

Figure 4.19. Constant amplitude loading spectrum.

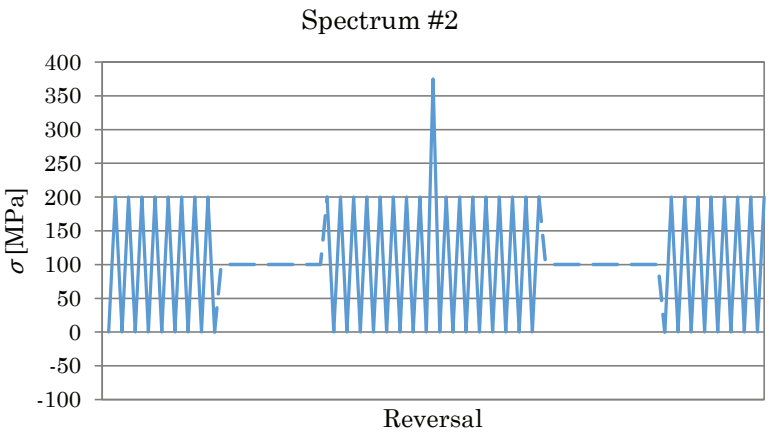

Figure 4.20. Constant amplitude loading spectrum with a single overload.

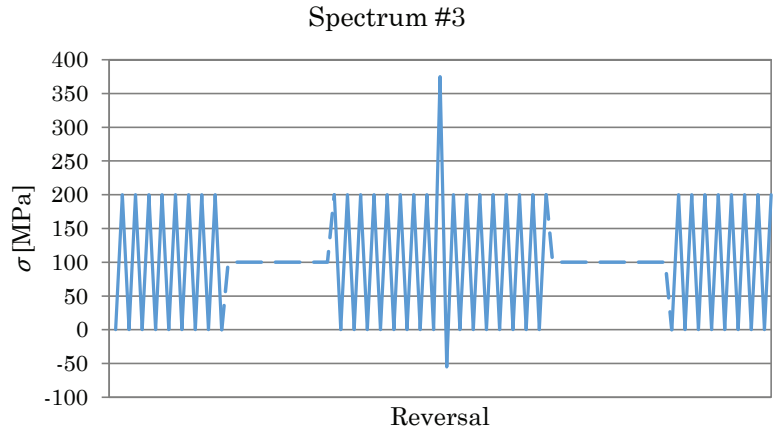

Figure 4.21. Constant amplitude loading spectrum with a single overload, followed by an immediate underload (compressive overload).

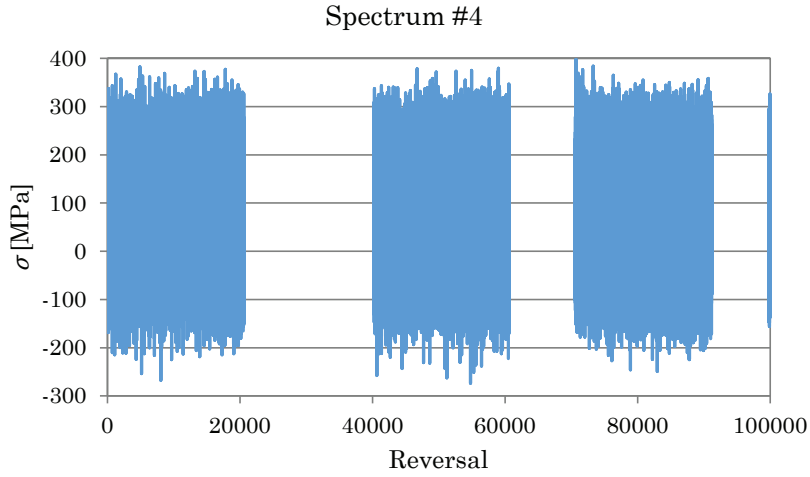

Figure 4.22. Randomly-generated loading spectrum.

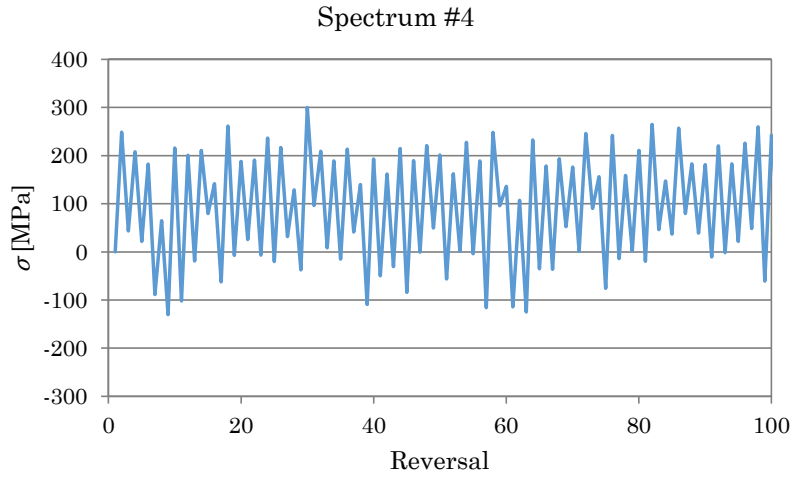

Figure 4.23. Randomly-generated loading spectrum, reversals 0 - 100.

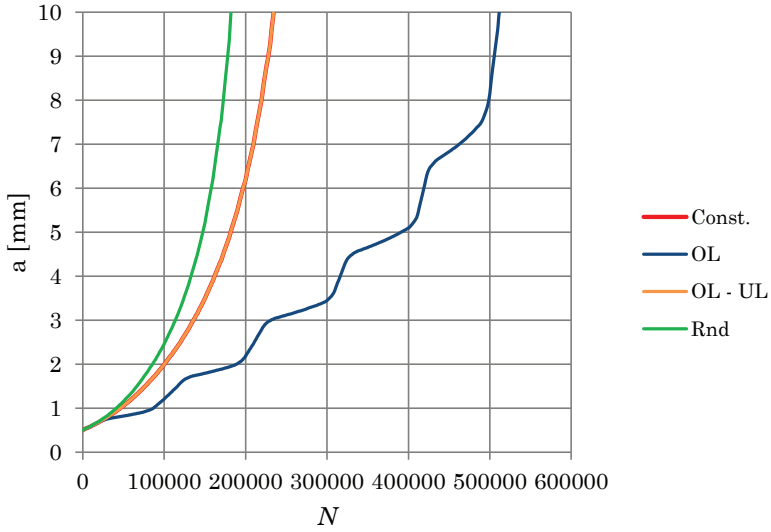

Figure 4.24. Surface crack: development of a

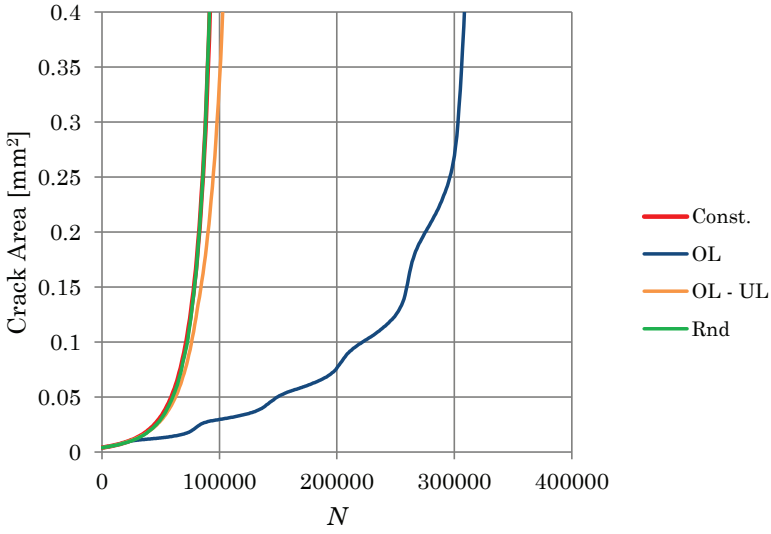

Figure 4.25. Embedded crack: development of crack area.

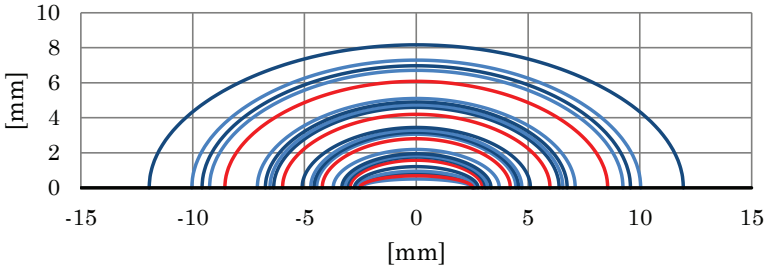

Figure 4.26. The surface crack: Evolution of the crack front. Contour lines are drawn every $20,000$ cycles. Red lines represent the crack front position when the overload was applied.

Table 4.2. Material parameters (mean values) for A22-H steel.

Ultimate strength, σ_u	545	MPa
Yield strength, σ_y	475	MPa
Elastic modulus, E	206423	MPa
Fracture Toughness, K_{IC}	50	Mpa $m^{0.5}$
Cyclic strength coefficient, $K^{'}$	1070.1	MPa
Cyclic hardening exponent, $n^{'}$	0.187	
Crack tip radius, ρ^{*}	$5.5x10^{-6}$	m
FCG constant, C	$3.0x10^{-11}$	(m , MPa $m^{0.5}$)
FCG exponent, m	3.02	

Table 4.3. Estimated fatigue lives.

Spectrum	N_f, surface	N_f, embedded
#1	234,500	97,963
#2	511,483	315,679
#3	234,536	111,687
#4	182,054	99,898

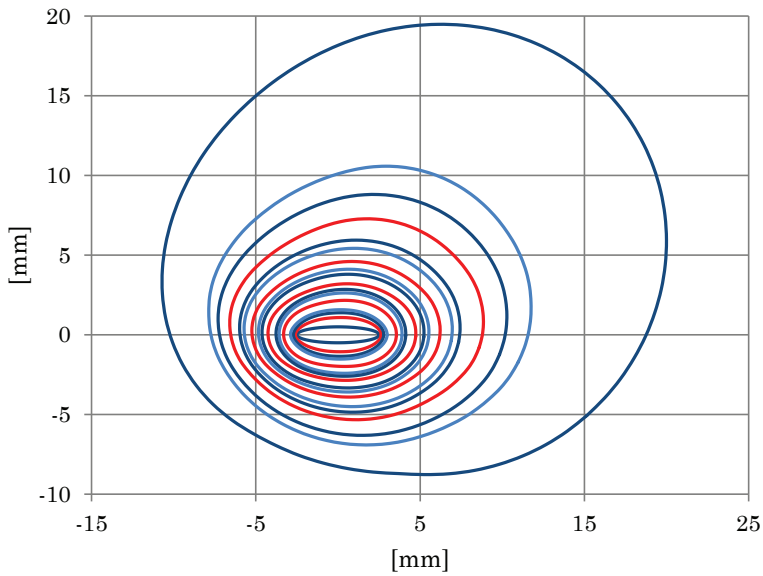

Figure 4.27. The embedded crack: Evolution of the crack front. Contour lines are drawn every $20,000$ cycles. Red lines represent the crack front position when the overload was applied.

4.4 Effect of the Initial Crack Geometry

In practice, cracks of arbitrary geometry are approximated by an elliptical crack. However, the actual aspect ratio, a/c, dimension and location of the initial crack are seldom known and results depend on assumed values. This numerical study concentrates on the effect of the initial aspect ratio, a/c, and the influence of size and location are studied in Section 4.5. The purpose was to identify the most critical, initial aspect ratio that leads to the shortest fatigue life. This aspect ratio can be used to obtain the most conservative fatigue life estimation, if the actual initial crack geometry is unknown.

In order to identify the most critical aspect ratio, numerous crack growth simulations were run with different initial a/c values, while the initial crack area was kept constant. The simulations were run until the final crack area was 100 times greater than the initial one. Both embedded cracks in an infinite body and semi-elliptical cracks in a semi-infinite body were considered. A uniform stress field was applied in both cases.

This study revealed that the fatigue crack growth exponent, m, in Eq. (3.15), significantly influences the final fatigue lives. Fatigue lives with different initial aspect ratios and various fatigue crack growth exponent values are presented in Figs. 4.28 and 4.29. The aspect ratio, a/c, that yields the minimum fatigue life, N_{min}, depends on the fatigue crack growth exponent, m. The fatigue life, N, approaches infinity in all cases when the initial ratio, a/c, approaches zero (infinitely wide crack). This happens as a result of the assumed constant initial crack area, thus, $a \to 0$ when $c \to \infty$. The fatigue lives of embedded cracks in Fig. 4.28 reach a local maximum value when $a/c = 1.0$. The local maximum of the fatigue lives of surface cracks in Fig. 4.29 occurs with different a/c values, depending on the exponent, m.

The fatigue lives in Figs. 4.28 and 4.29 are presented in relation to the shortest life, N_{min}, of each curve. Therefore, the fatigue life values between different curves cannot be compared.

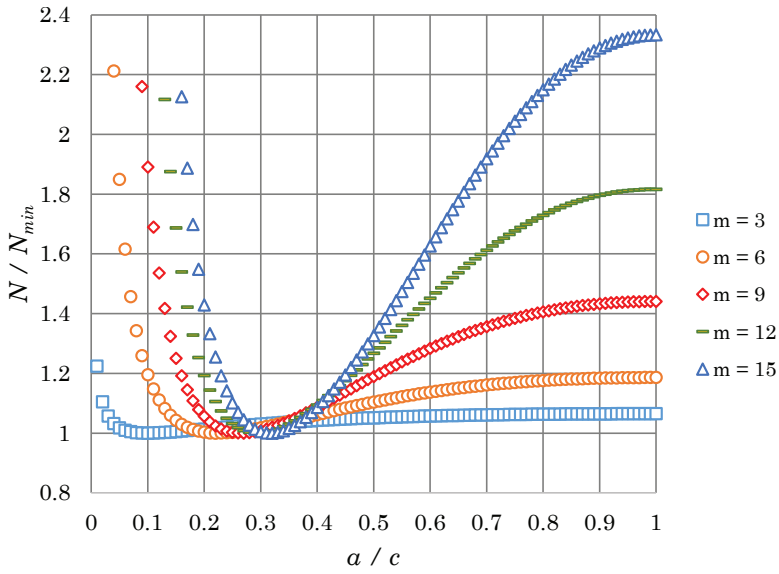

Figure 4.28. Fatigue life of embedded cracks with various initial aspect ratios, a/c, and the FCG exponent, m.

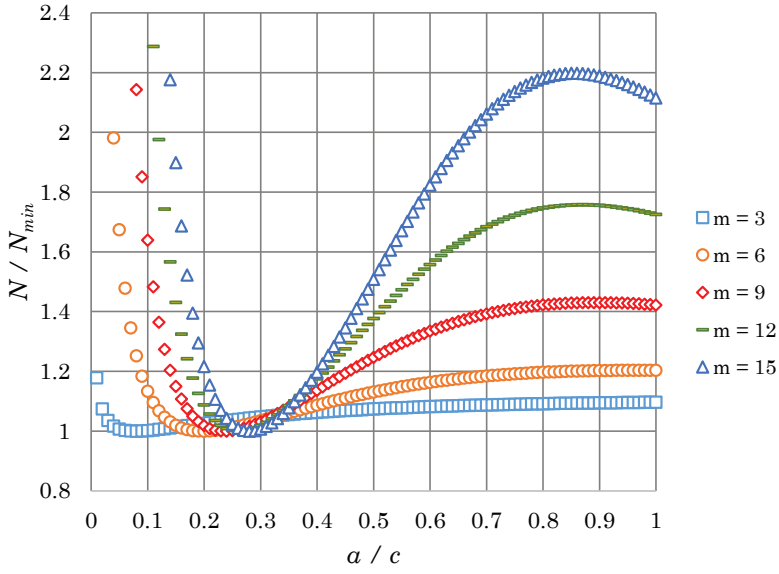

Figure 4.29. Fatigue life of semi-elliptical surface cracks with various initial aspect ratios, a/c, and the FCG exponent, m.

The most critical aspect ratio, a/c, is shown in Figs. 4.30. and 4.31 as a function of m. The following equations are fitted to data and can be used to determine the ratio, a/c, that gives the shortest fatigue life:

Embedded:

$$a/c = 8.7802 \cdot \exp\left(3.8367 \cdot m^{-1.1207}\right) - 6.3904 \cdot \exp\left(4.0966 \cdot m^{-1.0022}\right) - 1.8578 \quad (4.3)$$

Surface:

$$a/c = 9.0213 \cdot \exp\left(3.8456 \cdot m^{-1.0676}\right) - 7.1082 \cdot \exp\left(4.0391 \cdot m^{-0.9803}\right) - 1.4446 \quad (4.4)$$

4.5 Fatigue Crack Growth of the Small Inclusion in a Valve Spring Wire

The method was also used to analyse the fatigue failure of a valve spring in Fig. 4.32. The spring was developed for a very long fatigue life and failure occurred because of a sub-surface fatigue crack that initiated from a sub-surface defect. The fracture surface in Fig. 4.33 was inspected and the initial flaw size was measured as 20 μm x 30 μm. The initial flaw was located at a depth of 175 μm below the surface and the crack became unstable after breaking through the free surface. Based on service hours, the spring failed approximately after 78 million cycles. The diameter of the spring wire was 4 mm.

The constant amplitude load fluctuated between 298 N to 791 N, i.e., the load ratio was $R = 0.38$. The applied load induced internal torsion and direct shear. Thus, the stress distribution over the cross-section of the spring wire was non-uniform. The principal normal stresses were found in the plane that was oriented at a 45° angle with respect to the wire's longitudinal axis, as shown in Fig. 4.34. The distance between the crack and the free surface on the plane was 250 μm.

Spring wires are usually post-treated in order to induce compressive residual stresses at the surface. Unfortunately, the residual stresses were not measured and consequently, the residual stress field could only be approximated, based on measurements found from existing literature. The fatigue properties of the actual steel were not available, hence the properties of similar steel materials were used. Material properties are presented in Table 4.4.

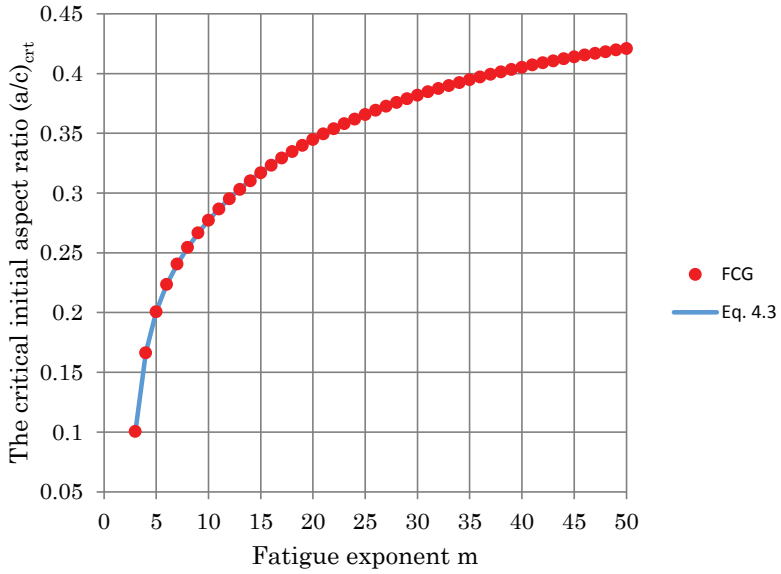

Figure 4.30. The most critical aspect ratio a/c of a embedded crack as a function the fatigue crack growth exponent m.

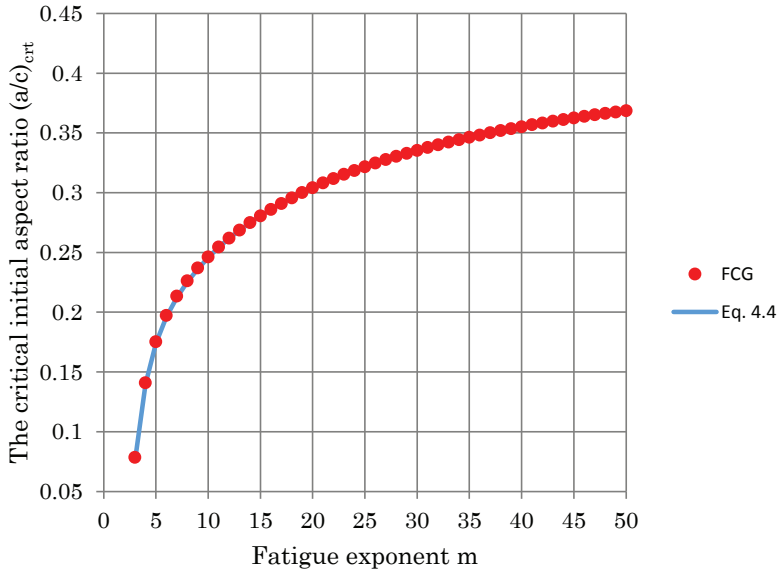

Figure 4.31. The most critical aspect ratio, a/c, of a semi-elliptical surface crack, as a function of the fatigue crack growth exponent, m.

The initial crack was modelled as an ellipse and fatigue crack growth was computed until the crack front reached the free surface, as presented in Fig. 4.35. The effects of the residual stresses and the initial conditions were studied by running several simulations with different configurations, as described below.

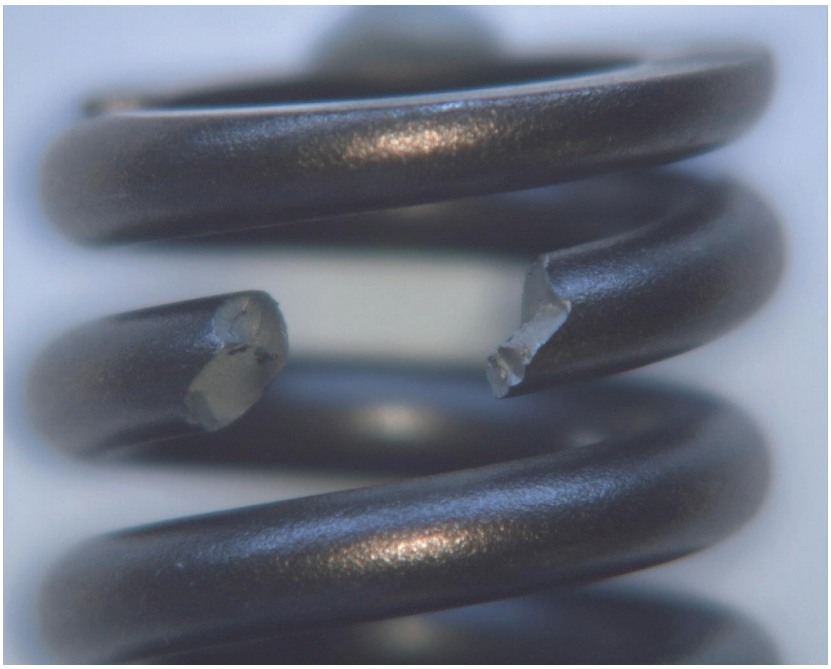

Figure 4.32. Valve spring wire after fatigue failure.

Table 4.4. Material parameters (mean values) for high strength spring steel.

Ultimate strength, σ_u	2010	MPa
Yield strength, σ_y	1280	MPa
Elastic modulus, E	206000	MPa
Cyclic strength coefficient, $K^{'}$	3488	MPa
Cyclic hardening exponent, $n^{'}$	0.161	
Crack tip radius, ρ^{*}	2.28x10^{-6}	m
FCG constant, C_1	2.31x10^{-21}	(m , MPa m$^{0.5}$)
FCG exponent, m_1	19.13	
FCG constant, C_2	9.13x10^{-12}	(m , MPa m$^{0.5}$)
FCG exponent, m_2	3.06	
Driving force exponent, p	0.14	

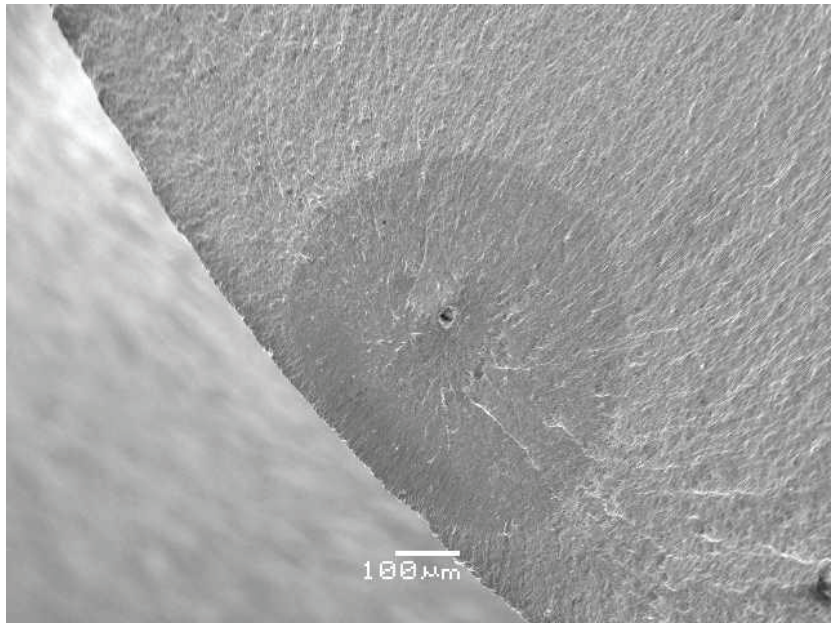

Figure 4.33. Fracture surface of a valve spring wire.

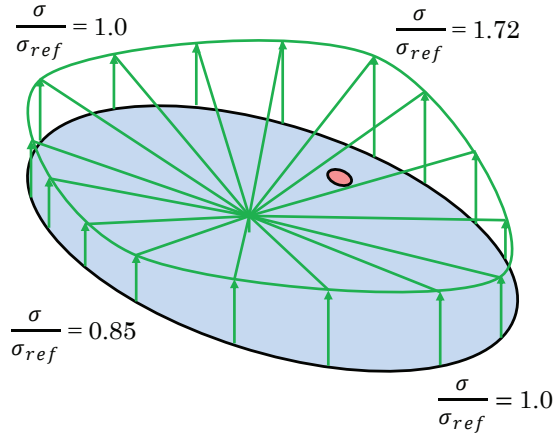

Figure 4.34. Stress field over the cross-section of the spring wire, $\sigma_{ref} = 582$ MPa (max).

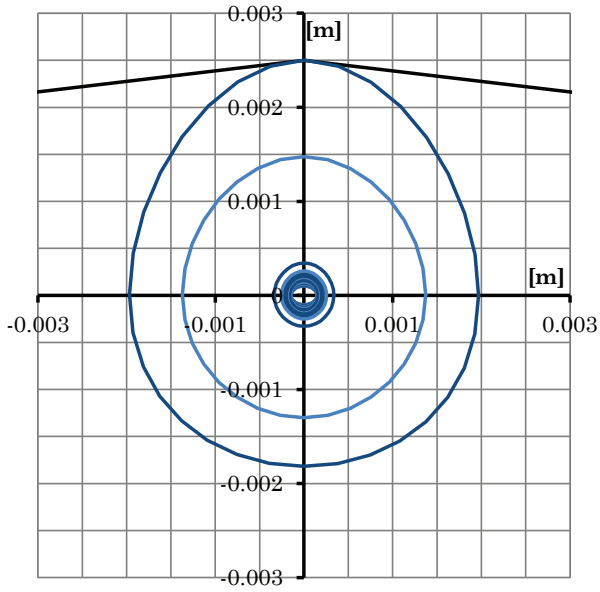

Figure 4.35. Simulated fatigue crack growth by using the measured input values.

4.5.1 The global Residual Stress Effect

The residual stress profile was simplified by using four parameters. The maximum compressive residual stress, σ_c, occurs at the free surface and continues until the depth of d_c. After that point, the residual stress starts to shift linearly from compression to tension. The maximum tensile residual stress, σ_t , occurs at the depth of d_t. The maximum tensile residual stress remains constant between d_t and the centre of the cross-section. The residual stress profile was assumed to be symmetric in relation to the centre line. The parameters are presented in Fig. 4.36

The actual profile was not measured and, therefore, the parameters were approximated. Based on the observations of Wang et al. [78], the assumption was made that $d_t = 3.6\, d_c$. Due to this assumption and the force equilibrium, $A_{c1} + A_{c2} = A_{t1} + A_{t1}$, in Fig. 4.36, only two parameters are needed to fully define the residual stress profile.

The maximum compressive residual stress, σ_c, and the depth of the maximum compressive residual stress, d_c, were chosen to define the stress profile. The effect of the residual stress profile was studied by varying these parameters. The parameter, σ_c, was varied from 0 to 900 MPa and the parameter, d_c, from 50 to 300 μm. The results are presented in Fig. 4.37.

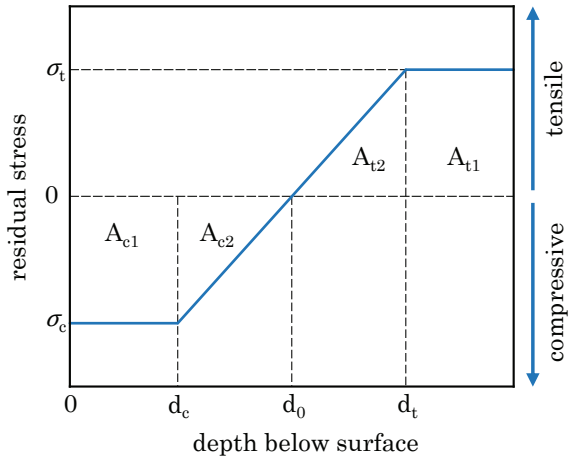

Figure 4.36. Residual stress profile.

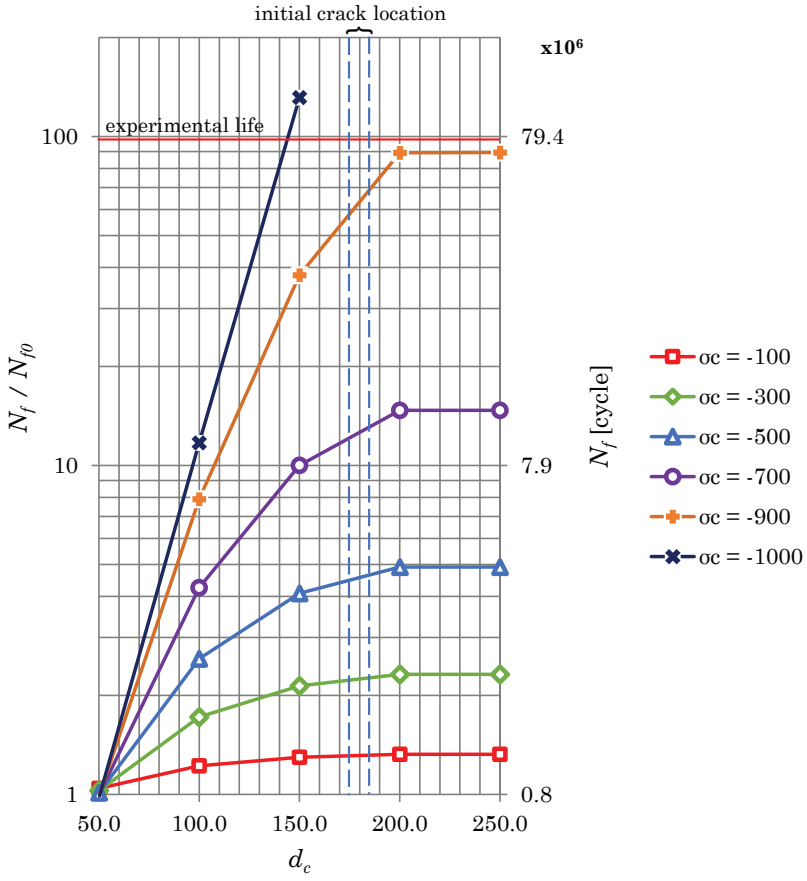

Figure 4.37. Effect of residual stresses. N_{f0} refers to fatigue life without any residual stresses.

4.5.2 Effect of the Initial Crack Geometry

In practice, an arbitrary initial flaw is usually approximated by an elliptical crack. However, the actual aspect ratio, a/c, the size and location of the initial crack are seldom known precisely and depend on the selected input data.

The importance of the input data effect was studied by varying those parameters. The parameters were varied one by one, while keeping other values as constants that correspond to the measured values. These computations were run without accounting for the residual stresses or the small crack effect.

The fatigue life in Fig. 4.38 was computed by varying the initial aspect ratio, a/c, from 0.2 (narrow) to 1.0 (circular). Similar behaviour was observed as previously in Section 4.4. The minimum fatigue life was obtained with $a/c = 0.38$. The fatigue life in Fig. 4.39 shows the effect of the initial dimension. The initial dimensions of the elliptical crack, a and c, were varied within the range of $\pm 15\%$ of the measured values. The distance between the surface and the crack was varied within the range of $0 - 350\mu$m, as shown in Fig. 4.40.

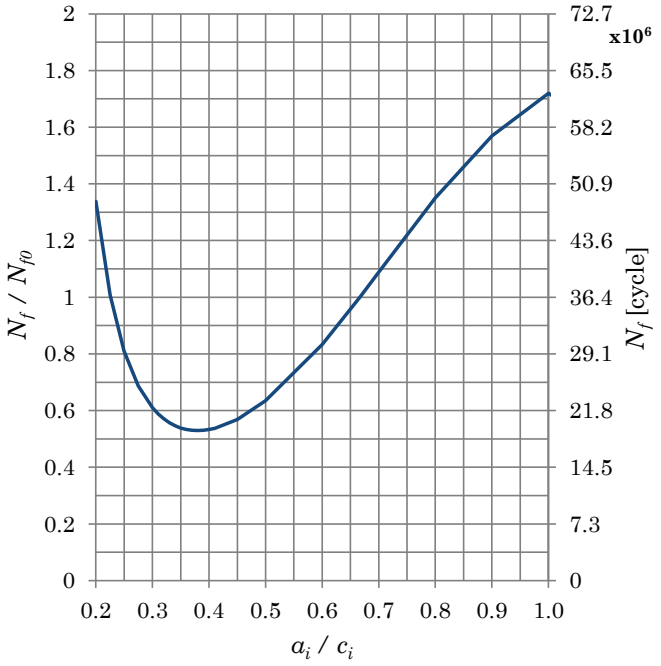

Figure 4.38. Estimated fatigue lives for cracks with different initial aspect ratios, a_i/c_i. The fatigue life, N_{f0}, is the estimated fatigue life which corresponds to the actual measured aspect ratio, $a_i/c_i = 0.67$.

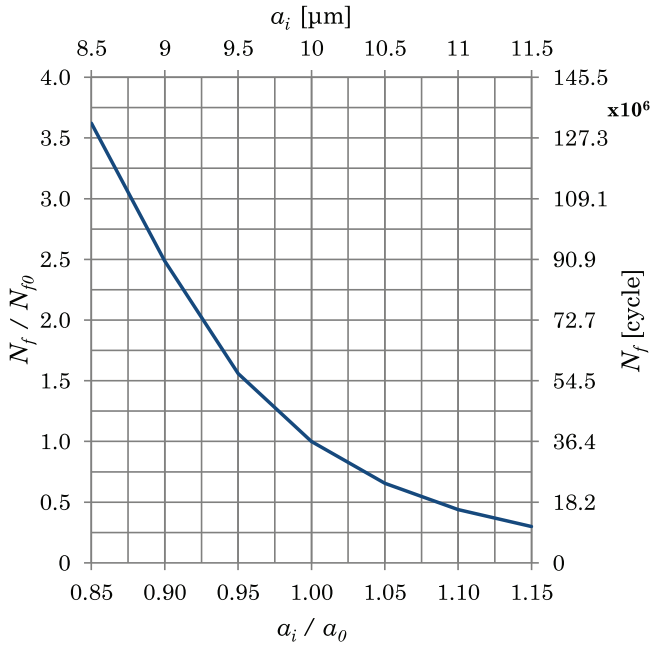

Figure 4.39. Estimated fatigue lives for cracks with different initial sizes, a_i. The fatigue life, N_{f0}, is the estimated fatigue life which corresponds to the actual measured initial size, a_0.

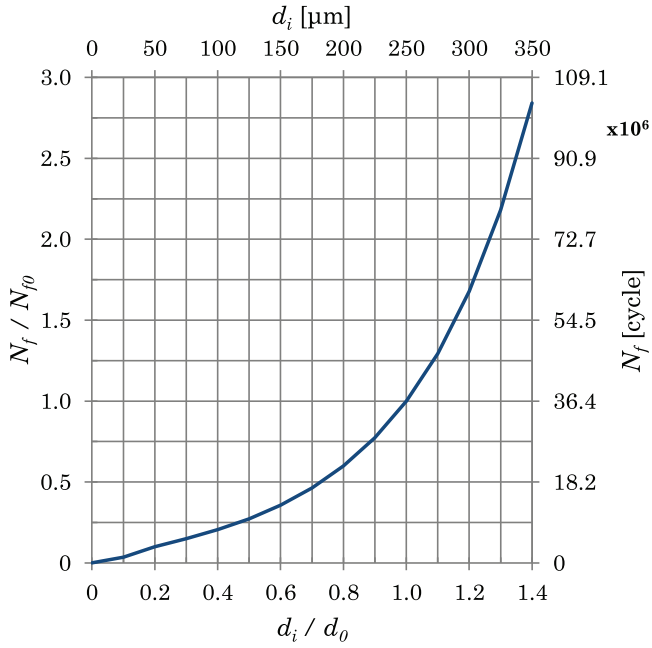

Figure 4.40. Estimated fatigue lives for cracks with different distances from the surface, d_i. The fatigue life, N_{f0}, is the estimated fatigue life which corresponds to the actual measured depth, $d0 = 250\ \mu m$.

4.6 Fatigue Life Analysis of a Tubular Welded Structure

The numerical fatigue crack growth simulation programme has been validated, based on comparison with published experimental results for a welded, rectangular, hollow-section joint, subjected to bending and torsion [79]. During the experiment, only the crack length on the surface was measured.

4.6.1 Experimental Set-up

The two rectangular tubes in Fig. 4.41 were welded together by using the Flux Cored Arc Welding (FCAW) method. The dimensions of the welded profiles were, respectively, 101.6 x 101.6 x 600.075 mm and 50.8 x 152.4 x 363.5502 mm, and the wall thicknesses were 7.9 mm. The welded profiles were fabricated from A22-H steel (ASTM A500 Cold-Formed Steel for Structural Tubing). The weld dimensions in Fig. 4.42 were:

$t = 7.9$ mm	$h = 7.9$ mm	$r = 0.79$ mm
$t_p = 7.9$ mm	$h_p = 7.9$ mm	$\theta = 45^\circ$

The specimen was subjected to torsional and bending load fluctuations within the range of ± 17.8 kN, applied at the free end of the large square profile. The bottom base plate was secured by six screws.

4.6.2 Fatigue life Analysis

Using shell elements, the FEM was employed to determine the most critical location where cracks would be expected to initiate. The most critical point in Figs. 4.43 and 4.44 was identified at the weld toe, located at the end of the tube. The FEM calculations were performed by Chattopadhyay et al. [79]. In order to estimate the fatigue life at this location, the through-thickness stress distribution in Fig. 4.45 was determined. The residual stress distribution in Fig. 4.46 was approximated, based on limited experimental data [79].

Two different techniques were used, one with and the other without residual stresses. Thus, four different fatigue crack growth simulations were performed using different initial parameters. The first two simulations followed the calculations by [79], by assuming a similar crack initiation life, N_i, and an initial crack size of a_i and a_i/c_i. However, the crack growth model presented in this work was used to estimate crack propaga-

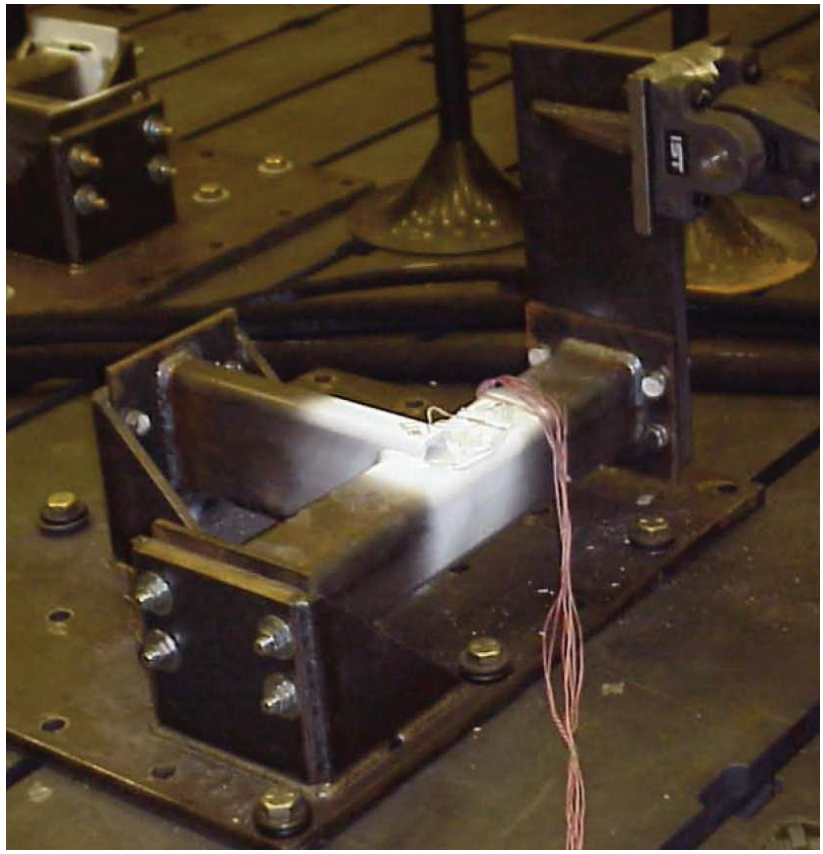

Figure 4.41. Experiment set-up for fatigue life analysis of tubular welded structure.

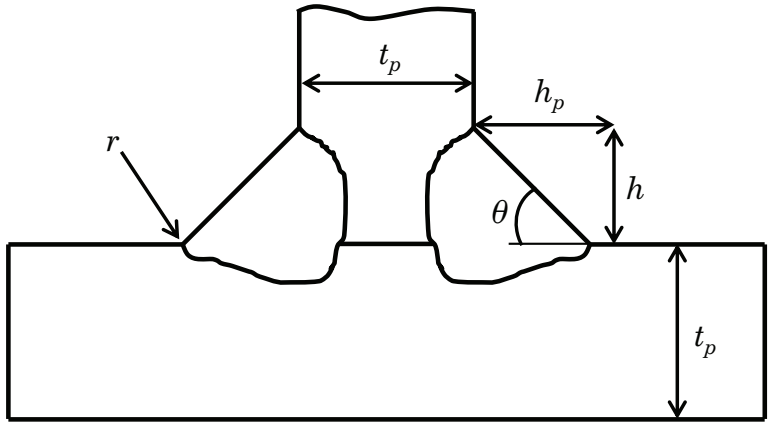

Figure 4.42. Notation for the weld dimensions.

tion life. The remaining two simulations were started from smaller initial cracks, without separate crack initiation calculations. The purpose was to estimate total fatigue life using only the crack propagation. In these two simulations, the initial crack size and geometry were assumed, based on the research of Nykänen et al. [80]. The parameters of these simulations are presented in Table 4.5.

Table 4.5. Parameters for different simulations.

Simulation #	a_i (mm)	a_i/c_i	N_i	Residual stresses
1	0.5	0.286	10 602	Yes
2	0.5	0.286	25 039	No
3	0.2	0.4	0	Yes
4	0.2	0.4	0	No

The material properties given in Table 4.2 were used. Unfortunately, due to the unavailability of the constant amplitude fatigue curves, i.e., $\mathrm{d}a/\mathrm{d}N$ vs. ΔK curves, the ρ^* parameter was estimated by using Eq. (3.21).

The simulated fatigue crack growth on the free surface was compared with the experimental data shown in Fig. 4.47. The simulated fatigue crack growth in the depth direction is presented in Fig. 4.48. The crack depth dimension was not measured during the experiments. The crack front developed in such a way that the aspect ratio, a/c, in Fig. 4.49 did not remain constant. The varying aspect ratio, the non-uniform stress field and the effect of free surfaces influenced the SIFs, as presented in Fig. 4.50. The simulated crack shape evolution is illustrated in Fig. 4.51.

4.7 Fatigue Life Analysis of a T-Welded Joint

The set of experimental data for the T-welded joint was made available courtesy of John Deere[81].

4.7.1 Experimental Set-up

The attachment in Fig. 4.52 was welded to the base plate by using the Flux Cored Arc Welding (FCAW) method. The dimensions of the attachment were 50 x 100 x 4 mm and the base plate dimensions were 500 x 500 x 4 mm. The base plate and the attachment were composed of SAE 1008 steel. The weld dimensions in Fig. 4.42 were:

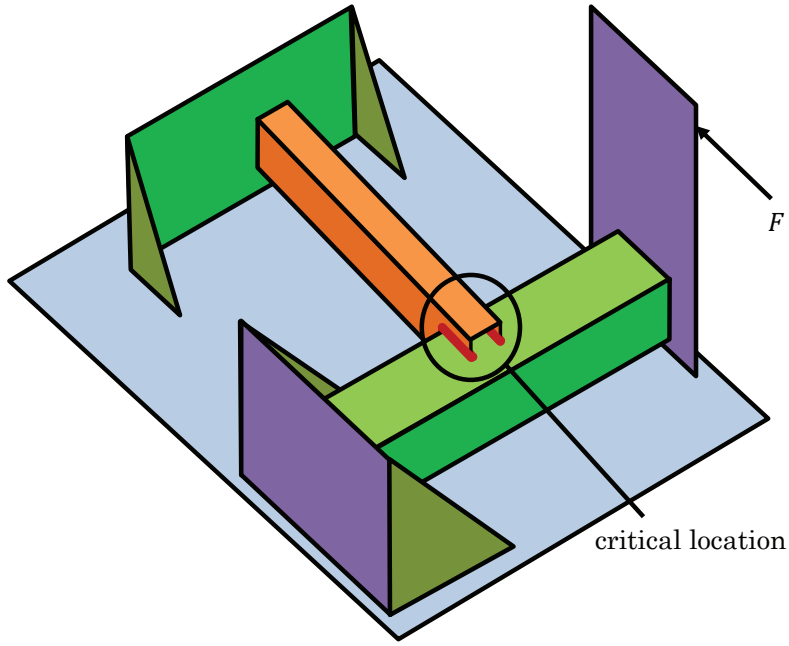

Figure 4.43. The most critical point based on FEM analysis

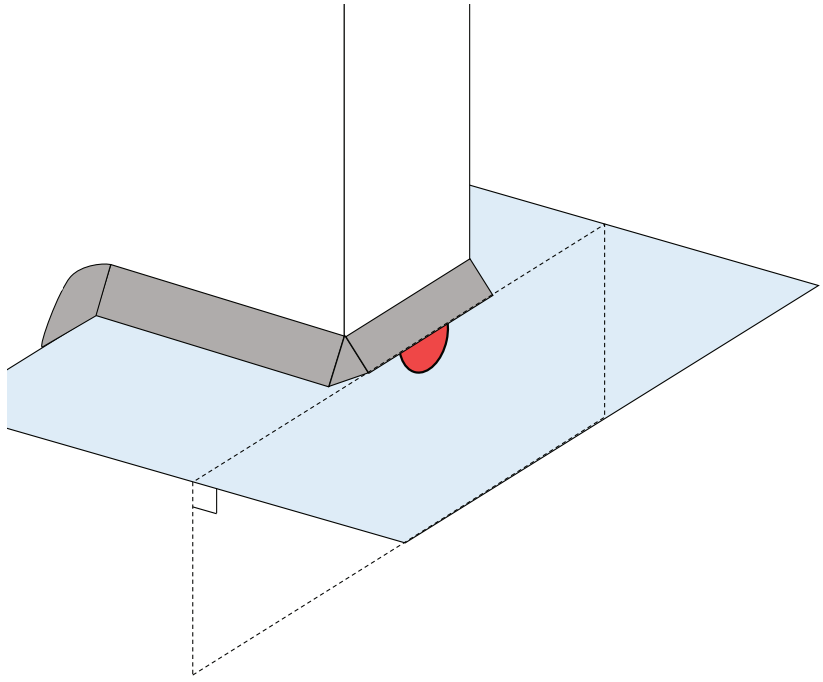

Figure 4.44. The crack growth plane.

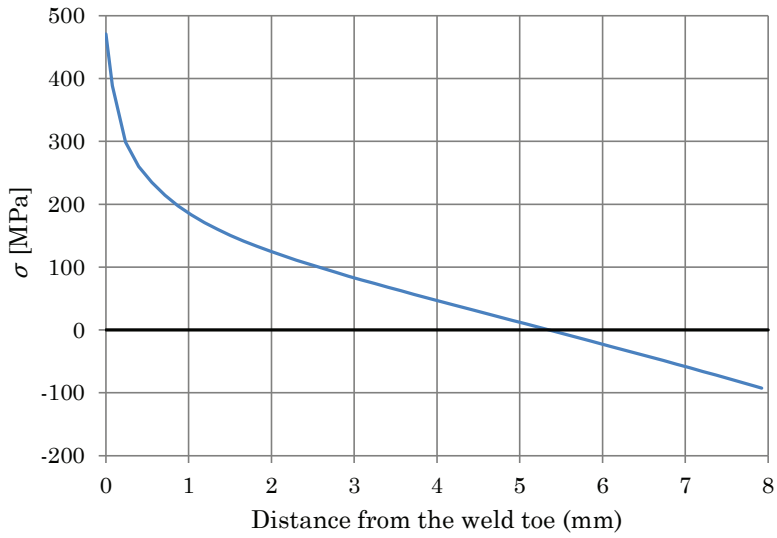

Figure 4.45. Through-thickness stress distribution induced by the $F = 17.8$ kN load.

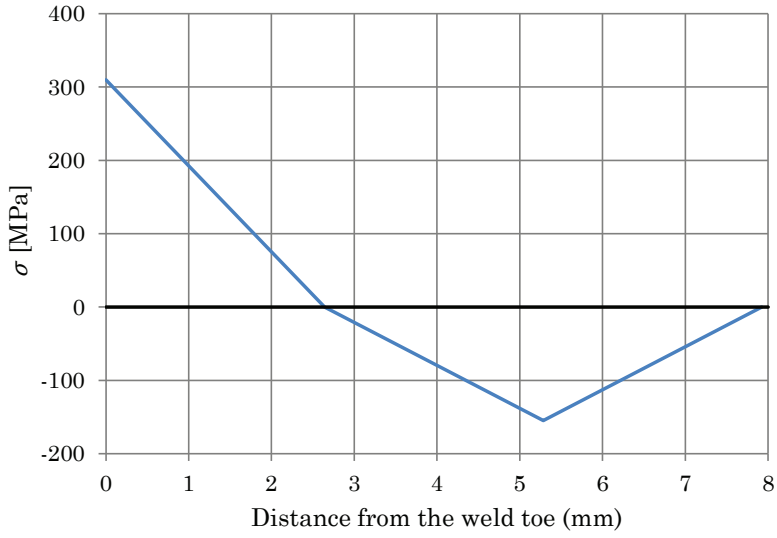

Figure 4.46. Through-thickness residual stress distribution.

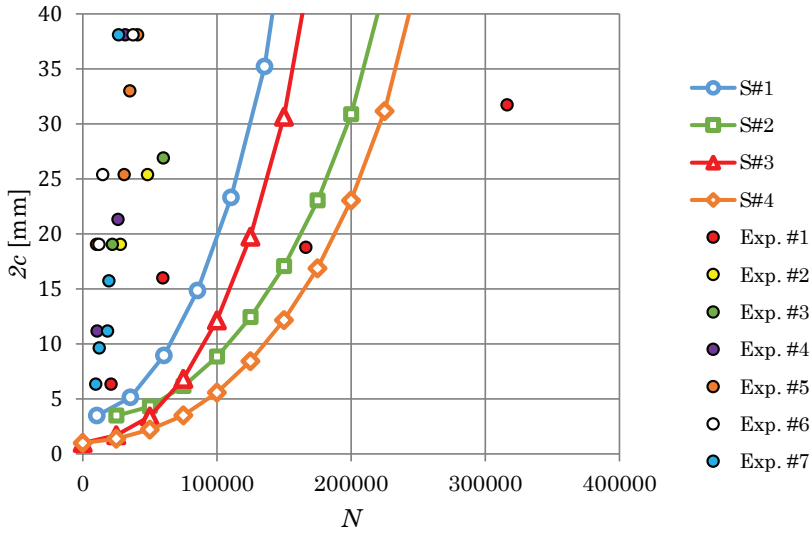

Figure 4.47. Comparison between experimental and simulated fatigue crack growth.

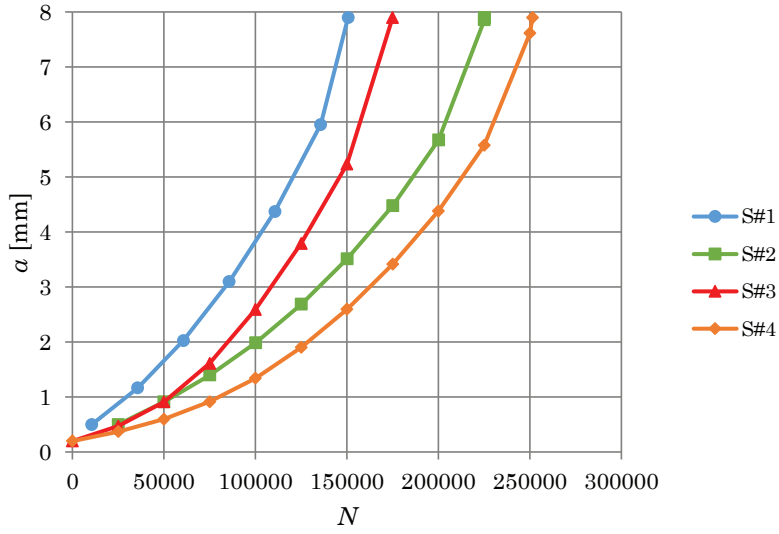

Figure 4.48. Crack growth in the depth direction.

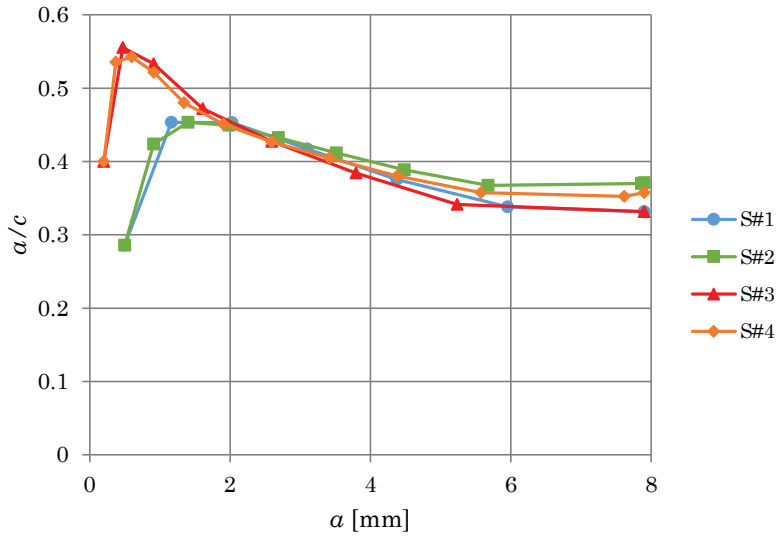

Figure 4.49. The development of the aspect ratio.

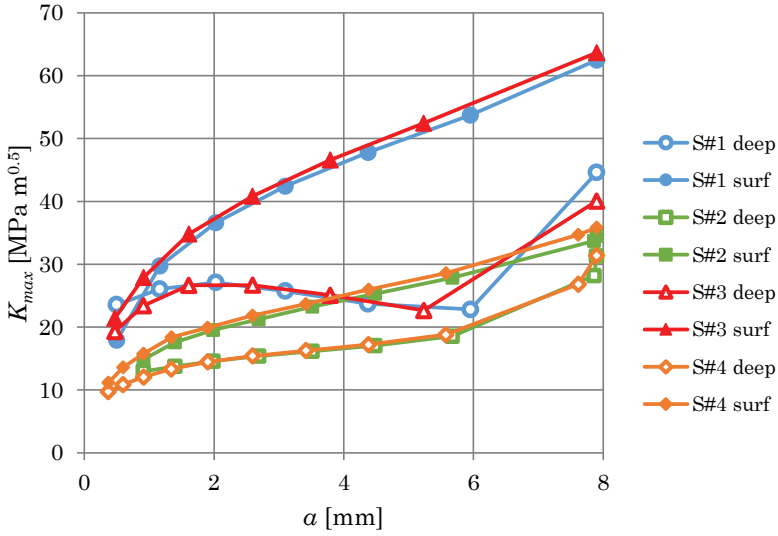

Figure 4.50. SIF at the deepest point and the surface point.

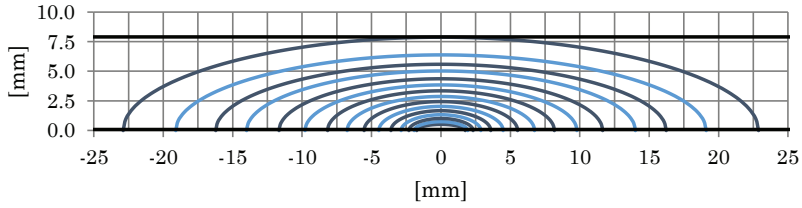

Figure 4.51. Simulated (#1) fatigue crack shape evolution. Contour lines are plotted every $10,000$ cycle.

$t = 4.0$ mm $\quad h = 4.0$ mm $\quad r = 0.55$ mm

$t_p = 4.0$ mm $\quad h_p = 4.0$ mm $\quad \theta = 45^\circ$

The attachment was subjected to a fully-reversed, out-of-plane bending load, induced by the fluctuation ± 308 N force applied at the free edge.

4.7.2 Fatigue life Analysis

Using shell elements, the FEM was employed to determine the most critical location for crack initiation and growth. The most critical point in Fig. 4.53 was identified at the attachment. In order to estimate the fatigue life at this location, the through-thickness stress distribution across the section (Fig. 4.54) was calculated. The residual stress distribution in Fig. 4.55 was approximated, based on limited experimental measurements of stresses on the surface of the attachment.

Four simulations were run, similar to those in Section 4.6, and the input parameters are provided in Table 4.6.

Table 4.6. Parameters for different simulations.

Simulation #	a_i (mm)	a_i/c_i	N_i	Residual stresses
1	0.5	0.286	60277	Yes
2	0.5	0.286	110720	No
3	0.2	0.4	0	Yes
4	0.2	0.4	0	No

The material properties given in Table 4.2 were used. Unfortunately, due to the unavailability of the constant amplitude fatigue curves, $\mathrm{d}a/\mathrm{d}N$ vs. ΔK, the ρ^* parameter was estimated by using Eq. (3.21).

The simulated fatigue crack growth on the surface was compared to the experimental results, as shown inFig. 4.56. The simulated fatigue crack growth in the depth direction is presented in Fig. 4.57. These values were not measured during the experiments. During the simulations, the crack front developed in such a way that the aspect ratio, a/c, did not remain constant, as evidenced in Fig. 4.58. The varying aspect ratio, the non-uniform stress field and the effect of free surfaces influenced the SIFs, as presented inFig. 4.59. The simulated crack front development is illustrated in Fig. 4.60.

The simulated fatigue crack growth on the free surface was compared with the experimental data shown in Fig. 4.56. The simulated fatigue

crack growth in the depth direction is presented in Fig. 4.57. The crack depth dimension was not measured during the experiments. The crack front developed in such a way that the aspect ratio, a/c, in Fig. 4.58 did not remain constant. The varying aspect ratio, the non-uniform stress field and the effect of free surfaces influenced the SIFs, as presented in Fig. 4.59. The simulated crack shape evolution is illustrated in Fig. 4.60.

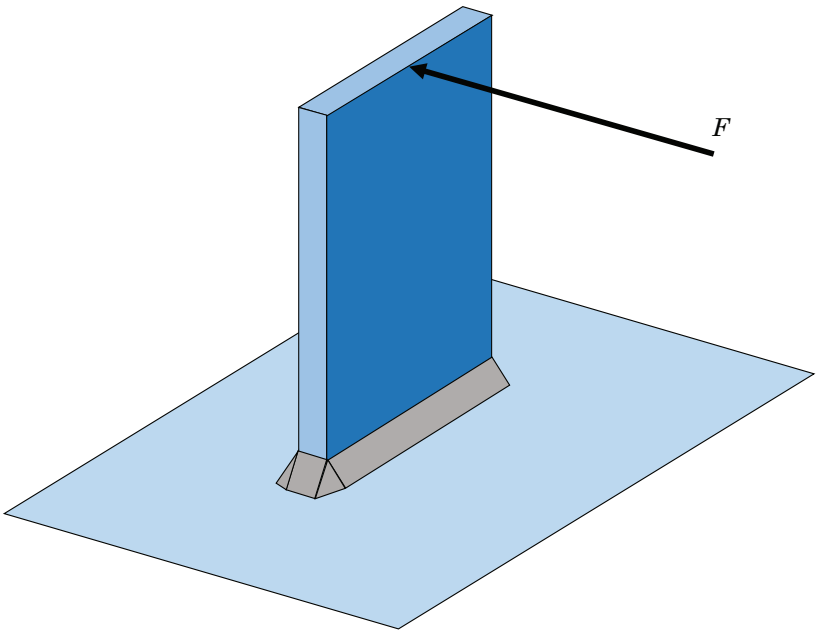

Figure 4.52. Experiment set-up for fatigue life analysis of T-welded joint.

Table 4.7. Material parameters (mean values) for SAE 1008 steel.

Ultimate strength, σ_u	351	MPa
Yield strength, σ_y	198	MPa
Elastic modulus, E	207447	MPa
Fracture Toughness, K_{IC}	80	Mpa $m^{0.5}$
Cyclic strength coefficient, $K^{'}$	1747	MPa
Cyclic hardening exponent, $n^{'}$	0.3219	
Crack tip radius, ρ^{*}	4.73x10^{-6}	m
FCG constant, C	1.95x10^{-12}	(m , MPa $m^{0.5}$)
FCG exponent, m	3.72	

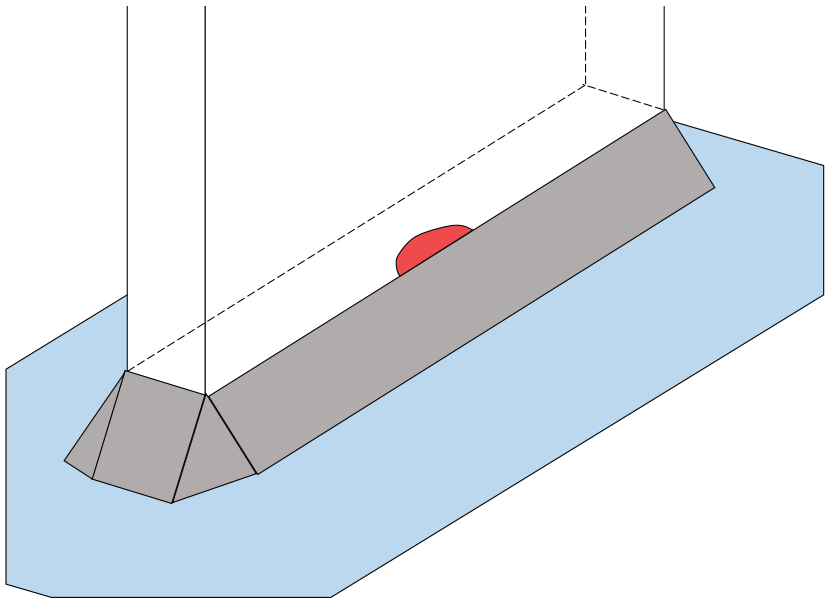

Figure 4.53. Planar crack at the attachment.

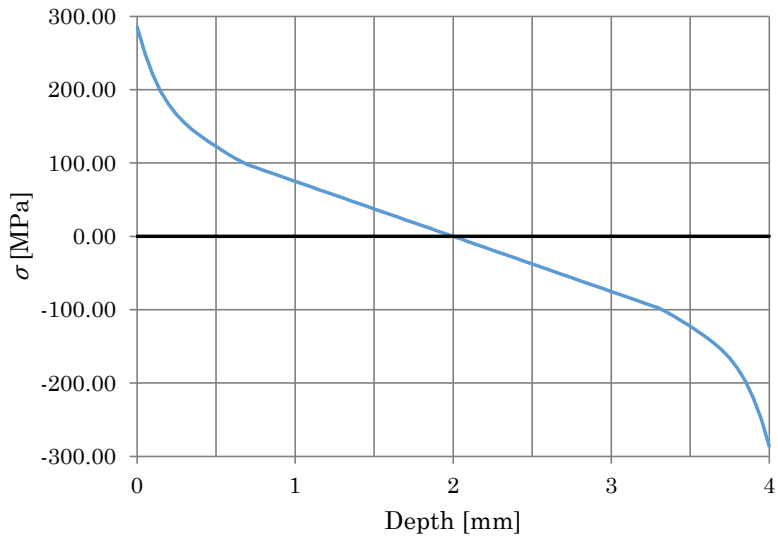

Figure 4.54. Through-thickness stress distribution induced by the $F = 308$ N load.

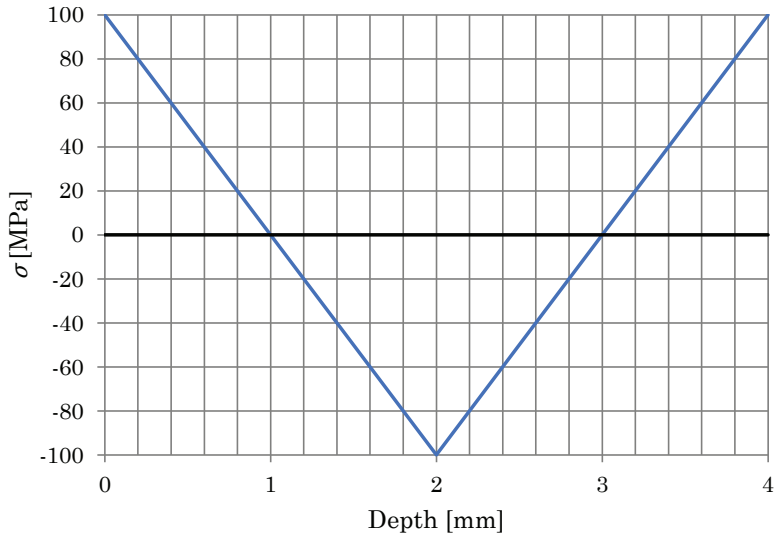

Figure 4.55. Through-thickness residual stress distribution.

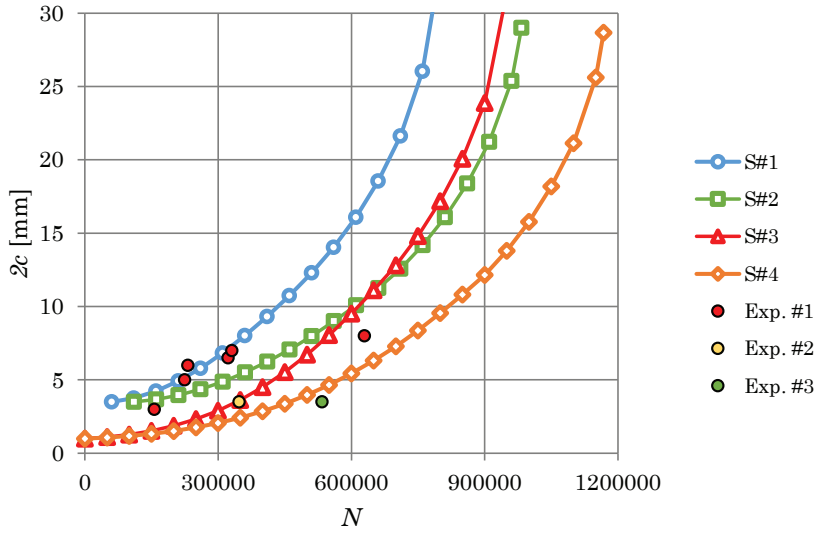

Figure 4.56. Comparison between experimental and simulated fatigue crack growth.

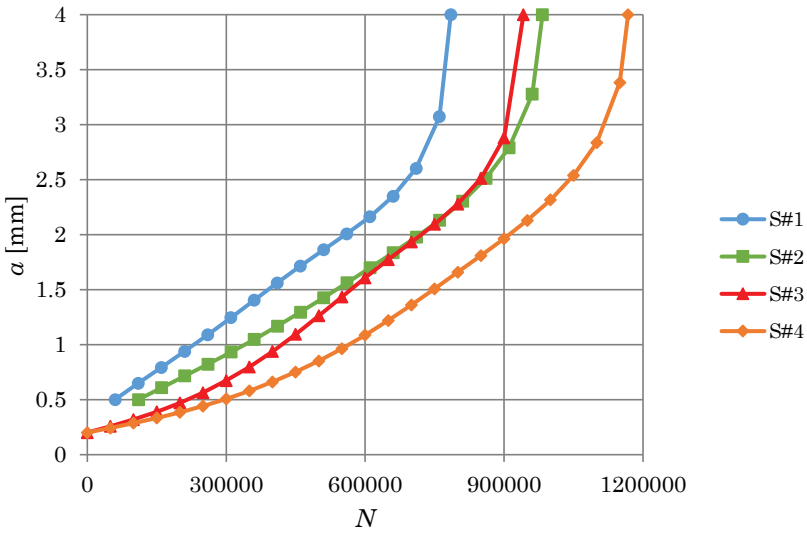

Figure 4.57. Crack growth in the depth direction.

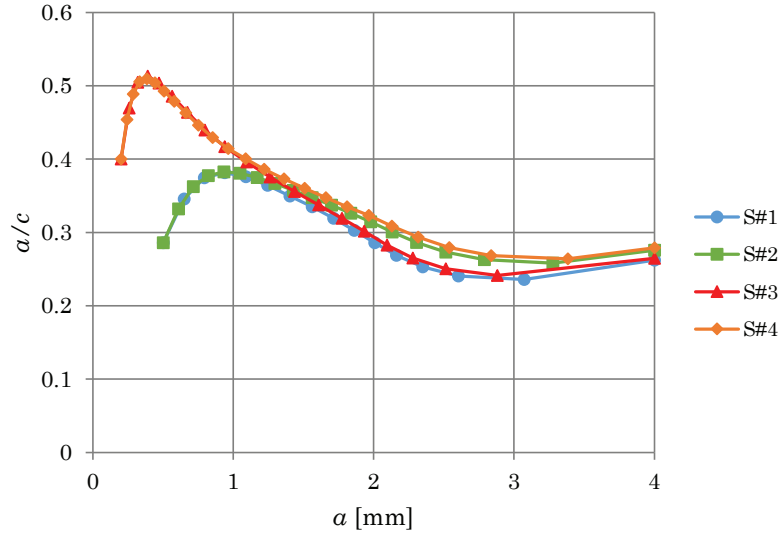

Figure 4.58. The development of the aspect ratio

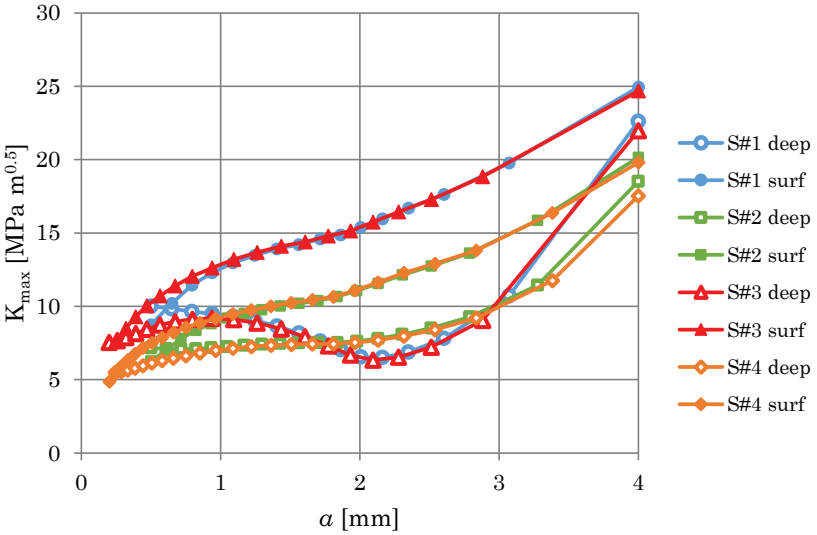

Figure 4.59. SIF at the deepest point and the surface point.

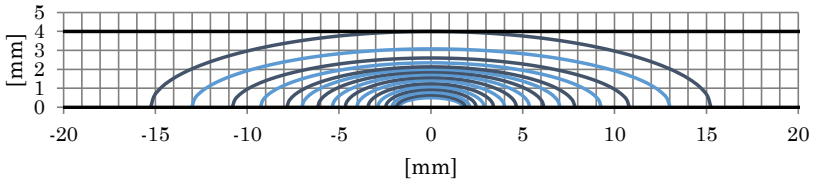

Figure 4.60. Simulated (#1) fatigue crack shape evolution. Contour lines are plotted every $50,000$ cycle.

5. Discussion

5.1 Stress Intensity Factors

One of the most challenging and important aspects of fracture mechanics-based, fatigue assessment is the sufficiently-accurate estimation of SIFs. Because cracks in complex stress fields were analysed, a special methodology was essential for the determination of required SIFs. Consequently, a special weight function method was developed. The novelty of the proposed and validated point load-weight function is that the function is not restricted to any particular geometry or stress field. The point load-weight function enables the calculation of the SIF for any convex planar crack subjected to any non-linear, two-dimensional stress field.

The developed weight function was verified by comparing computed SIFs to solutions from existing literature. Comparisons are made for both embedded and semi-elliptical surface cracks under uniform and non-uniform stress fields. Comparison revealed that the proposed weight function produced SIFs with good accuracy for both crack types, with $a/c = 0.1 - 1.0$ and $a/t = 0.0 - 0.6$ with all linear and non-linear stress distributions.

It was found that in the case of semi-elliptical surface cracks, the SIF values near the free surface were very sensitive with respect to the discretization method, i.e., the length and orientation of the segments. Therefore, this effect is minimised by two different techniques. First of all, the spline-fitting technique was used to maintain a smooth crack front and uniform, linear segment distribution. Secondly, the SIFs near the surface were estimated by extrapolation, based on SIF values at points further away from the surface. The main idea behind these techniques was to reduce the effect of discretization, not to increase the accuracy.

It is difficult to determine the accuracy of the SIFs near the free surface

because the classical $1/\sqrt{r}$ SIF is not well-defined at this location. The solutions, based on the plate theory [64] or the FEM with very fine mesh [65], indicate that the SIF decreases rapidly near the free surface and equals zero at the free surface. However, most of the solutions found in existing literature, [33, 34, 41, 74, 75], yield a non-zero value for the SIF at the surface point. Usually, these solutions are based on the FEM result with relatively-coarse mesh, or some kind of approximation near the surface. In practice, the non-zero SIF at the surface point is needed in order to model fatigue crack growth using linear-elastic fracture mechanics. Therefore, the non-zero SIF at the surface point is used in this work. It would be possible and mathematically correct to force the SIF to decrease to zero at the free surface, but this was not deemed necessary.

5.2 Determinations of the ρ^* Parameter

The crack tip, plasticity-based, fatigue crack growth model, used in the analysis, is based on the assumption that the crack tip radius, the ρ^* parameter, is a material parameter. The parameter, ρ^*, depends on the micro-structural features of the analysed material; unfortunately, it cannot be uniquely associated with any specific micro-structural particle size. Rather, the elementary material block size, ρ^*, can be understood as an average dimension of inhomogeneous material blocks which still behaves like the bulk material of larger volume.

Because the ρ^* parameter cannot be measured directly, several different approaches have been developed for its determination. Since different approaches require different material properties, one can choose an appropriate method based on available material data. In this work, a new method for the approximation of the ρ^* parameter, based on the theoretical strength and fracture toughness of the material, has been proposed. The theoretical strength can be approximated based on the modulus of elasticity and, therefore, only two well-established material properties are needed.

Estimated ρ^* values for steel and aluminium in Table 4.1 are close to the $\rho^*_{ref,2}$ reference values found in existing literature. This indicates that the proposed method for determination of the ρ^* parameter is sufficiently accurate and that the obtained values can be used in fatigue crack growth analysis.

5.3 Planar Cracks Under Non-Uniform Stress Field and Subjected to Variable Amplitude Loading Histories

In order to model fatigue crack growth under variable amplitude loading, the method must account for the loading history effects, e.g., crack retardation following an overload. Therefore, several fatigue analyses were run using various cyclic loading spectra. In addition, the influence of a non-uniform stress field was studied. No experiments were performed. Thus, the results are compared to general knowledge and assumptions based on previous studies related to the behaviour of fatigue cracks.

The constant amplitude loading, Spectrum #1, was used as a reference when other spectra were studied. The amplitude and interval between the overloads in Spectrum #2 and Spectrum #3 were defined so that the effect of a previous overload would disappear before the next was applied. Because of this set-up, one could distinctly see the effect of a single overload. In Spectrum #3, the amplitude of the underload was defined so that the ratio of the overload and the underload was the same as in experiments by Schijve and Broek [77]. The random Spectrum #4 was constructed in such a way that the maximum stress and stress range of the average cycle corresponded to the reference, Spectrum #1.

The results, presented in Figs. 4.24 and 4.25, show clear crack growth retardation after a single overload. The crack contour lines in Fig. 4.24 indicate that there is a delay before retardation occurs. The effect is similar to that observed in previous experiments [77] and numerical calculations when a similar crack tip, plasticity-based model is applied to a one-dimensional crack [82]. If an overload was followed by an immediate underload, the crack retardation was much less apparent (Fig. 4.25), or even disappeared (Fig. 4.24). Based on previous studies [77], this kind of behaviour was to be expected.

The evolution of the crack front is presented in Figs. 4.26 and 4.27. The surface crack remains semi-elliptical due to the application of the uniform stress field. In contrast, due to the non-uniform stress field, the embedded crack develops more arbitrarily and grows faster towards peak stress at $x = 20.0$ mm and $y = 20.0$ mm. This kind of result was assumed and proves that the method presented in this thesis can handle non-uniform stress fields.

5.4 Effect of the Initial Crack Geometry

When fatigue life is estimated by using linear-elastic fracture mechanics, assumptions for the initial crack size and shape are needed. Since the real initial crack geometry is seldom known, assumptions are often based on guidelines or common practice. Therefore, it is important to know to what degree fatigue life estimations vary when different assumptions are made.

The obtained results, as shown in Figs. 4.28 and 4.29, indicate that the effect of the initial shape is negligible when fatigue crack growth is modelled in the Paris region, i.e., $m \approx 3$. The fatigue life estimations differ less than $10\ \%$ when cracks with $a/c \geq 0.1$ are considered. However, this effect becomes more significant when higher values for m are used. The higher m values occur when stresses are low, or when small cracks near the threshold are modelled.

Traditionally, most fatigue crack growth analysis is concentrated in the Paris region and, consequently, the strain-life method is applied to estimate the crack initiation period. However, recent studies indicate that total fatigue life can be determined by using only the crack propagation theory, without dividing the calculations into the initiation and propagation stages [39]. Hence, since fatigue crack growth is also modelled on the threshold region, the effect of the initial crack shape must be considered.

The most conservative fatigue life estimation can be obtained by using Figs. 4.28 and 4.29, or Eqs. (4.3) and (4.4), to determine the initial crack shape that yields the shortest fatigue life. It is important to note that these results are for the cracks under a uniform stress field, although the results discussed in Section 5.5 indicate similar behaviour when an even more complex stress field is applied.

Calculations were made without any small crack corrections so that the effect of crack size was eliminated. While the results are not related to the selected weight function and crack growth law, similar results are obtained with other methods which use the power law expression for the crack growth increment.

5.5 Fatigue Crack Growth of the Small Inclusion in a Valve Spring Wire

The purpose of this case was to verify the ability of the method presented here to estimate the fatigue life of a real engineering component. The component contained a small, sub-surface flaw and virtually the entire fatigue crack growth occurred in the near-threshold region. This proves that initial conditions affect results significantly, as discussed earlier in Section 5.4.

The measured initial flaw size was 20 μm x 30 μm and the flaw was located at a depth of 175μm below the surface. Since the residual stresses were not measured, simulations were run by using several different residual stress fields and the influence on fatigue life was studied. In all cases the stress at the location of the initial flaw, $d = 175\mu$m, was $\sigma_{max} < 900$ MPa. In the case corresponding to $d_c > 150\mu$m and $\sigma_c = -1000$ MPa, crack growth simulation could not be performed because the sum of $\sigma_{max} + \sigma_c$ produced a negative value, thus, the fatigue life was deemed to be infinite.

The fatigue life estimations using different residual stress fields are presented in Fig. 4.37. Results indicate that fatigue life estimations depend significantly on both σ_c and d_c. The maximum influence of d_c is attained soon after d_c goes deeper than the initial crack.

Although the residual stresses were not measured, the residual stress at the surface can be approximated using the material yield limit [78]:

$$\sigma_c = -120 - 0.5 \cdot \sigma_y \text{ [MPa]} \tag{5.1}$$

Using this approximation, $\sigma_c \approx -1000$ MPa is obtained. In the method presented in this thesis, it is assumed that the global residual SIF , K_R, affects only the maximum SIF , $K_{max,tot}$. If K_R affected ΔK_{tot}, then all residual stresses at $\sigma_c > -500$ MPa would yield an infinite life due to $\Delta\sigma \approx 500$ at the initial crack location. In that case, $\sigma_c = -200$ would already produce a fatigue life of hundreds of millions of cycles, or a virtually infinite number. This indicates that the assumption that ΔK_{tot} is not affected by residual stresses is correct. Otherwise, even a small, compressive residual stress would lead to infinite life.

The different initial a/c aspect ratios were studied, the results of which are presented in Fig. 4.38. The shortest fatigue life was obtained by using $a/c = 0.38$. This value is close to $a/c = 0.34$ that can be estimated by using Eq. (4.3). This study indicates that the results related to the initial

crack geometry, discussed in Section 5.4, are even more relevant when a complex, non-uniform stress field is applied.

Figs. 4.39 and 4.40 present the influence of the initial crack size and distance from the free surface. All these results indicate that near-threshold, fatigue crack growth simulations are very sensitive to the initial parameters.

5.6 Fatigue Life Analysis of a Tubular Welded Structure

The fatigue life of a welded, rectangular, hollow-section joint, subjected to bending and torsion, was estimated by using the method outlined in this work. The crack initiation life was taken from existing literature [79] and the fatigue crack growth phase was simulated. In addition, the fatigue life was estimated without including residual stresses, and by using the smaller initial crack without the separated crack initiation phase.

Simulations #1 and #3 yielded fatigue life estimations which were closest to the experiments, as seen in Fig. 4.47. This was expected, because these simulations included the residual stress field. In Simulation #1, the crack initiation life, $N_{i,\#1} = 10,600$, was assumed to be a certain number of cycles to initiate a crack with $a_i = 0.5$ mm. In Simulation #3, it took $27,000$ cycles to grow the crack from $a_i = 0.02$ mm to 0.05 mm. This life can be defined as an initiation life, $N_{i,\#3}$, resulting in the ratio of two initiation lives being $N_{i,\#3}/N_{i,\#1} = 2.5$.

After initiation, the crack depth was equal in both simulations, but the crack lengths at the surface were different: $c = 1.7$ mm ($a/c = 0.29$) in Simulation #1 and $c = 0.9$ mm ($a/c = 0.56$) in in Simulation #3. When the depth of the crack reached 25% of the cross-section thickness, $a = 2$ mm, the aspect ratio, a/c, was 0.45 in both simulations. After this point, the aspect ratios developed similarly. The development on a/c is presented in Fig. 4.49. These results indicate that the initial crack size and shape did not have an effect on the final crack shape, although the fatigue lives turned out to be different.

As previously mentioned, the exclusion of residual stresses affected the fatigue life estimations, as seen for Simulations #2 and #4 in Fig. 4.47. However, the influence was smaller than expected. The residual stresses had a greater influence when the same problem was studied by using a different method [79]. According to both methods, the residual SIF, K_R, is calculated from the residual stress field. However, K_R is included in

calculations in a different manner. In the method presented in this paper, K_R affects $K_{max,tot}$, whereas in [79], K_R is applied to ΔK_{tot}.

In the valve spring case in Section 5.5, the effect of residual stress was much more significant when fatigue crack growth occurred in the threshold region. The obtained results reveal that when the method presented here was used, the influence of residual stresses was felt mainly in the threshold region.

Overall, the simulations verify that the presented model is applicable for welded structures. The difference between experimental and simulated fatigue lives can be considered acceptable when one takes into account complex welded structures.

5.7 Fatigue Life Analysis of a T-Welded Joint

The T-welded joint problem was very similar to the tubular welded structure detailed in Section 5.6, but the geometry was simpler. Similarly, as in the case of the tubular welded structure, four simulations were performed. A comparison between simulated results and experiments is presented in Fig. 4.56. The results show that all four simulations yield realistic fatigue crack behaviour and that estimated fatigue lives are in good agreement with experimental results.

One can make very similar observations to those made for the tubular welded structure. The initiation lives that included the residual stress field were $N_{i,\#1} = 60,277$ and $N_{i,\#3} = 217,000$. Thus, the ratio of two initiation lives was $N_{i,\#3}/N_{i,\#1} = 3.6$. After initiation, the crack depth was equal in both simulations, but the crack lengths at the surface were different: $c = 1.7$ mm ($a/c = 0.29$) in Simulation #1, $c = 1.0$ mm ($a/c = 0.50$) in Simulation #3. Soon after the depth of the crack reached 25% of the cross-section thickness, $a = 1$ mm, the aspect ratio, a/c, was 0.36 in both simulations. After this point, the aspect ratios developed in a similar manner. The development of a/c is presented in Fig. 4.58.

Based on the results presented, the previous observation that the residual stress field decreases fatigue life can be confirmed, albeit not significantly in the Paris region.

6. Conclusions

In this thesis, a new method was presented for modelling the fatigue crack growth of arbitrary planar cracks subjected to a non-uniform stress field, induced by variable amplitude loading. The method was developed because the existing methods were limited to simple standard geometries and one-dimensional stress fields.

The presented method consists of three important parts: SIF calculation, crack growth increment calculation and algorithms to advance the crack front. When arbitrary cracks were considered, the SIF calculation was the most challenging aspect. Therefore, the new general point-load weight function was developed. The new weight function yielded more accurate SIFs for surface cracks than those obtained by using the general weight function, derived mainly for embedded cracks. Since surface cracks pose a more common problem in real engineering applications than embedded cracks, the developed weight function is needed.

After the SIF calculation, the crack growth increment was calculated using the crack tip, plasticity-based model. The model has previously been used to simulate only one-dimensional or very limited two-dimensional cracks. In this work, the model was used to determine the crack growth increment along the arbitrarily-shaped crack front. Advancing the crack front was not a simple task because the crack front was defined by linear segments and the crack growth increment was known at discrete points. After consideration of this problem, a potential solution is presented in this thesis.

The presented method is validated in three different stages. At first, SIFs were calculated for the cracks under several different stress fields. These calculations indicated that the proposed weight function can be applied to both embedded and surface cracks under complex stress fields. The second stage included crack growth simulations, during which four

different loading spectra were applied. The influence of overloads and underloads were studied and the expected crack retardation effect was observed. The simulated fatigue behaviour was similar to that observed in experiments. The third phase comprised fatigue life estimations for real engineering components. These exercises demonstrated that the method presented in this thesis can be utilised for the estimation of real fatigue lives when complex problems are considered.

In numerical simulations, the effect of initial crack geometry and residual stresses were studied. It was shown that the most critical initial crack geometry depends on the fatigue crack growth exponent, m. The influence of the initial crack shape is significant when fatigue crack growth occurs near the threshold region. Conversely, in the Paris region, this effect was almost negligible. Similar observations were made when the residual stresses were studied. The residual stresses were found to have the greatest effect in the threshold region and this influence may prove to be very significant.

Bibliography

[1] Jaap Schijve. *Fatigue of structures and materials*. Springer, 2009.

[2] P. C. Paris and F. Erdogan. A critical analysis of crack propagation laws. *J. Basic Engineering*, 85:528–534, 1963.

[3] G. Marquis. Variable amplitude loading. In A. MacDonald, K, editor, *Fracture and Fatigue of Welded Joints and Structures*, chapter 8, pages 208–238. Woodhead Publishing Ltd, Cambridge, 2011.

[4] R. G. Forman, V. E. Kearny, and R. M. Engle. Numerical analysis of crack propagation in a cyclic-loaded structure. *Trans. ASME J Basic Eng.*, pages 458–464, 1967.

[5] K. Walker. The effect of stress ratio during crack propagation and fatigue for 2024-t3 and 7075-t6 aluminum. In *Effects of Environment and Complex Load History on Fatigue Life*, ASTM STP 462. ASTM, Philadelphia, PA, 1970.

[6] J. M. Barsom and S. T. Rolfe. *Fracture Control in Structures*. Prentice-Hall, Englewood Cliffs, NJ, 1977.

[7] D. N. Lal. The combined effects of stress ratio and yield strength on the LEFM fatigue threshold condition. *Fatigue Frac. Eng. Mat. Struc.*, 15:1199–1212, 1992.

[8] O. E. Wheeler. Spectrum loading and crack growth. *J. Basic Eng.*, 94:181–186, 1972.

[9] J. Willenborg, R. M. Engle, and H. A. Wood. *A crack growth retardation model using an effective stress concept*. AFFDL-TR71-1. Air Force Flight Dynamic Laboratory, Wright-Patterson Air Force Base, 1971.

[10] W. Elber. Fatigue crack closure under cyclic tension. *Eng. Frac. Mech*, 2: 37–45, 1970.

[11] W. Elber. The significance of fatigue crack closure, in: Damage tolerant aircraft structures. In *Damage Tolerant Aircraft Structures*, ASTM STP 486, pages 230–242. ASTM, Philadelphia, PA, 1971.

[12] A. U. de Koning. A simple crack closure model for prediction of fatigue crack growth rates under variable-amplitude loading. In R. Roberts, editor, *Fracture Mechanics*, ASTM STP 743, pages 63–85. ASTM, Philadelphia, PA, 1981.

[13] T. H. Topper and M. T. Yu. The effect of overloads on threshold and crack closure. *Int. J. Fatigue*, 7:159–164, 1985.

[14] J. Schjive. *Fatigue of Structures and Materials*. Kluwer Academic Publishers, Dordrecht, 2001.

[15] H. Führing and T. Seeger. Structural memory of cracked components under irregular loading. In C. W. Smith, editor, *Fracture Mechanics*, ASTM STP 677, pages 144–167. ASTM, Philadelphia, PA, 1979.

[16] J. C. Newman Jr. A crack-closure model for predicting fatigue crack growth under aircraft spectrum loading. In J. B. Chang and C. M. Hudson, editors, *Methods and Models for Predicting Fatigue Crack Growth under Random Loading*, ASTM STP 748, pages 53–84. ASTM, Philadelphia, PA, 1981.

[17] G. S. Wang and A. F. Blom. A strip model for fatigue crack growth prediction under general load conditions. *Eng. Frac. Mech.*, 40:507–533, 1991.

[18] D. S. Dugdale. Yielding of steel sheets containing slits. *Journal of the Mechanics and Physics of Solids*, 8(2):100–104, 1960.

[19] K. Sadananda, A. K. Vasudevan, R. L. Holtz, and E. U. Lee. Analysis of overload effects and related phenomena. *Int. J. Fatigue*, 21:S233–S246, 1999.

[20] A. H. Noroozi, G. Glinka, and S. Lambert. A two parameter driving force for fatigue crack growth analysis. *International Journal of Fatigue*, pages 1277–1296, 2005.

[21] A. H. Noroozi, G. Glinka, and S Lambert. Prediction of fatigue crack growth under constant amplitude loading and a single overload based on elastoplastic crack tip stresses and strains. *Engineering Fracture Mechanics*, pages 188–206, 2007.

[22] S. Mikheevskiy. *Elastic-Plastic Fatigue Crack Growth Analysis under Variable Amplitude Loading Spectra*. PhD thesis, University of Waterloo, 2009.

[23] K. J. Miller. The short crack problem. *Fatigue & Fracture of Engineering Materials & Structures*, 5(3):223–232, 1982. ISSN 1460–2695.

[24] R. O. Ritchie and J. Lankford. Small fatigue cracks: A statement of the problem and potential solutions. *Materials Science and Engineering*, 84(0): 11–16, 1986.

[25] S. Suresh and R. O. Ritchie. Propagation of short fatigue cracks. *International Materials Reviews*, 29(1):445–475, 1984.

[26] M. F. E. Ibrahim and K. J. Miller. Determination of fatigue crack initiation life. *Fatigue & Fracture of Engineering Materials & Structures*, 2(4):351–360, 1979. ISSN 1460-2695.

[27] J. R. Rice. A path independent integral and the approximate analysis of strain concentration by notches and cracks. *Journal of Applied Mechanics*, 35:379–386, 1968.

[28] T. L. Anderson. *Fracture Mechanics: Fundamentals and Applications*. CRC Press, Boca Raton, 1995.

[29] X. B. Lin and R. A. Smith. Finite element modelling of fatigue crack growth of surface cracked plates: Part i: The numerical technique. *Engineering Fracture Mechanics*, 63(5):503 – 522, 1999.

[30] X. B. Lin and R. A. Smith. Finite element modelling of fatigue crack growth of surface cracked plates: Part ii: Crack shape change. *Engineering Fracture Mechanics*, 63(5):523 – 540, 1999.

[31] N. Sukumar, D. L. Chopp, and B. Moran. Extended finite element method and fast marching method for three-dimensional fatigue crack propagation. *Engineering Fracture Mechanics*, 70(1):29–48, 2003.

[32] I. V. Singh, B. K. Mishra, S. Bhattacharya, and R. U. Patil. The numerical simulation of fatigue crack growth using extended finite element method. *International Journal of Fatigue*, 36(1):109 – 119, 2012.

[33] Y. Murakami, editor. *Stress Intensity Factors Handbook*. Pergamon Press, Oxford, 1987.

[34] H. Tada, P. C. Paris, and G. R. Irwin. *Stress Analysis of Cracks Handbook*. ASME Press, 3 edition, 2000.

[35] H. F. Bueckner. A novel principle for the computation of stress intensity factor. *Zeitschrift für Angewandte Mathematik und Mechanik*, 50(9):529–546, 1970.

[36] J. R. Rice. Some remarks on elastic crack-tip stress fields. *International Journal of Solids and Structures*, 8(6):751–758, 1972.

[37] G. Shen and G. Glinka. Determination of weight functions from reference stress intensity factors. *Theoretical and Applied Fracture Mechanics*, 15: 237–245, 1991.

[38] S. Mikheevskiy, G. Glinka, and D. Algera. Analysis of fatigue crack growth in an attachment lug based on the weight function technique and the unigrow fatigue crack growth model. *International Journal of Fatigue*, 42(0): 88 – 94, 2012. Fatigue Damage of Structural Materials VIII.

[39] R. Goyal and G. Glinka. Fracture mechanics-based estimation of fatigue lives of welded joints. *Welding in the World*, 57(5):625–634, 2013.

[40] X. Wang and G. Glinka. Determination of approximate point load weight functions for embedded elliptical cracks. *International Journal of Fatigue*, 31(11–12):1816 – 1827, 2009. ISSN 0142-1123.

[41] R. Ghajar and H. Saeidi Googarchin. General point load weight function for semi-elliptical crack in finite thickness plates. *Engineering Fracture Mechanics*, 109(0):33 – 44, 2013.

[42] H. Saeidi Googarchin and R. Ghajar. Stress intensity factors calculation for surface crack in cylinders under longitudinal gradient pressure using general point load weight function. *Fatigue & Fracture of Engineering Materials & Structures*, 37(2):184–194, 2014.

[43] M. Oore and D. J. Burns. Estimation of stress intensity factors for embedded irregular cracks subjected to arbitrary normal stress fields. *Journal of Pressure Vessel Technology*, 102/211, 1980.

[44] G. Glinka and W. Reinhardt. Calculation of stress intensity factors for cracks of complex geometry and subjected to arbitrary nonlinear stress fields. *Fatigue and Fracture Mechanics*, 31, ASTM STP 1389:348–370, 2000.

[45] Z. Wu, H. Jakubczak, G. Glinka, K. Molski, and L. Nilsson. Determination of stress intensity factors for cracks in complex stress fields. *Archive of Mechanical Engineering*, Vol. L, nr 1:41–67, 2003.

[46] P. Lindroth, G. Glinka, and G. Marquis. Stress intensity factors for planar cracks of arbirary shapes. In *Fatigue Design 2011 Conferensce Proceedings*, 2011.

[47] A. Jankowiak, H. Jakubczak, and G Glinka. Fatigue crack growth analysis using 2-d weight function. *International Journal of Fatigue*, 31:1921–1927, 2009.

[48] D. N. Lal and V. Weiss. A notch analysis of fracture approach to fatigue crack propagation. *Metallurgical Transactions A*, 9(3):413—-426, 1978.

[49] L. R. Kaisand and D. F. Mowbray. Relationships between low-cycle fatigue and fatigue crack growth-rate properties. *Journal of Testing and Evaluation*, 7(5):270–280, 1979.

[50] G. Glinka. A notch stress-strain analysis approach to fatigue crack growth. *Engineering Fracture Mechanics*, 21(2):245–261, 1985.

[51] H. Neuber. *Kerbspannugslehre*. Springer, Berlin, 1985.

[52] P. J. E. Forsyth. A unified description of micro and macroscopic fatigue crack behaviour. *International Journal of Fatigue*, 5(1):3–14, January 1983.

[53] W. Ramberg and W. R. Osgood. Description of stress-strain curves by three parameters. In *Technical Note No. 902*. National Advisory Committee For Aeronautics, Washington DC, 1943.

[54] J. M. Tartaglia, P. E. Ritter, R. B. Gundlach, and L. Jenkins. Technical report on low cycle fatigue properties: ferrous and non-ferrous metals. In *SAE Standard No. J1099*. Society of Automotive Engineers (SAE), Warrendale, Pennsylvania, 1998.

[55] K. N. Smith, P. Watson, and T. H. Topper. A stress–strain function for the fatigue of metals. *Journal of Materials*, 5(4):767–778, 1970.

[56] M. Creager and P. C. Paris. Elastic field equations for blunt cracks with reference to stress corrosion cracking. *International Journal of Fracture*, 3 (4):247–252, 1967.

[57] H. Neuber. Theory of stress concentration for shear-strained prismatic bodies with arbitrary nonlinear stress-strain law. *Journal of Applied Mechanics*, 28:544–551, 1961.

[58] A. Moftakhar, A. Buczynski, and G. Glinka. Calculation of elastoplastic strains and stresses in notched under multiaxial loading. *International Journal of Fracture*, 70(4):337 – 357, 1995.

[59] G. Glinka and A. Buczynski. Multiaxial stress–strain notch analysis. In S. Kalluri and P. J. Bonacuse, editors, *Multiaxial fatigue and deformation*, STP 1387, pages 82 – 98. American Society for Testing and Materials, Philadelphia, 2000.

[60] Norman E. Dowling. *Mechanical Behavior of Materials*. Prentice Hall, 3 edition, 2006.

[61] J. Schijve. The significance of fractography for investigations of fatigue crack growth under variable-amplitude loading. *Fatigue & fracture of engineering materials & structures*, 22(2):87 – 99, 1999.

[62] H. Remes, P. Varsta, and J. Romanoff. Continuum approach to fatigue crack initiation and propagation in welded steel joints. *International Journal of Fatigue*, 40:16–26, July 2012.

[63] J. R. Rice. Weight function theory for three-dimensional elastic crack analysis. *Fracture Mechanics: Perspectives and Directions (Twentieth Symposium)*, pages 29–57, 1989.

[64] R. J. Hartranft and G. C. Sih. An approximate three-dimensional theory of plates with application to crack problems. *International Journal of Engineering Science*, 8(8):711–729, 1970.

[65] I. S. Raju and J. C. Newman. Stress-intensity factors for a wide range of semi-elliptical surface cracks in finite-thickness plates. *Engineering Fracture Mechanics*, 11(4):817 – 829, 1979.

[66] X. Cheng, J. W. Fisher, H. J. Prask, T. Gnäupel-Herold, B. T. Yen, and S. Roy. Residual stress modification by post-weld treatment and its beneficial effect on fatigue strength of welded structures. *International Journal of Fatigue*, 25(9–11):1259–1269, 2003.

[67] H. Kitagawa and S. Takahashi. Applicability of fracture mechanics to very small cracks or the cracks in the early stage. In *Proceedings of Second International Conference on Mechanical Behaviour of Materials*, pages 627–31, Metal Park, OH, 1976. American Society for Metals.

[68] David Taylor. *The Theory of Critical Distances. A New Perspective in Fracture Mechanics*.

[69] J. Pokluda, M. Černý, P. Šandera, and M. Šob. Calculations of theoretical strength: State of the art and history. *Journal of Computer-Aided Materials Design*, 2004.

[70] P. Lindroth, G. Marquis, and G Glinka. Fatigue crack growth of arbitrary planar cracks in welded components. *Welding in the World*, 57(3):425–435, 2013.

[71] T. J. Nykänen. Fatigue crack growth simulations based on free front shape development. *Fatigue & Fracture of Engineering Materials & Structures*, 19 (1):99–109, 1996.

[72] W. F. Brown and J. E. Srawley. *Plane Strain Crack Toughness Testing of High Strength Metallic Material*, volume ASTM STP 410, pages 110—-114. American Society for Testing and Materials, Philadelphia, 1966.

[73] E. Atroshchenko, S. Potapenko, and G. Glinka. Weight function for an elliptical planar crack embedded in a homogeneous elastic medium. *International Journal of Fracture*, 165(1):39–45, 2010.

[74] J. C. Newman and I. S. Raju. An empirical stress-intensity factor equation for the surface crack. *Engineering Fracture Mechanics*, 15(1–2):185 – 192, 1981.

[75] X. Wang and S.B. Lambert. Stress intensity factors for low aspect ratio semi-elliptical surface cracks in finite-thickness plates subjected to nonuniform stresses. *Engineering Fracture Mechanics*, 51(4):517–532, 1995.

[76] A. H. Noroozi, G. Glinka, and S. Lambert. A study of the stress ratio effects on fatigue crack growth using the unified two-parameter fatigue crack growth driving force. *International Journal of Fatigue*, 29(9–11):1616–1633, 2007. Fatigue Damage of Structural Materials {VI} The Sixth International Conference on Fatigue Damage of Structural Materials.

[77] J. Schijve and D. Broek. Crack propagation: The results of a test programme based on a gust spectrum with variable amplitude loading. *Aircraft Engineering and Aerospace Technology*, 34(11):314 – 316, 1962.

[78] S. Wang, Y. Li, M. Yao, and R. Wang. Compressive residual stress introduced by shot peening. *Journal of Materials Processing Technology*, 73(1–3):64 – 73, 1998.

[79] A. Chattopadhyay, G. Glinka, M. El-Zein, and J. Qian. Stress analysis and fatigue of welded structures. *Welding in the World*, 55, 2011.

[80] T. Nykänen, G. Marquis, and T. Björk. A simplified fatigue assessment method for high quality welded cruciform joints. *International Journal of Fatigue*, 31:79–87, 2009.

[81] John Deere, Moline Technology Innovation Center, Courtesy of Dr. Mohamad El-Zein, 2005.

[82] S. Mikheevskiy and G. Glinka. Elastic–plastic fatigue crack growth analysis under variable amplitude loading spectra. *International Journal of Fatigue*, 31(11–12):1828 – 1836, 2009. Fatigue Damage of Structural Materials VII.

Aalto-DD 130/2014

ISBN 978-952-60-5836-8
ISBN 978-952-60-5837-5 (pdf)
ISSN-L 1799-4934
ISSN 1799-4934
ISSN 1799-4942 (pdf)

Aalto University
School of Engineering
Department of Applied Mechanics
www.aalto.fi

BUSINESS +
ECONOMY

ART +
DESIGN +
ARCHITECTURE

SCIENCE +
TECHNOLOGY

CROSSOVER

**DOCTORAL
DISSERTATIONS**